

Geodätisch-geophysikalische Arbeiten in der Schweiz

(Fortsetzung der Publikationsreihe
«Astronomisch-geodätische Arbeiten in der Schweiz»)

herausgegeben von der

Schweizerischen Geodätischen Kommission
(Organ der Akademie der Naturwissenschaften Schweiz)

**Neunundsechzigster Band
Volume 69**

Absolute Airborne Gravimetry

Henri Baumann

2005

Adresse der Schweizerischen Geodätischen Kommission:

Institut für Geodäsie und Photogrammetrie
Eidg. Technische Hochschule Zürich
ETH Hönggerberg
CH-8093 Zürich, Switzerland

Internet: <http://www.sgc.ethz.ch>

ISBN 3-908440-12-2

Redaktion des 69. Bandes:
Dr. H. Baumann, Dr. M. Troller

Druck: ADAG COPY AG, Zürich

FOREWORD

With the advent of radar altimeter satellite techniques it has become possible to monitor the height of the instantaneous sea surface on a global scale. In order to interpret these data in terms of sea level changes caused by climatic changes, it is mandatory to determine the reference surface, an equipotential surface of the earth's gravity field, at very high accuracy. The only way to achieve this in near coastal regions, in particular, is by means of airborne gravimetry.

The majority of kinematic gravity measurements are performed with relative spring-based instruments which are, however, difficult to calibrate over large dynamic ranges. Furthermore they suffer from drifts and tares which are extremely difficult to correct in kinematic mode. In order to overcome these limits the potential of absolute airborne gravity (AAG) measurements was studied. This technique measures gravity directly by tracking a freely falling object in a vacuum chamber. The problem is to separate non-gravitational aircraft accelerations and vibrations from the gravity signals. The work presented is the first attempt worldwide to construct such a system for application in airborne mode. Henri Baumann did a very careful analysis on this problem, tested mechanical coupling systems, and developed appropriate mathematical algorithms.

Before mounting the instrument in the aircraft systematic experiments were carried out to test the transfer function of the mechanical filters in a truck. In the airborne experiment external sensors, such as EpiSensor and INS, were also attached to the measuring platform, in order to determine external accelerations and deviations from verticality, respectively. Of particular interest was the upward continuation of ground gravity data to flight level. This provides an independent check on the reliability of the airborne results achieved. Also systematic comparisons with previous relative airborne measurements were made.

The results achieved will form an integral part in future developments of airborne gravimetric techniques. Henri Baumann has provided a significant body of work which forms a sound basis for future developments in this field of research. The success of this project is also greatly due to the never-ending engagement of Prof. Dr. E. Klingelé who offered invaluable help at all stages of the research study. Ziegler Consultants, Zürich, and the Laboratoire de Topométrie, EPFL, provided substantial support to vibration and inertial measurements, respectively. The unbureaucratic support of Dr. T. Niebauer of MicroG and the valuable support of swisstopo during the flight campaigns are gratefully acknowledged.

Overall this was a huge task, and the Swiss Geodetic Commission (SGC) congratulates Henri Baumann for his pioneering work as a new contribution of Swiss Geodesy to the international community. The project was supported by ETH Zurich research grant TH-01803 / 19/99-4, and the SGC. We are furthermore grateful to the Swiss Academy of Sciences for covering the printing costs of this volume.

Prof. Dr. H.-G. Kahle,
Prof. Dr. E. E. Klingelé
Institute of Geodesy and Photogrammetry
ETH Zürich

Prof. Dr. A. Geiger
ETH Zürich
President of SGC

VORWORT

Mit dem Aufkommen der Satellitenaltimetrie ist es möglich geworden, den Meeresspiegel im globalen Massstab zu kartieren. Um die Daten in Form von Meeresspiegeländerungen als Folge des Klimawandels zu interpretieren, braucht man eine hochgenaue Referenzfläche, die Äquipotentialfläche des Schwerefeldes der Erde. Die einzige Möglichkeit, diese zu bestimmen und festzulegen, liefert die fluggestützte Gravimetrie. Dies gilt insbesondere in küstennahen Regionen.

Üblicherweise werden kinematische Gravimetermessungen mit Federgravimetern vorgenommen, die allerdings über grosse dynamische Bereiche schwer zu kalibrieren sind und nur relative Schweredaten liefern. Ein schwergewichtiges Defizit sind zudem Drifterscheinungen und Sprünge der Feder, die im kinematischen Modus nur schwer zu korrigieren sind. Um diese Schwierigkeiten zu vermeiden, wurde die Methode der Absolutgravimetrie untersucht. Dabei wird die Schwerebeschleunigung direkt durch die Bewegung einer frei fallenden Testmasse im Vakuum bestimmt. Das Problem dabei ist die Trennung der nicht-gravitativen Beschleunigungen von dem wirklichen gravitativen Signal der Erde. Die vorliegende Arbeit stellt den ersten Versuch weltweit dar, ein solches System zu entwickeln und im fluggestützten Modus zu erproben. Henri Baumann hat hierzu eine ausführliche Analyse aller auftretenden physikalisch-theoretischen und praktischen Probleme durchgeführt, verschiedene mechanische Plattformen entwickelt und getestet, sowie geeignete mathematische Algorithmen zur Auswertung entwickelt.

Vor den eigentlichen Flugmessungen wurden systematische Versuche am Boden und in einem Mini-Lastwagen durchgeführt, um die Übertragungsfunktion der mechanischen Filter zu testen. In den Flugversuchen wurden externe Beschleunigungssensoren hinzugefügt, um die externen Beschleunigungen sowie Abweichungen vom vertikalen Fall zu bestimmen. Zur Bestimmung der Zuverlässigkeit und Genauigkeit wurden Bodenwerte analytisch nach oben auf Flughöhe fortgesetzt. Hierdurch konnte eine unabhängige Überprüfung der neuen Methode realisiert werden.

Die vielversprechenden Resultate bilden einen wichtigen integrierenden Bestandteil der fluggestützten Gravimetrie. Henri Baumann hat eine überaus wichtige Pionierarbeit dazu geleistet, die wegweisend für zukünftige Weiterwicklungen auf diesem Gebiet ist. Der Erfolg dieser Forschung und Entwicklung wäre ohne die tatkräftige Unterstützung von Herrn Prof. Dr. E. Klingelé nicht möglich gewesen. In allen Phasen der Projektarbeit hat Herr Klingelé wertvolle Hilfe geleistet. Die Firma Ziegler Consultants, Zürich, sowie das Laboratoire de Topométrie, EPFL, lieferten wichtige Beiträge im Bezug auf Vibrations- bzw. Inertialmessungen. Auch die unbürokratische Hilfe von Dr. T. Niebauer, MicroG, sowie die wertvolle Unterstützung während den Flugkampagnen durch die swisstopo werden ausdrücklich verdankt.

Die Schweizerische Geodätische Kommission (SGK) gratuliert Herrn Baumann für seine Pionierleistung. Sie ist ein wichtiger Beitrag der schweizerischen Geodäsie im internationalen Verbund. Das Projekt wurde von der ETH Zürich, research grant TH-01803 / 19/99-4, und der SGK unterstützt. Zudem danken wir der Akademie für Naturwissenschaften Schweiz für die Übernahme der Druckkosten.

Prof. Dr. H.-G. Kahle,
Prof. Dr. E.E. Klingelé
Institut für Geodäsie und Photogrammetrie
ETH Zürich

Prof. Dr. A. Geiger
ETH Zürich
Präsident der SGK

PREFACE

Avec l'avènement de l'altimétrie radar par satellites il est devenu possible de contrôler, à grande échelle, la hauteur instantanée de la hauteur des mers. Afin d'interpréter ces données en termes de changements du niveau des mers causés par des changements climatiques, il est obligatoire de déterminer la surface de référence, une surface équipotentielle du champ de pesanteur terrestre, avec une grande précision. La seule voie pour obtenir cette surface, particulièrement dans les zones côtières, est d'utiliser la gravimétrie aéroportée.

La majorité des mesures gravimétriques cinématiques sont faites avec des instruments relatifs, utilisant un ressort et qui sont difficiles à calibrer sur de grandes plages dynamiques. De plus ces instruments souffrent de dérives et de discontinuités qui sont extrêmement difficiles à corriger en mode cinématique. Afin de surmonter ces limitations, le potentiel de la gravimétrie absolue aéroportée (AAG) a été étudié. Cette technique mesure la gravité directement en mesurant la position d'un corps en chute libre dans une chambre sous vide. Le problème est de séparer les accélérations non gravitationnelles des accélérations produites par les mouvements de l'avion et par les vibrations. Le travail présenté ici est la première tentative mondiale de construire un tel système pour une application aéroportée. Monsieur H. Baumann a fait une analyse soignée de ce problème, a testé des systèmes mécaniques de couplages et a développé les algorithmes mathématiques appropriés.

Avant de monter l'instrument dans l'avion des expériences systématiques ont été conduites avec un camion afin de déterminer la fonction de transfert des filtres mécaniques utilisables. Dans l'expérience aéroportée des senseurs externes tel que EpiSenseur et INS ont été joints à la plateforme de mesure afin de déterminer respectivement les accélérations externes et les déviations autour de la vertical du système. Un intérêt particulier a été porté à la continuation des mesures terrestres à l'altitude de vol. Cette prolongation fournit un contrôle indépendant de la fiabilité des résultats obtenus. Des comparaisons systématiques avec des levés aéroportés existants ont aussi été conduites.

Les résultats obtenus formeront une partie intégrante des développements futurs de la technique gravimétrique aéroportée. Monsieur H. Baumann a fourni un travail significatif qui forme une base pour de futures développements dans ce champ de recherches. Le succès de ce projet est aussi grandement dû à l'engagement sans fin du Prof. Dr. E. Klingelé qui a apporté une aide inestimable à tous les stages du projet. L'entreprise Ziegler Consultants, Zürich, et le laboratoire de topométrie, EPFL, ont substantiellement aidé aux mesures de vibrations respectivement inertielles. Le soutien non bureaucratique par le Dr. T. Niebauer de MicroG et le support de gestion par le swisstopo au cours des campagnes aéroportées sont vivement appréciés.

Par dessus tout ce projet a été un travail énorme et la Commission Suisse de Géodésie (SGC) félicite Monsieur H. Baumann pour ce travail de pionnier qui représente une contribution de la géodésie suisse à la communauté internationale. Ce projet a été supporté financièrement par l'ETH Zürich au travers du crédit TH 01803/19/99-4 et par la Commission Suisse de Géodésie. Nous sommes de plus reconnaissant à l'Académie suisse des sciences naturelles pour avoir pris à sa charge les coûts d'impression du présent fascicule.

Prof. Dr. H.-G. Kahle,
Prof. Dr. E. E. Klingelé
Institut de Géodésie et Photogrammétrie,
ETH Zürich

Prof. Dr. A. Geiger
ETH Zürich
Président de la CGS

Summary

This work consists of a feasibility study of a first stage prototype airborne absolute gravimeter system. In contrast to relative systems, which are using spring gravimeters, the measurements acquired by absolute systems are uncorrelated and the instrument is not suffering from problems like instrumental drift, frequency response of the spring and possible variation of the calibration factor. The major problem we had to resolve were to reduce the influence of the non-gravitational accelerations included in the measurements. We studied two different approaches to resolve it: direct mechanical filtering, and post-processing digital compensation.

The first part of the work describes in detail the different mechanical passive filters of vibrations, which were studied and tested in the laboratory and later in a small truck in movement. For these tests as well as for the airborne measurements an absolute gravimeter FG5-L from Micro-G Ltd was used together with an Inertial navigation system Litton-200, a vertical accelerometer EpiSensor, and GPS receivers for positioning. These tests showed that only the use of an optical table gives acceptable results. However, it is unable to compensate for the effects of the accelerations of the drag free chamber.

The second part describes the strategy of the data processing. It is based on modeling the perturbing accelerations by means of GPS, EpiSensor and INS data.

In the third part the airborne experiment is described in detail, from the mounting in the aircraft and data processing to the different problems encountered during the evaluation of the quality and accuracy of the results. In the part of data processing the different steps conducted from the raw apparent gravity data and the trajectories to the estimation of the true gravity are explained. A comparison between the estimated airborne data and those obtained by ground upward continuation at flight altitude allows to state that airborne absolute gravimetry is feasible and has a spatial resolution comparable to the one of the relative airborne gravimetry. For a wavelength on the order of 11 km the mean value of the resolution of the estimated gravity is 9.7 mGal.

Finally some suggestions are formulated for the improvement of the system which should simplify its use, increase the accuracy and reduce its price.

Zusammenfassung

Dieses Forschungsprojekt ist eine Machbarkeitsstudie über fluggestützte Absolutgravimetrie. Im Vergleich zu den relativen Messsystemen, die federgestützt Gravimeter einsetzen, sind die durch Absolut-Systemen erfassten Daten nicht korreliert. Ein Absolutgravimeter leidet nicht unter Problemen wie Drift, Eigenfrequenz der Feder oder Kalibration! Das Hauptproblem, das wir zu lösen hatten, war die Minimierung des Einflusses der nicht gravitativen Beschleunigungen. Dazu betrachteten wir zwei Ansätze: direkte mechanische Filterung, und digitale Post-Kompensierung.

Der erste Teil umfasst die Beschreibung von verschiedenen mechanischen Passiv-Filtern zur Dämpfung von Vibrationen. Diese Systeme wurden erst statisch im Labor und dann dynamisch in einem Lieferwagen getestet. Während den Tests wurde das Absolutgravimeter FG5-L von Micro-g Ltd., eingesetzt. Es wurde mit einem Inertial-Navigations-System Litton-200, einem Beschleunigungssensor EpiSensor und GPS Empfängern gekoppelt. Die Versuche zeigten, dass das beste Resultat mit einem Optik-Tisch erhalten wird. Allerdings können die durch die „drag-free“ Kammer erzeugten Störbeschleunigungen nicht verhindert werden.

Im zweiten Teil wird die Strategie beschrieben, die zur Datenverarbeitung eingesetzt wurde. Das Konzept beruht auf der Modellierung der Störbeschleunigungen mit Hilfe der GPS-, INS- und EpiSensor-Daten.

Im Teil 3 wird das Flug-Experiment im Detail beschrieben, vom Einbau in das Flugzeug über die Datenverarbeitung bis hin zur Evaluierung der Qualität der Resultate. Der Datenverarbeitungs-Teil erklärt die einzelnen Schritte, die es ermöglichen, ausgehend von den Rohdaten der gemessenen Scheinbeschleunigungen und Trajektorien die Schwerebeschleunigung schätzen zu können. Ein Vergleich zwischen den geschätzten Werten mit terrestrischen Messungen, die durch Feldfortpflanzung auf Flughöhe berechnet wurden, ermöglicht es, die Qualität des Experiments abzuschätzen. Die Schlussfolgerung dieses Vergleichs zeigt, dass die fluggestützte Absolutgravimetrie machbar ist, mit einer räumlichen Auflösung, die vergleichbar ist mit derjenigen der fluggestützten Relativgravimetrie. Für eine Wellenlänge von 11 km liegt der mittlere Wert der Auflösung der geschätzten Schwere bei 9.7 mGal.

Im Ausblick werden verschiedene Vorschläge präsentiert, die das System vereinfachen, seine Genauigkeit verbessern und die Kosten senken können.

Contents

1	INTRODUCTION	3
1.1	AIM OF THE PROJECT	4
1.2	ABOUT AIRBORNE ABSOLUTE MEASUREMENTS OF G.	4
2	AIRBORNE GRAVIMETRY	7
2.1	INTRODUCTION	7
2.2	THE MEASUREMENT OF G FROM AN AIRCRAFT	7
2.2.1	<i>The reference systems in terrestrial mechanics</i>	7
2.2.2	<i>Relative movements and inertial forces</i>	9
2.2.3	<i>Dynamics in the geocentric reference system, tidal forces</i>	12
2.2.4	<i>Dynamics in the terrestrial reference system, gravity</i>	13
2.2.5	<i>Dynamics in an aircraft, gravity measurements.</i>	14
2.2.6	<i>Determination of kinematic accelerations</i>	15
3	AIRBORNE GRAVITY SYSTEMS	19
3.1	EXISTING AIRBORNE GRAVITY SYSTEMS	19
3.2	INTRODUCTION	19
3.2.1	<i>The KSS31 system</i>	19
3.2.2	<i>The Bell BGM-3 system</i>	20
3.2.3	<i>The A/S system from LaCoste & Romberg</i>	20
3.3	AIRBORNE ABSOLUTE GRAVIMETRY SYSTEMS	22
3.3.1	<i>Introduction</i>	22
3.3.2	<i>Absolute gravimetry: basic concepts</i>	22
3.3.2.1	<i>The free-fall method</i>	22
3.3.2.2	<i>The measurement of time and distances</i>	24
3.3.3	<i>The FG5-L gravimeter</i>	27
3.3.3.1	<i>The determination of g</i>	28
3.3.3.2	<i>Principal characteristics of the FG5-L</i>	29
3.3.4	<i>The EpiSensor accelerometer</i>	29
3.3.4.1	<i>Working Principle</i>	29
3.3.4.2	<i>EpiSensor Specifications</i>	30
3.3.5	<i>Inertial Navigation System (LN 200)</i>	30
3.3.5.1	<i>Fiber-Optic Gyro</i>	32
3.3.5.2	<i>LN-200 IMU Specifications</i>	33
3.3.6	<i>The Instrument Platform</i>	34
3.3.7	<i>Conclusion</i>	34
4	THE DAMPING PLATFORMS	35
4.1	INTRODUCTION	35
4.2	ANALYSIS OF THE VIBRATIONS OF THE AIRCRAFT.	35
4.3	MECHANICAL SYSTEMS OF ABSORPTION	37
4.3.1	<i>Introduction</i>	37
4.3.2	<i>The active table MOD1-L from Halcyonics</i>	38
4.4	THE MULTI-LAYER TABLE	40
4.4.1	<i>Introduction</i>	40
4.4.2	<i>The experimental mounting</i>	41
4.4.3	<i>Determination of the transfer function of the multi-layer table</i>	42
4.4.4	<i>Application to the vibrations of the aircraft</i>	43
4.5	THE HANGING TABLE	44
4.5.1	<i>Introduction</i>	44
4.5.2	<i>The table</i>	45
4.5.3	<i>The determination of the transfer function</i>	46
4.5.4	<i>Application to the vibrations of the aircraft</i>	48
4.5.5	<i>The first dynamic test</i>	48

4.6	CONCLUSION	49
5	LABORATORY TESTS	51
5.1	INTRODUCTION	51
5.2	FAMILIARIZATION WITH THE FG5-L	51
5.3	FG5-L COMBINED WITH AN EPISENSOR AND SOFTWARE VALIDATION	54
5.4	INFLUENCE OF THE PLATFORMS	56
5.4.1	<i>Influence of the strap-down table</i>	56
5.4.2	<i>Influence of the platform the damping table</i>	58
5.5	DETAILED ANALYSIS OF A G MEASUREMENT IN LABORATORY	59
5.5.1	<i>Least squares adjustment</i>	59
5.5.1.1	Theory	59
5.5.2	<i>Statistical analysis</i>	63
5.5.3	<i>Frequency analysis</i>	65
5.5.4	<i>Analysis of the measurements carried out in the laboratory</i>	65
5.5.4.1	Analysis of the FG5-L components	65
5.5.4.2	Expected resolution for one single drop	66
5.5.4.3	Spectral analysis	68
5.6	CONCLUSIONS	70
6	FIRST DYNAMIC MEASUREMENT IN A TRUCK	71
6.1	INTRODUCTION	71
6.2	LOCATION OF THE TEST LINE	71
6.3	EXPERIMENTAL BUS-SETUP	71
6.4	MEASUREMENTS IN STRAP-DOWN CONFIGURATION	73
6.4.1	<i>Static measurements</i>	73
6.4.2	<i>Measurement in dynamic mode</i>	86
6.5	MEASUREMENTS WITH THE HANGING TABLE	92
6.5.1	<i>Discussion</i>	97
7	THE AIRBORNE TEST SURVEY	99
7.1	INTRODUCTION	99
7.2	THE AIRCRAFT	99
7.3	LOCATION OF THE TEST SURVEY	101
7.4	THE POSITIONING OF THE AIRCRAFT	102
7.5	EXPERIMENTAL MOUNTING AND MEASUREMENTS	104
7.6	DATA ACQUISITION DURING THE FLIGHT	105
8	PROCESSING OF THE AIRBORNE GRAVITY DATA	107
8.1	PROCESSING OF THE GPS DATA.	107
8.1.1	<i>Single difference equation of observation</i>	107
8.1.2	<i>Strategy for the GPS data processing in kinematics mode</i>	109
8.1.3	<i>Accuracy of the kinematics variables computed with GPS data</i>	111
8.2	PROCESSING OF THE GRAVITY DATA	117
8.2.1	<i>Upward continuation of the ground data</i>	117
8.2.2	<i>Analysis of the perturbing accelerations produced by the aircraft</i>	119
8.2.3	<i>Estimation of the apparent acceleration A_{app} for a single fall.</i>	123
8.2.4	<i>Correction of the functions $A_{apparent}(x(t), y(t), z(t))$</i>	129
9	CONCLUSIONS AND RECOMMENDATIONS	135

1 Introduction

A good knowledge of the Earth's gravity field allows, in principle, to monitor the temporal and spatial evolution of the Earth. The spatial variations of g are due to the lateral distribution of masses whereas the temporal variations are the result of transfer of masses (magma, water, atmosphere, etc). In metrology the value of g is used for defining units like force and pressure whereas in oceanography the temporal variation of gravity is used for developing models of the earth tides.

In geodesy gravity is used for determining the geoid and for computing orthometric heights. In geophysics the comparison between the measured gravity field and its theoretical value defines the so called gravity anomaly, which reflects the geological structure of the Earth. This is of particular interest for mineral, natural gas and oil prospecting.

Until today billions of gravity measurements were carried out on land, offshore and also on the sea bottom. However, these measurements are limited because of the difficult access of deserts, rain forests, high mountains or large areas covered by glaciers like Antarctica.

The spectacular technical progress of the last twenty years allowed initiating programs dealing with gravity measurements by using satellites (SEASAT, GEOS-3, GEOSAT, ERS-1, TOPEX/POSEIDON, ERS-2). With the data obtained from these different programs it was possible for the first time to determine global gravity anomalies with wavelength between some hundred to some thousand km.

Due to the intrinsic technique of measurement, the ground and offshore data cover the wavelengths extending from meters to some kilometers.

Even combining spatial and ground measurements the Earth will never be covered with data having wavelengths between ten and some hundred kilometers; even worse, many areas will remain uncovered with wavelengths smaller than 200 km.

Fortunately thanks to the development of GPS positioning airborne gravity became industrially possible.

Terrestrial field gravimetry is essentially based on spring-type gravity meters. This type of instrument determines the difference of gravity between two points by measuring the elongation of a spring, which holds a test mass. The difference in the restoring force of the spring is directly related to the difference in gravity. High sensitivity (on the order of 10^{-9} g) and repeatability are the main advantages of spring-type gravimeters. Drift, frequency response of the spring, and the need of calibration are the main disadvantages. Spring-type gravimeters have been primarily designed for land measurements.

The measurements of gravity from a moving platform are complicated because of the superposition of gravitational and non-gravitational accelerations, the duration of the measurements (which limits the spatial resolution) and the verticality of the platform itself.

Spring-type gravimeters have been designed for ship-borne measurements and only recently for airborne ones. Non-gravitational accelerations mainly depend upon the motion of the ship or airplane and can be orders of magnitude higher than the gravity anomalies. The final accuracy of the measurement of the acceleration due to gravity is, therefore, limited by the accuracy of the measurement of the motion of the moving platform. The development of kinematic GPS has allowed measuring the motion of a body in space with high accuracy. The problem of separating gravitational from non-gravitational accelerations is, therefore, correctly addressed even if it may still need some efforts. It is worthwhile now to devote a particular effort in the development of new airborne gravity sensors.

1.1 Aim of the project

The aim of our project was to develop a new airborne gravity measurement system (AAG), which should provide absolute values of the Earth's gravitational acceleration and its anomalies and which would not be influenced by instrumental disturbing effects like drifts and tares. To be useful and commercially interesting such a system has to have at least the same performances as the airborne relative gravimeters. In other words an airborne absolute gravimeter should reach the resolution of some milliGal at wavelengths shorter than ten kilometers required in applied geophysics and in geodesy.

We planned to use a modified small version of a land-based absolute gravimeter for use on board of an aircraft and use Global Positioning System (GPS) and Inertial Navigation System (INS) data to remove aircraft disturbing accelerations. It is the first attempt worldwide to measure absolute gravity on board of an aircraft. The absolute gravimeter employs a laser interferometer that measures the free fall trajectory of an optical element within an evacuated chamber. Standards for length and time are provided by atomic references, which provide high accuracy and stability. Such a system is therefore drift free and quasi insensitive to horizontal accelerations. In principle it is able to perform measurements at a rate of 2 seconds. Another advantage of absolute gravimetry is that the measurements are uncorrelated, which means that a sporadic perturbation like a shock will affect only the actual measurement and not the following ones as is the case with a spring type gravimeters measuring in a relative mode.

Although the principle of such a technique seems to be straightforward many huge technical obstacles arose during the development of the instrument, during the airborne measurements and last but not least during the data processing. In fact the results of this research will give answers to the following fundamental questions:

- **Is absolute airborne gravimetry feasible at all?**
- **Which accuracy can we expect from these measurements?**
- **What are the advantages and disadvantages of this technique with respect to the classical ones?**
- **Which are the necessary improvements to be made to the system in order to make it useful for routine measurements?**

1.2 About airborne absolute measurements of g .

In order to determine the Earth's gravity field from an airplane the system has to have one sensor measuring the sum of all vertical accelerations and one sensor allowing to measure the vertical accelerations caused by the movements of the aircraft. These accelerations are due to the turbulence, the vertical components of the Coriolis force as well as to the engines.

Until today, to our knowledge, nobody has tried to install and to measure the absolute value of g in an aircraft. Since no such experience can be found in any scientific publication we will begin by describing the general principles of this kind of experiment

Some work was carried out in the domain of the compensation of non-gravitational accelerations perturbing the absolute measurements. For the compensation there are two ways of realizing it: either by isolating the system from external vibrations by using a mechanical filter (active or passive) or by measuring these vibrations separately and by subtracting them during data processing.

In the 80ies a new portable absolute gravimeter was developed at JILA (Joint Institute for Laboratory Astrophysics) (Zumberge et al. 1982). This instrument determines the g value by

measuring the position of a falling body as a function of time by means of a Michelson interferometer. In order to isolate the reference mirror from the vibration a new kind of mechanical filter was developed, the Super Spring. This system with a cut-off frequency of about 0.015 Hz consist of an electronically synthesized spring (*Zumberge et al. 1982, R.L. Rinker, 1983, P.G. Nelson, 1991*)

In 2000 J. Brown from micro-g, Inc. began to study the problem of compensating the vibration in view of an application in dynamic mode (*Brown et al. 2000*). The method proposed is to measure the external acceleration by means of a very sensitive seismometer and then to introduce these data as observations in the system of equations governing the determination of g . The results obtained in the laboratory are very convincing and we surmised that it could be used for our experiments. A similar approach as already been used by Canuteson (*Canuteson et al. 1996, 1997*) but the technique of J. Brown had the advantage that it has been developed for a gravimeter similar with the one we used.

2 Airborne gravimetry

2.1 Introduction

The most difficult part of airborne gravimetry is to separate the gravity from vertical accelerations due to the variations of the trajectory of the airplane, the vibrations induced by the rotation of the engines and the vertical component of the Coriolis acceleration. This chapter is dedicated to the problems linked to the determination of g from an aircraft. It starts by studying the basic equations, of relative movements, which will be applied to the measured values. After having described the airborne system all the components necessary for an absolute airborne system will be summarized. At the end of this chapter the theory of the essential components for the determination of g from a moving platform will be available.

2.2 The measurement of g from an aircraft

Airborne gravimetry is a typical case of relative movements between two different reference systems. If both reference systems have uniform and rectilinear movements the classical laws of mechanics formulated by Newton are equivalent for both systems. However, in practice any system called « inertial » is only an approximation because due to the movement of the Earth any body attached to this system is submitted to the gravitational acceleration of the Sun and the planets. Since the reference system used in terrestrial mechanics is not strictly inertial it is necessary to add some correcting terms to the resultant force, which take into account the relative movement between the reference systems.

2.2.1 The reference systems in terrestrial mechanics

In the following a short description of the principal reference systems, used in terrestrial mechanics, will be given. These systems are illustrated in Figure 2-1 and Figure 2-2.

The Copernican reference system:

The Copernican reference system (R_I) is a quasi-inertial system with its origin at the center of the mass of the solar system. It is a Cartesian system with its axis oriented in the direction of fixed stars.

Terrestrial reference system:

It is a Cartesian reference system rigidly tied to the Earth (R_T) with its origin at the center of mass of the system Earth-Atmosphere. The Z-axis corresponds to the mean rotation axis of the Earth whereas the X-axis and Y-axis are located in the equatorial plane with X crossing the meridian of Greenwich. Since the rotation axis of the Earth is subject of precession and nutation this system has to be materialized by ground reference stations, which are referenced with respect to celestial bodies. The most widely known terrestrial systems are the ITRF (International Reference System) and the WGS-84 (World Geodetic System).

Local reference systems:

A local reference system (R_L) is a system, which can be defined in any point P at the surface of the Earth. Its Z -axis corresponds to the direction of g at the point P and the X and Y form a tangent plane to the equipotential surface at the same point. The X -axis points towards the geographic North and the Y -axis points towards East. In order to be able to define such a system it is necessary to know the direction of g at each point at the surface of the Earth! In practice one constructs a model of the Earth's gravity field, which allows a mathematical description of the Earth's ellipsoid. In this manner the Z -axis corresponds to the normal of the ellipsoid.

In the frame of this project we will use, for defining the position of a point P , the terrestrial reference system $WGS-84$ in which P is fully defined by its geographical coordinates: latitude, longitude and ellipsoidal height (λ, φ, h). In this manner it is possible to form a base $(\vec{u}_E, \vec{v}_N, \vec{n})$ in $P(\lambda, \varphi, h)$, which is commonly called « local geographic reference system »

Geocentric reference system:

This system (R_G) is a Cartesian reference system with its origin at the center of masse of the Earth. This system has a translation movement with respect to the Copernican reference system. It is materialized by the observation of celestial bodies with invariant positions.

Measurement reference system:

This system, (R_M), corresponds to the reference system into which each measuring instrument located inside the moving platform works.

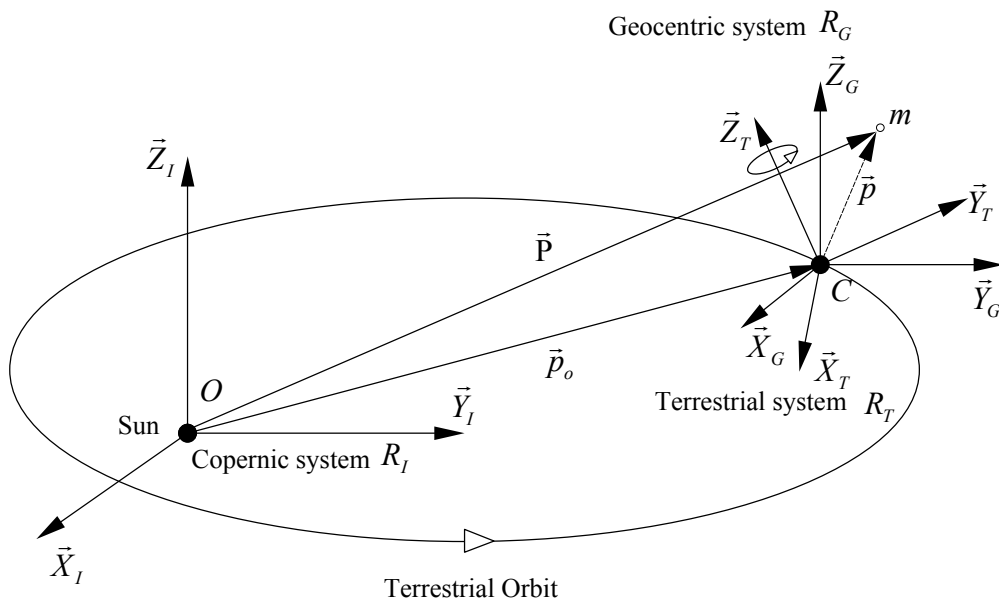


Figure 2-1: The principal reference systems used in celestial and terrestrial mechanics. The Copernican system R_C or R_I , the geocentric R_G system with its translation with respect to R_C , and the terrestrial system R_T with its origin at the same point as R_C and rotating around Z_T . m : moving mass with geocentric vector \vec{p} .

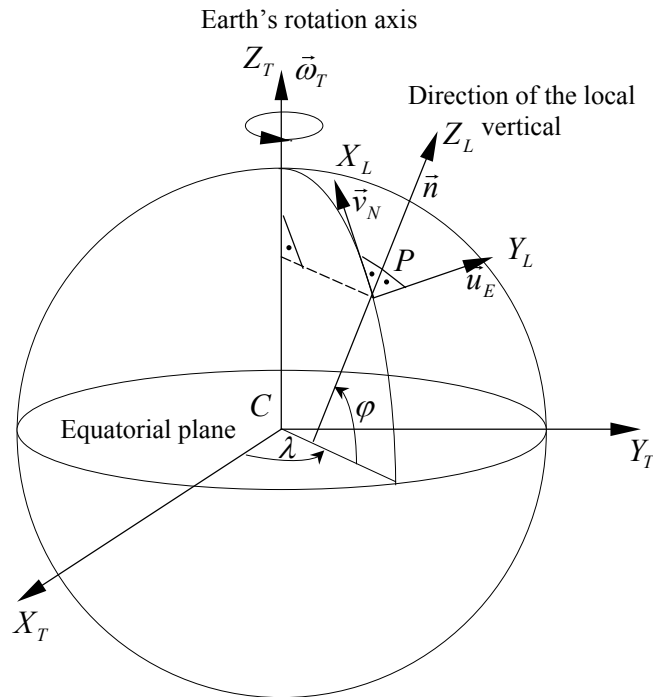


Figure 2-2: Definition of the reference system of the local gravity field R_L . The three unit vectors $\vec{u}_E, \vec{v}_N, \vec{n}$ are defining the local base at the point $P(\lambda, \varphi, h)$ referred to the ellipsoid.

2.2.2 Relative movements and inertial forces

The data we compare are all determined in different reference systems. We have to describe a physical phenomenon defined in an accelerated reference system in a fixed one. For this we use only the classical description, which is sufficient for our application.

In two systems Σ and Σ' , shown in Figure 2-3, in relative uniform and rectilinear movements the fundamental law of mechanics holds.

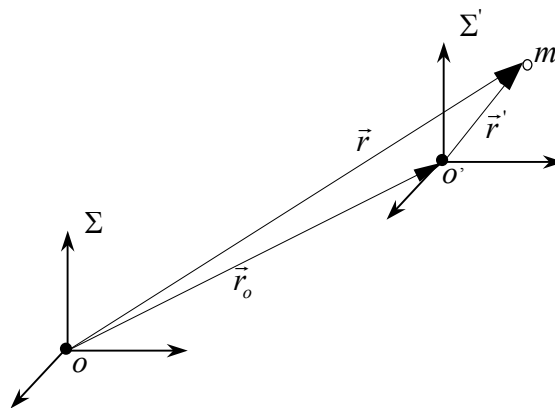


Figure 2-3: Reference systems in relative uniform and rectilinear movements.

On the other hand this is not the case if the system Σ' is accelerated with respect to the system Σ shown in Figure 2-4. The moving system Σ' is not an inertial system and the fundamental laws of mechanics are not valid anymore.

For a better understanding we look at the modifications introduced by the acceleration of the system Σ' which has a velocity $v_o(t)$ and $\omega(t)$ when seen from Σ .

The variations of any vector \vec{q} during a given time dt being $d_a\vec{q}$ seen from Σ and $d\vec{q}$ from Σ' , one obtains:

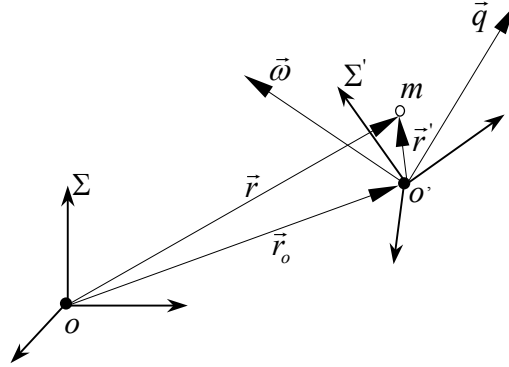


Figure 2-4: Non inertial reference system Σ' accelerated with respect to Σ

$$d_a q = dq + v_{(\text{due to the rotation})} dt$$

So:

$$\boxed{\frac{d_a \vec{q}}{dt} = \frac{d\vec{q}}{dt} + \vec{\omega} \times \vec{q}} \quad (2.1)$$

The relationship (2.1) is valid for every \vec{q} . For determining the acceleration of \vec{r}' , it is sufficient to replace \vec{q} by \vec{r}' and to apply the above general relationship (2.1) twice:

$$\begin{aligned} \frac{d^2 \vec{r}'}{dt^2} &= \left(\frac{d}{dt} + \vec{\omega} \times \right) \left(\frac{d\vec{r}'}{dt} + \vec{\omega} \times \vec{r}' \right) = \\ &= \frac{d^2 \vec{r}'}{dt^2} + \frac{d\vec{\omega}}{dt} \times \vec{r}' + \vec{\omega} \times \frac{d\vec{r}'}{dt} + \vec{\omega} \times \frac{d\vec{r}'}{dt} + \vec{\omega} \times (\vec{\omega} \times \vec{r}') \end{aligned}$$

Because $\vec{r}' = \vec{r} - \vec{r}_o$, one finally obtains:

$$\boxed{\frac{d_a^2 \vec{r}}{dt^2} = \frac{d^2 \vec{r}_o}{dt^2} + \frac{d^2 \vec{r}'}{dt^2} + \frac{d\vec{\omega}}{dt} \times \vec{r}' + \vec{\omega} \times (\vec{\omega} \times \vec{r}') + 2\vec{\omega} \times \frac{d\vec{r}'}{dt}} \quad (2.2)$$

Taking into account that $\vec{F} = m \frac{d^2 \vec{r}}{dt^2}$, the fundamental law for non-inertial system in movement can be written:

$$\boxed{m \frac{d^2 \vec{r}'}{dt^2} = \vec{F} + \vec{F}_{entr.} + \vec{F}_{centr.} + \vec{F}_{Cor.}} \quad (2.3)$$

In this equation three supplementary terms appear to the resultant of the external forces that are called « inertial forces ». The first one, which remains even when the angular velocity $\vec{\omega}$ is equal to zero, is due to the driving of the body in the accelerated translating movement of the reference system. The second is the centrifugal force due to the rotation and the third one, also called Coriolis force, appears due to the presence of the relative velocity \vec{v}' :

$$\vec{F}_{entr.} = -m \frac{d^2 \vec{r}_o}{dt^2} \quad (2.4)$$

$$\vec{F}_{centr.} = -m \left(\frac{d\vec{\omega}}{dt} \times \vec{r}' + \vec{\omega} \times (\vec{\omega} \times \vec{r}') \right) \quad (2.5)$$

$$\vec{F}_{Cor.} = -2m(\vec{\omega} \times \vec{v}') \quad (2.6)$$

These inertial forces have to be introduced only for an observer tied to the moving system.

2.2.3 Dynamics in the geocentric reference system, tidal forces

In order to determine the influence of the tidal forces we will study the movement of a mobile in \vec{p} with a mass m in the geocentric reference system, R_G (Figure 2-1).

The geocentric reference system R_G , being in translation with respect to the Copernican reference system R_C , the unique inertial force that we have to take into account is the driving force where the vector \vec{p}_o , corresponds to the vector linking the origins O and C , of the two systems.

The forces acting on m are, on one side the gravitational forces produced by the Earth and other celestial bodies and on the other side, the non-gravitational forces.

In the geocentric reference system R_G , it is then possible to describe the movement of m in \vec{p} by:

$$m\vec{a}_{R_G}(\vec{p}) = m\vec{G}_{Earth}(\vec{p}) + \vec{F}_{Non-grav}(\vec{p}) + m\vec{G}_{Celest.}(\vec{p}) - m\vec{a}_{R_I}(C) \quad (2.7)$$

With:

- m : Mass of the moving object in \vec{p}
- \vec{a}_{R_G} : Acceleration with respect to R_G
- \vec{a}_{R_I} : Acceleration with respect to R_I
- \vec{G}_{Terre} : Gravitational acceleration of the Earth
- $\vec{G}_{Celest.}$: Gravitational acceleration of other celestial bodies
- $\vec{F}_{Non-grav}$: Resulting forces of non-gravitational forces

The acceleration \vec{a}_{R_I} corresponds to the acceleration felt by the center of masse of the Earth in the Copernican reference system R_I . The movement of the Earth is due to the gravitational forces of all the celestial bodies. However, the largest influences come from the Moon and the Sun. On the Earth every element of mass dm in \vec{p} is submitted to a gravitational force $dm\vec{G}_{Celest.}(\vec{p})$. Then we can write by integrating over the elements of masse dm :

$$\int \vec{a}_{R_I}(\vec{p})dm = \int \vec{G}_{Celest.}(\vec{p})dm$$

The left part of the above equality represents the acceleration of the center of mass of the Earth multiplied by the Earth's mass M_{Earth} .

$$\int \vec{a}_{R_I}(\vec{p})dm = M_{Earth}\vec{a}_{R_I}(C)$$

Making the hypothesis that all the elements of masses are submitted to a constant gravitational acceleration, it is possible to write:

$$\int \vec{G}_{Celest.}(\vec{p})dm \approx \vec{G}_{Celest.}(C) \int dm = M_{Earth}\vec{G}_{Celest.}(C)$$

Finally one gets: $\vec{a}_{R_t}(C) = \vec{G}_{Celest.}(C)$

And (2.7) can be re-written as:

$$m\vec{a}_{R_G}(\vec{p}) = m\vec{G}_{Earth}(\vec{p}) + \vec{F}_{Other}(\vec{p}) + m(\vec{G}_{Celest.}(\vec{p}) - \vec{G}_{Celest.}(C)) \quad (2.8)$$

In (2.8) a differential term $\vec{G}_{Celest.}(\vec{p}) - \vec{G}_{Celest.}(C)$ appears. This is called the “tidal force”, which is responsible for the periodic deformation of the solid Earth and the oceans. It does not exceed 0.2 mGal (Klingelé et al., 1996), and can therefore be neglected. Neglecting this term corresponds to considering the movement of the Earth as uniform and rectilinear and consequently to assimilate the geocentric reference system as an inertial system.

2.2.4 Dynamics in the terrestrial reference system, gravity

Looking at the dynamics of a motionless body of masse m at a point \vec{p} on Earth, we see, that after (2.3), the only term to be retained, neglecting the tidal force, is the term describing the rotation of the Earth around the mean polar axis, that is the centrifugal force.

Considering the angular velocity as constant ($\omega = 7.292115 \times 10^{-5} \text{ rad} \cdot \text{s}^{-1}$, Torge, 1991) one can write:

$$\vec{F}_{centr.} = -m(\omega \times (\omega \times \vec{p}))$$

To keep the system in equilibrium the sum of the forces has to be equal to zero, which can be written as:

$$m\vec{a}_{R_t}(\vec{p}) = m\vec{G}_{Earth}(\vec{p}) + \vec{F}_{other}(\vec{p}) - m(\omega \times (\omega \times \vec{p})) = \vec{0}$$

Consequently in order to maintain a body in equilibrium on the Earth it is necessary to apply to it a force equal but in the opposite direction to the sum of the gravitational and the centrifugal forces. This force corresponds to the product of the inertial mass of the body by the gravitational acceleration $\vec{g}(p)$. Then:

$$-\vec{F}_{other} = m\vec{g}(\vec{p}) = m\vec{G}_{Earth}(\vec{p}) - m(\omega \times (\omega \times \vec{p}));$$

Setting:

$$\boxed{\vec{g}(p) = \vec{G}_{Earth}(p) - \omega \times (\omega \times \vec{p})} \quad (2.9)$$

Equation (2.9) corresponds to the **gravity field**. In fact most of the instruments measuring gravity determine the **antagonistic** force \vec{F}_{other} .

2.2.5 Dynamics in an aircraft, gravity measurements.

Now it is necessary to write the law of dynamics allowing the determination of the gravity from an aircraft in motion. For that we have to consider a moving body of masse m located at a point \vec{p} on board of an airplane. Let us make the hypothesis that the measurement reference system R_M corresponds to the local reference system R_L . In the geocentric reference system R_G , the law of dynamics can be expressed by:

$$m\vec{a}_{R_G}(\vec{p}) = m\vec{G}_{Earth}(\vec{p}) + m\vec{F}_{Other}(\vec{p})$$

According to (2.9), it is possible to write:

$$\vec{G}_{Earth}(\vec{p}) - \vec{a}_{R_G}(\vec{p}) = \vec{g}(\vec{p}) - \vec{\omega}_T \times (\vec{\omega}_T \times \vec{p}) - \vec{a}_{R_G}(\vec{p})$$

Whereby $\vec{\omega}_T$ is the vector of angular velocity of the rotation of the Earth with respect to the geocentric reference system R_G . The acceleration seen from the geocentric reference system in the terrestrial reference system can be written, after (2.2):

$$\vec{a}_{R_G}(p) = \frac{d^2 \vec{p}_{R_T}}{dt^2} + 2\vec{\omega} \times \frac{d\vec{p}_{R_T}}{dt} + \vec{\omega}_T \times (\vec{\omega}_T \times \vec{p})$$

Expressing $\frac{d^2 \vec{p}_{R_T}}{dt^2}$ as a function of the ground velocity, in the terrestrial reference system R_T one gets:

$$\frac{d^2 \vec{p}_{R_T}}{dt^2} = \dot{V}_E \vec{u}_E + \dot{V}_N \vec{v}_N + \ddot{h} \vec{n} + \vec{\omega}_L \times \vec{V}_{Flight}(\vec{p})$$

Whereby $\vec{\omega}_L$ is the vector of angular velocity of rotation of the local reference system with respect to the terrestrial system.

$$\dot{V}_E \vec{u}_E + \dot{V}_N \vec{v}_N + \ddot{h} \vec{n} = \dot{\vec{V}}_{Flight}(\vec{p})$$

This allows us to write the final form of the apparent gravity $\vec{P}_{apparent}$ measured in the aircraft

$$\boxed{\vec{P}_{apparent} = \vec{g}(\vec{p}) - [\dot{\vec{V}}_{Flight}(\vec{p}) + (2\vec{\omega}_T + \vec{\omega}_L) \times \vec{V}_{Flight}(\vec{p})]} \quad (2.10)$$

Formula (2.10) is the basic expression for the measurement of g on board of a moving platform (aircraft). This expression contains two parts: the real gravity $\vec{g}(\vec{p})$ on one side, and the sum of all non-gravitational accelerations $\vec{A}_{cin} = \dot{\vec{V}}(p) + (2\vec{\omega}_T + \vec{\omega}_L) \times \vec{V}_{Flight}(p)$, which are tied to the movement of the aircraft, on the other side.

One of the biggest difficulties is to separate the two terms in order to get the value of g . This separation can be done either by filtering, mechanically or numerically or by modeling it and subtracting it from the total acceleration.

In a simplified manner (2.10) can be written:

$$\boxed{\vec{P}_{\text{apparent}} = \vec{g}(p) - \vec{A}_{\text{cin}}(p)} \quad (2.11)$$

2.2.6 Determination of kinematic accelerations

In the frame of this project we will focus our attention to the intensity of the gravity field $g(p)$ at a point p . $g(p)$ is a scalar value defined by $\vec{g}(p) = -g(p)\vec{n}_{\text{true}}$, where \vec{n}_{true} corresponds to the unit zenith vector pointing toward the local vertical. In order to be able to determine the kinematics accelerations we will make the approximation that the local vertical is parallel to the normal of the ellipsoid ($\vec{n} \approx \vec{n}_{\text{true}}$). This is justify, because, if we assume that the deflection of the vertical does not exceed $\varepsilon = 30''$ on the surface of the Earth, the relative error on the static measurement g_{measured} is given by:

$$g_{\text{measured}} = g \cos(\varepsilon) \approx g \left(1 - \frac{\varepsilon^2}{2}\right) \quad \Rightarrow \quad \frac{g - g_{\text{measured}}}{g} = \frac{\varepsilon^2}{2} = 10^{-8}$$

Then for $g_{\text{measured}} = 9.80 \text{ ms}^{-2}$, the error is $\delta g = 9.80 \cdot 10^{-8} \text{ ms}^{-2}$ which is much less than the accelerations produced by the movements of the aircraft. Consequently this approximation can be used without restriction.

From (2.11), and using our approximation we can write:

$$\vec{P}_{\text{apparent}} = (-g(p) - A_{\text{cin}_n}(p))\vec{n} = -\vec{P}_{\text{apparent}}\vec{n} \quad \Rightarrow \quad \vec{P}_{\text{apparent}} = g(p) + A_{\text{cin}_n}(p)$$

Projecting \vec{A}_{cin} on \vec{n} , one obtains A_{cin_n}

$$(\dot{\vec{V}}_{\text{Flight}}(p) + (2\vec{\omega}_T + \vec{\omega}_L) \times \vec{V}_{\text{Flight}}(p)) \cdot \vec{n}$$

In the local base system $(\vec{u}_E, \vec{v}_n, \vec{n})$ the global rotation's vector can be decomposed in the following manner:

$$2\vec{\omega}_T + \vec{\omega}_L = \begin{bmatrix} -\dot{\varphi} \\ (2\omega_T + \dot{\lambda}) \cos(\varphi) \\ (2\omega_T + \dot{\lambda}) \sin(\varphi) \end{bmatrix}$$

We then obtain for $Acin_n$:

$$Acin_n(p) = \ddot{h} - (V_N \dot{\varphi} + V_E (2\omega_T + \dot{\lambda}) \cos(\varphi)) = \ddot{h} - E(p)$$

Where E is the Eötvös correction.

The basic relationship, which gives the intensity of gravity in airborne gravimetry, can then be written as:

$$g(p) = P_{\text{apparent}} + E(p) - \ddot{h}$$

The Eötvös corrections can be written as a function of the flight parameters V_E , V_N and h as follow:

$$\begin{aligned} V_E &= (N(\varphi) + h) \cos(\varphi) \dot{\lambda} \\ V_N &= (M(\varphi) + h) \dot{\varphi} \end{aligned}$$

Where $N(\varphi)$ and $M(\varphi)$ are the principal radius of curvature normal and meridian at the point p , respectively.

Calling $f = \frac{a-b}{a}$ the ellipsoidal flattening, with a and b major respectively minor axis of the ellipsoid, the Eötvös correction can be written (Torge, 1991)

$$E(p) = \frac{V^2}{a} \left[1 - \frac{h}{a} - f(1 - \cos^2(\varphi)(3 - 2\sin^2(\alpha))) \right] + 2V\omega_T \cos(\varphi) \sin(\alpha)$$

Where $V^2 = V_E^2 + V_N^2$, and where α represents the flight azimuth so that $V_E = V \sin \alpha$ and $V_N = V \cos \alpha$

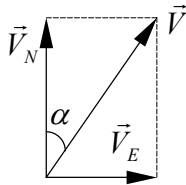


Figure 2-5: Definition of the azimuth α

Using the speed of the aircraft projected to the Earth's surface and writing $V_{\text{Earth}}^2 = V_{E_{\text{Earth}}}^2 + V_{N_{\text{Earth}}}^2$ the relationship becomes (Harlan, 1968):

$$E(p) = \frac{V_{\text{Earth}}^2}{a} \left[1 + \frac{h}{a} - f(1 - \cos^2(\varphi)(3 - 2\sin^2(\alpha))) \right] + 2V_{\text{Earth}}\omega_T \cos(\varphi) \sin(\alpha) \left(1 + \frac{h}{a}\right)$$

Consequently all kinematic accelerations can be determined from the values of the coordinates, (λ, φ, h) , the first derivatives with respect to the time of the longitude and the latitude, $\dot{\lambda}$ and $\dot{\varphi}$, and the vertical acceleration \ddot{h} of the aircraft.

In conclusion in order to be able to determine g from a flying platform (aircraft) it is necessary to have a very accurate positioning system in addition to the gravimeter allowing the computation of the disturbing accelerations.

3 Airborne gravity systems

3.1 Existing airborne gravity systems

3.2 Introduction

Three measuring systems are used in airborne gravimetry (Neumeyer et Hehl, 1995). These are: the BGM-3 from *Bell Aerospace (Buffalo, N.Y.)*, the KSS31 from *Bodenseewerke Geosystem GmbH (Überlingen)*, and the A/S system from *LaCoste & Romberg Gravity Meters (Austin, Texas)*. They all are relative measuring systems, based on the classical mechanical spring system.

The difference between the systems is found in the movement of the mass: In the first two systems the movement is truly vertical (vertical spring) whereas in the third system the movement is in form of an arc of circle (mass attached to a beam).

All three systems are mounted on a stabilized platform in order to eliminate the effect of tilting caused by the roll and the pitch of the aircraft. The platform is held in horizontal position by a pair of gyroscopes feeding signals to torque motors. In the next chapters we will shortly describe these three systems and explain their principles of measurements.

3.2.1 The KSS31 system

Figure 3-1 depicts the working principle of the sensor used in the KSS31 system.

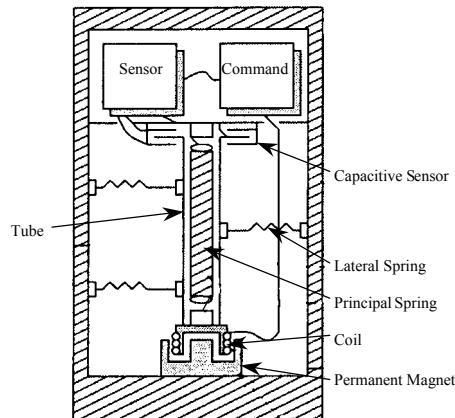


Figure 3-1: Schematic principle of the KS31 sensor after Torge 1989. In the middle of the picture one can distinguish the suspended tube guided vertically by the lateral springs. At the top of the tube is the capacitive sensor that detects the tube movements, and at the bottom is the coil moving in the magnetic field of the permanent magnet.

The movements of the mass (a tube) are detected by a capacitive sensor, which supplies a current to a coil by means of control loop. This coil located at the end of the tube in the magnetic field of a permanent magnet generates the supplementary magnetic field for restoring the static equilibrium of the mass. The restoring current, that is proportional to the variation of the apparent gravity, is then recorded. To minimize the environmental influences, the whole system is enclosed in a pressurized and thermostated box.

3.2.2 The Bell BGM-3 system

The mass formed of a coil is maintained in equilibrium between two poles of equal polarity of two permanent magnets as depicted in Figure 3-2. The movement of the mass is detected by a capacitive system, which supplies a current to the coil-mass through a control loop. The current in the coil-mass produces a magnetic field, which interacts with the one of the permanent magnet and tends to restore the static position of the mass. Like in the KS31 system the restoring current is calibrated and the whole system is enclosed in a pressurized and thermostated box.

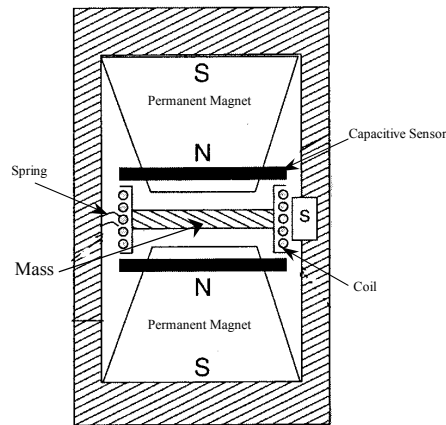


Figure 3-2: Schematic principle of the Bell BGM-3 sensor. Between the two permanent magnets, is the mass to which the coil is fixed. The capacitive sensor, depicted in black detects the movement of the mass that is attached to the spring.

3.2.3 The A/S system from LaCoste & Romberg

The LaCoste and Romberg Air-Sea gravity meter consists of a highly damped, spring-type gravity sensor mounted on a gyro stabilized platform with associated electronics for obtaining gravity readings. The basic equation of the LaCoste & Romberg S/A gravimeter is given by (3.1)

$$g_{airborne} = \left[K_1 S(t) + K_2 \frac{dB}{dt} \right] K_3 + CC(t) \quad (3.1)$$

$S(t)$: Position of the attachment point

$B(t)$: Positon of the bean

$CC(t)$: Cross - coupling term

K_1, K_2, K_3 : Calibration factors

The quantity $g_{airborne}$ corresponds to the complete vertical acceleration measured in airborne configuration. The term $K_1 S(t)$ represents the restoring force acting on the spring that is adjusted mechanically by moving the attachment point S . The S/A gravimeter is equipped with a motorized system, which allows the adjustment of the position of S (see Figure 3-3). A regulation loop determines the position of the beam and drives the motor in such a manner that the beam is kept in its rest position.

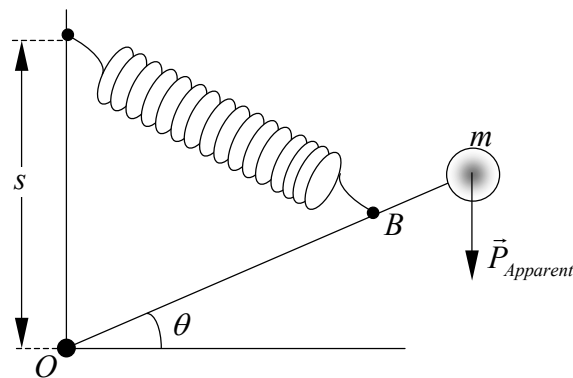


Figure 3-3: Schematic representation of the beam. S and B are the tow attachment points that are respectively used to describe the restoring force and the movement from the beam.

The term $K_2 \frac{dB}{dt}$ is proportional to the velocity of the beam, and the factors K_1 and K_3 are calibration factors. The gravimeter is equipped with a capacitive system (CPI, Capacitive Position Indicator), which ensures a continued measure of the beam position (see Figure 3-4). This signal is then used by the regulation loop described for keeping the beam in central position whereas the velocity of the beam is estimated by simple differentiation. Finally, $CC(t)$ corresponds to the cross-coupling term that takes into account the horizontal accelerations.

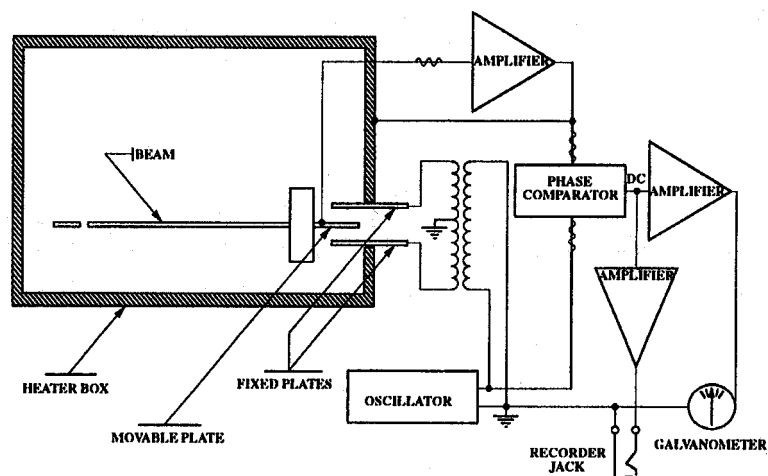


Figure 3-4: Schematic principle of the capacitive system (CPI, Capacitive Position Indicator) from the S/A gravimeter of LaCoste & Romberg. On distinguish the capacitive bridge formed by tow fixed plates and a moving one that is attached to the beam. Each movement from the beam induce a variation in the capacitive bridge, which is detected by the phase comparator.

3.3 Airborne absolute gravimetry systems

3.3.1 Introduction

The absolute airborne system used in our experiment is formed of five distinct units with a well-defined function each.

The core of the system is the absolute gravimeter FG5-L that allows the determination of the apparent gravity $P_{apparent}$. In order to determine the perturbing accelerations (non gravitational) the system is equipped with a vertical seismometer Episensor from Kinematics SA, with an Inertial Navigation Unit INU LN-200 from Litton and with four NAVSTAR GPS receivers. A fifth receiver is permanently located at a ground station and serves as reference for the positioning. The last but not the least element is the table on which the gravimeter, the seismometer and the INU are fixed. This table is necessary first for attenuating the vibration produced by the engines of the aircraft and second for maintaining the system parallel to the local vertical.

3.3.2 Absolute gravimetry: basic concepts

The aim of absolute gravimetry is to measure the value of the Earth's gravity field at desired discrete points. It is based on the measurement of two fundamental variables the time and the length, allowing the computation of the Earth's vertical acceleration. The most modern method to do it is to observe the vertical movement of a body falling freely in the Earth's gravity field.

3.3.2.1 The free-fall method

The mathematical formulation of the free-fall is given by:

$$m\ddot{z} = mg(z) \quad (3.2)$$
$$\ddot{z} = \frac{d^2 z}{dt^2}$$

Where:

m : mass of the falling body

z : position of the free - falling body

\ddot{z} : acceleration of the free - falling body

g : Earth's vertical acceleration

t : time

Under the hypothesis that the gravity field is homogeneous along the falling path one obtains the velocity and the position of the falling body by integrating equation (3.2)

$$\dot{z} = \dot{z}_0 + gt$$
$$\dot{z} = \frac{dz}{dt}$$

$$z = z_0 + \dot{z}_0 t + \frac{g}{2} t^2$$

Where \dot{z}_0 and z_0 are the velocity and the position respectively for the initial time $t = t_0 = 0$.

From the theoretical point of view, three couples of time-position $(t_i, z(t_i))$, $i = 1, 2, 3, \dots$ are enough for solving g

$$g = 2 \cdot \frac{(z_3 - z_1)(t_2 - t_1) - (z_2 - z_1)(t_3 - t_1)}{(t_3 - t_1)(t_2 - t_1)(t_3 - t_2)} \quad (3.3)$$

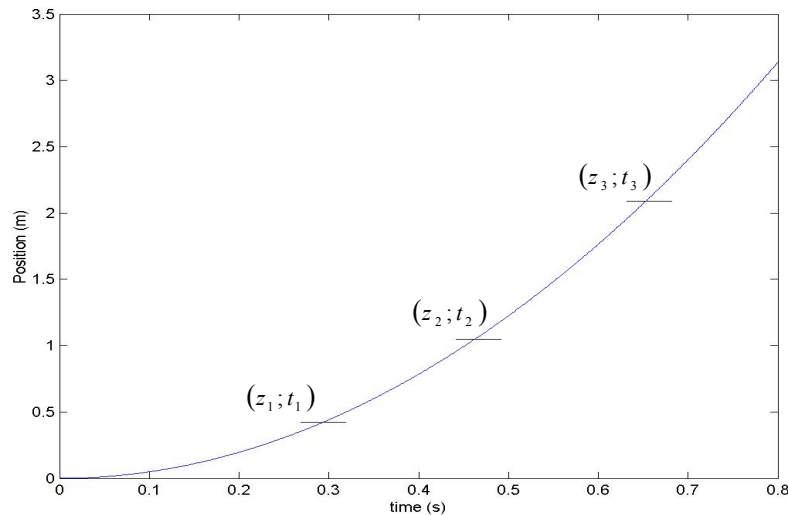


Figure 3-5: Representation of the positions of a free falling body as a function of time.

From (3.3) it is clear that in order to determine g with this method it is necessary to have an instrument capable of measuring simultaneously both the time and the distance with great accuracy.

3.3.2.2 The measurement of time and distances

The position of the free-falling body is measured by means of a Michelson's interferometer of which one arm is fix and the second is able to move vertically. A semi-transparent mirror splits the laser beam, with a wavelength λ , in a reference beam and in a measurement beam. These beams are reflected by the prism parallelly to the incident beams and then recombined in the splitter, creating the desired interferences. M.R. Zumberg describes the basic concept (M.R. Zumberg et al. 1982). A translation of the falling body of $\lambda/2$ produces minima and maxima of the intensity of interference fringes.

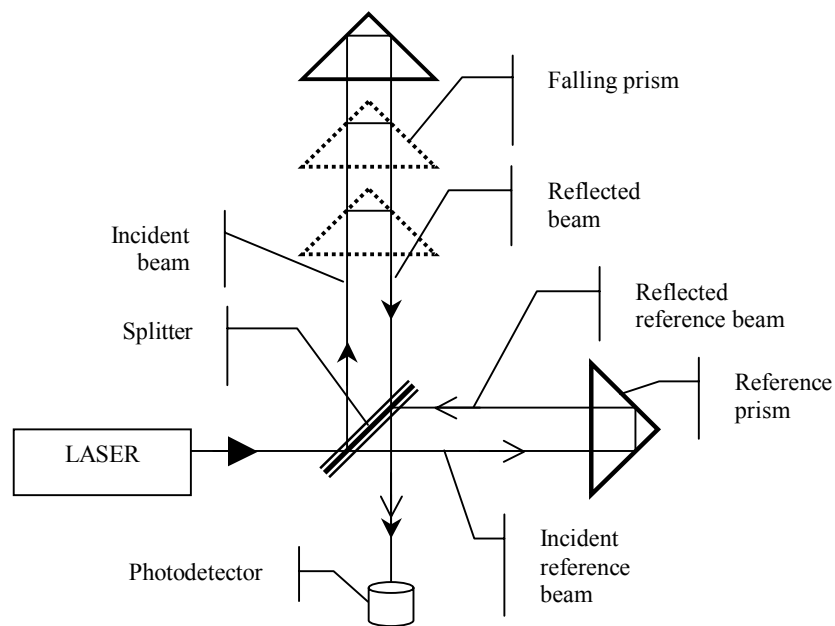


Figure 3-6: Block diagram of a *Michelson's* interferometer used in the free-fall method. The laser light is split into two beams, which are reflected by the falling prism and by the reference prism respectively. The recombined beam is then transformed in an electrical signal by the photo-detector. This signal is amplitude-modulated by the movement of the falling prism.

The optical signal obtained is converted into an electrical signal of which each zero with positive slope is transformed in a pulse. By counting N pulses one can compute the length of the travel path by:

$$\Delta z = N \cdot \frac{\lambda}{2}$$

The determination of the times corresponding to each Δz is done by measuring the time interval between the pulses (See Figure 3-7)

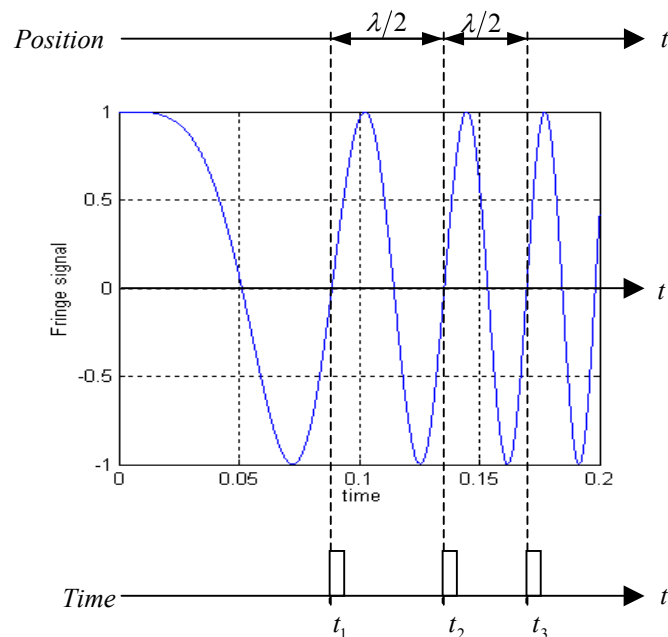


Figure 3-7: Principle of the simultaneous measurements of time and distance. The time interval between the pulses corresponds to the time that was needed to modify the relative distance between the prisms by $\lambda/2$. In other words, if the reference prism stays absolutely fix, the time interval corresponds to the time the falling prism has used to cover a distance of $\lambda/2$.

The electrical signal obtained at the output of the photo-detector can be modeled by the following equations (T. Niebauer, 1989):

$$\begin{aligned}
 U(t) &= u_0 \cdot \cos(2kz(t)) \\
 \text{where:} \\
 k &= \frac{2\pi}{\lambda} \\
 z &= z_0 + v_0 \tilde{t} + \frac{1}{2} g \tilde{t}^2 + \frac{1}{6} \gamma v_0 \tilde{t}^3 + \frac{1}{24} \gamma g \tilde{t}^4 \\
 \tilde{t} &= t - \frac{z - z_0}{c}
 \end{aligned}
 \tag{3.4}$$

With:

- $U(t)$: Measured voltage as a function of time.
- k : Wave number
- λ : Wavelength
- g : Gravity
- v_0, z_0 : Initial values of velocity and position of the falling prism.
- γ : Vertical gravity gradient (Free air gradient: 3.086 [$\mu\text{Gal}/\text{cm}$])
- c : Speed of light

Equation (3.4) describes the electrical signal obtained during a free-fall in a homogeneous gravity field along the trajectory without any external perturbations. In a real measurement case these conditions are not fulfilled, and it is, therefore, judicious to introduce a supplementary term in equations (3.4) accounting for the perturbations to which the gravimeter is submitted.

$$\begin{aligned}
 U(t) &= u_0 \cdot \cos(2kz(t)) \\
 \text{where:} \\
 k &= \frac{2\pi}{\lambda} \\
 z &= z_0 + v_0 \tilde{t} + \frac{1}{2} g \tilde{t}^2 + \frac{1}{6} \gamma_0 \tilde{t}^3 + \frac{1}{24} \gamma g \tilde{t}^4 + P(\tilde{t}) \\
 \tilde{t} &= t - \frac{z - z_0}{c}
 \end{aligned} \tag{3.5}$$

Where:

$P(t)$: Sum of the perturbations acting on the gravimeter

In our case, these perturbations are the non-gravitational accelerations described under chapter 2.2.5.

3.3.3 The FG5-L gravimeter

The gravimeter used in the frame of the AAG project is a FG5 type L built by Micro-g Solutions Inc, Erie Colorado, using the principle described in chapter 3.3.2 (See Figure 3-8).



Figure 3-8: Absolute Gravimeter FG5-L with its electronic command and its laser. The PC (1) is driving the whole system, the electronic rack (2) that contains the GT650 time analyzer, the AD-converter used to sample the Lennartz output signal, and the command electronic used to configure the dropping-chamber (4). In front of the rack is the laser (3) that is connected to the interferometer base (5) by an optical fiber (6). The dropping-chamber (4) is decoupled from the interferometer base (5) by the tripod (7).

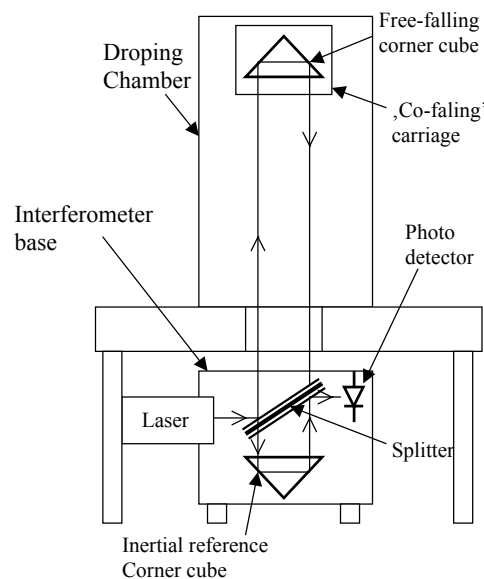


Figure 3-9: Block diagram of the gravimeter FG5-L. The diagram depicts the principal components of the interferometer. The dropping-chamber contains the free-falling corner cube and the co-falling carriage used to shield the falling prism from electromagnetic perturbations. The interferometer-base contains the reference corner cube, the splitter and the photo-detector.

The gravimeter FG5-L is formed of two principal parts: The falling chamber and the interferometer.

The falling chamber consists of the falling prism, a drag-free chamber protecting the prism against the effect of the residual air molecules and the mechanism necessary to carry the prism from its lower position to its upper position. The interferometer is made of the reference

arm, the splitter, the photo-diode and the electronics transforming the optical signal into electrical pulses.

The gravimeter FG5-L is in fact a small version of a FG5 with the significant difference that it is not equipped with the ‘Super-Spring’ to which the reference mirror is fixed. From their similarities the sources of errors of both gravimeters (FG5-L and FG5) can be considered as equal. These sources of error have been analyzed in detail by *Niebauer et al.* (1995) who have shown that the sum of all uncertainties is of the order of 1.1 *microGal*. However, this estimation has been performed under laboratory conditions, which can be considered experimentally almost perfect.

The vibrations, which are modifying the position of the reference prism and, therefore, modify the measured value of g , are of two kinds: Those that are produced by the system itself and those that are of environmental origin. The first ones are produced by the driving mechanism of the drag-free chamber and can be partially eliminated by decoupling physically the interferometer from the dropping chamber.

The vibrations of environmental origin can be compensated for in two different manners. Either by a mechanical absorption system, like the Super-Spring used in the FG5 (*Rinker*, 1983), or by a numerical processing of the data (*Brown*, 2000). It is the last method that the FG5-L uses. The system is equipped with a Lennartz LE-3D/5s seismometer. The output signal from the seismometer is digitized with a 16 bits A/D card and recorded for each drop.

3.3.3.1 The determination of g

The FG5-L system uses an external sensor for measuring and recording the accelerations of environmental origins. These accelerations are then used for correcting the raw measurements by numerically compensating the movement of the reference mirror. For every detected fringe equation (3.5) can be written in a digital form taking into account the measurement of the external sensor ‘ s ’.

$$z_i = z_0 + v_0 \tilde{t}_i + \frac{1}{2} g \tilde{t}_i^2 + \frac{1}{6} \gamma v_0 \tilde{t}_i^3 + \frac{1}{24} \gamma g \tilde{t}_i^4 + \alpha_s f_s(\tilde{t}_i) \quad (3.6)$$

Where f_s corresponds to the function of the signal measured by the sensor ‘ s ’ and α_s to the scaling factor.

The principal difficulty is to synchronize the external measurement with the one of the FG5-L and to determine the scaling factor. In fact in order to obtain a resolution on the order of one [microGal] the time difference between two fringes has to be accurate to about one *nanosecond*, and the position of the falling prism on the order of one *nanometer* (*T. M. Niebauer et al.* 1995).

The seismometer used by the FG5-L is a Lennartz seismometer from which the signal is digitized with a Daqboard2000 16 bits A/D card. The Lennartz-Daqboard system can be configured to measure maximum velocities between 0.78 *mm/s* and 50 *mm/s* with a respective resolution from 11 *nm/s* and 770 *nm/s*. We will see in chapter 0 that the measured velocities in the aircraft are larger than 70 *mm/s* in the low frequencies. The synchronization between the signal measured by the external sensor and the one from the FG5-L is done mathematically by correlation and the scale factor is estimated by least squares adjustment as well as x_0 , v_0 and g .

3.3.3.2 Principal characteristics of the FG5-L

Table 3-1 gives the principal specification of the absolute FG5-L gravimeter.

Instrument Specification	
Accuracy	50 microGal
Repetability	10 microGal

Table 3-1: Principal specification of the FG5-L

3.3.4 The EpiSensor accelerometer

To measure the non-gravitational accelerations, we equipped the system with a three-axial accelerometer. The EpiSensor consists of three orthogonally mounted force balanced accelerometers (FBAs), X-Axis, Y-Axis, Z-Axis, inside a sensor casing. Figure 3-10 below shows a simplified block diagram of the major components of each of the FBAs.

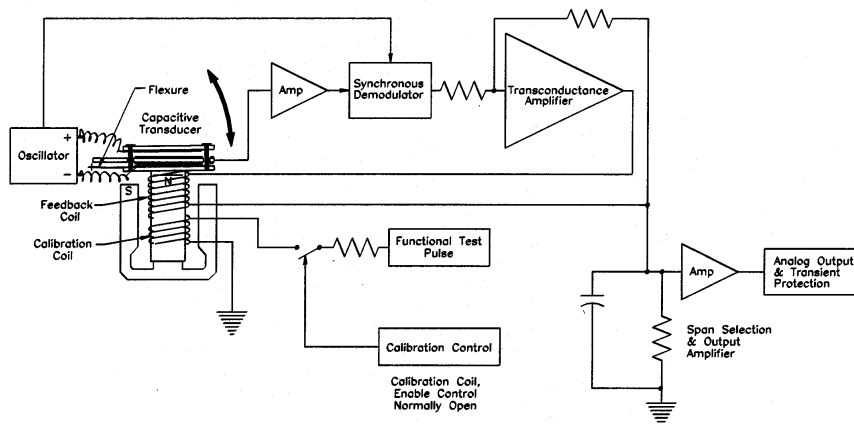


Figure 3-10: Simplified block diagram of an accelerometer. On the left side is the oscillator that applies a signal to the two moving capacitor plates. With the fixed central plate, the moving ones are forming a capacitor bridge. Voltage modifications induced by movements are amplified and filtered to generate a current. This current is then used to create a magnetic restoring force that brings the system back to its null position.

3.3.4.1 Working Principle

The oscillator applies an AC signal of opposite polarity to the two moving capacitor plates. When the accelerometer is at rest, the two plates are in symmetrical position above and below the fixed central plate and the voltage of the capacitor bridge is constant. An acceleration causes the coil and capacitive sensor plates, which are a single assembly mounted on mechanical flexures, to move with respect to the fixed central plate of the capacitive transducer. This displacement generates a variation of the voltage on the capacitor bridge. The signal is then amplified and passed to the demodulator where it is synchronously demodulated and filtered, creating an error term in the feedback amplifier. The feedback loop compensates for this error signal by passing current through the coil to create a magnetic restoring force to “balance” the capacitor plate back to their original null position.

The current traveling through the coil is thus directly proportional to the applied acceleration.

3.3.4.2 EpiSensor Specifications

Table 3-2 shows the essential characteristics of the EpiSensor

Type	Triaxial force balanced accelerometer
Dynamic range	155 dB
Bandwidth	DC to 200 Hz
Full-scale range	User-selectable at $\pm 0.25g$, $\pm 0.5g$, $\pm 1g$, $\pm 2g$ or $\pm 4g$

Table 3-2: Specifications of the Episensor three axial accelerometer

Theoretically, if the full dynamics of 155 *dB* is used, the resolution reaches approximately 8 *microGal* at a full scale of $\pm 0.25 g$. In our application, the full scale is set at $\pm 1 g$ and a 24 bits digitizer is used to digitize the output signal from the sensor. In this configuration the sensor can theoretically measure external disturbing acceleration with a resolution of about 0.12 *mGal*.

3.3.5 Inertial Navigation System (LN 200)

For determining the vertical non-gravitational accelerations, it is indispensable to know the attitude of the platform to which the measuring instruments are attached. To determine the attitude there are two possibilities. One can determine it with the GPS-antennas array fixed to the aircraft (Favey, 2001) or the system can be equipped with an inertial navigation system (INS). The Northrup Grumman LN-200 INS that we used, is an inertial system using fiber optic gyros (FOGs) and silicon accelerometers (SiAc's) for measurements of vehicle angular rate and linear acceleration.

Silicon accelerometers:

Over the last several years, extensive efforts have been devoted to the development of micromachined accelerometers with high sensitivity and large dynamic range using both, bulk-silicon and surface micromachining techniques. Many of these devices employ a capacitive sense mechanism where by the deflection of the inertial mass produce a change in the inter-electrode air gap of the capacitor. Thus, a change in the capacitance provides a measure of the acceleration.

A capacitive z-axis accelerometer is illustrated in Figure 3-11 (Selvakumar et al., 1996). The support beams are twisted by a torque produced by an acceleration acting on the offset center mass. This twisting is manifested as a change in the overlap area of the interdigitated fingers attached to the inertial mass.

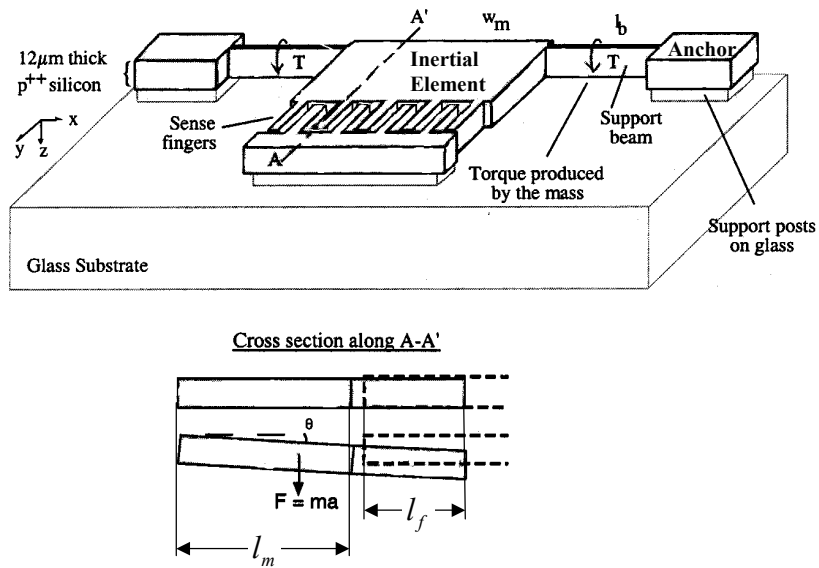


Figure 3-11: A z-axis capacitive torsional accelerometer. The Inertial Element can move around the axis defined by the support beam. The movements of the Inertial Element are modifying the overlap area of the interdigitated fingers. This modification will change the value of the capacitance proportionally to the applied acceleration.

An acceleration acting on the offset center of mass of the structure produces a torque on the suspension beam, thereby twisting them. The twisting angle θ , assuming a rigid mass plate, is given by

$$\theta = \frac{Ml_m l_b}{4\alpha G t w_b^3} a_z \quad (3.7)$$

With :

l_b, w_b : length and width of the beam;

l_m, w_m : length and width of the mass;

t : structur thickness;

G : modulus of rigidity;

M : mass;

a_z : z - axis acceleration,

α : correction factor (cross - section aspect)

The rotation of the mass and the attached sense fingers arrays from the rest position result in a reduction of the overlap area and hence the capacitance between the sense fingers. The capacitance change ΔC for n finger sense of length l_f , with an air gap p , and relative permittivity ϵ_r , is then given by:

$$\Delta C = \frac{n\epsilon_r l_f}{p} (2l_m + l_f) \theta \quad (3.8)$$

3.3.5.1 Fiber-Optic Gyro

Fiber-Optic gyros are solid-state devices, without moving parts, which require low power. They are very rugged and reliable, and thus are suitable to harsh dynamic environments. Analogous to GPS satellite ranging, the interferometric FOG (I-FOG) measures the difference in phase of two light beams traveling through a loop of optical fiber, where, ideally, the phase difference is due to rotation of the plane of the loop according to the Sagnac effect (*Torge, 1989*).

Figure 3-12 shows schematically the working principle of this kind of gyros. The light from a monochromatic source passes through a coupler to a polarizer and is split into two beams that propagate in opposite directions through the optical fiber loop. Upon exiting the loop, the light waves are recombined and the resulting wave is sent to a photodetector that generates an electrical voltage proportional to the optical power of the wave.

Due to the Sagnac effect, the rotation of the loop about an axis perpendicular to the plane of the loop causes a light beam to travel an extra distance ΔL . For two propagating beams the net relative distance is the difference

$$\Delta L - \Delta l = \frac{4\omega}{c} A \quad (3.9)$$

Where :

ω : angular rate

c : light speed

A : area swept out by the light

The Sagnac effect being independent of the shape of the optical fiber this one is coiled to increase the enclosed area, A , of the loop, thus increasing the phase difference for a given rotation and hence the sensitivity of the gyro. Let n be the number of optical fiber winding of the coil. The effective total area covered by the beam is

$$A = n\pi \frac{d^2}{4} = \frac{1}{4} Ld, \quad (3.10)$$

where d is the diameter of the coil and L is the total length of the fiber. Substituting (3.10) into (3.9) and converting to phase difference, we find the phase change, in radians, due to rotation:

$$\Delta\phi = \frac{\Delta L - \Delta l}{\lambda} = \frac{Ld}{\lambda c} \omega. \quad (3.11)$$

Where $\Delta\phi$ is in units of cycle.

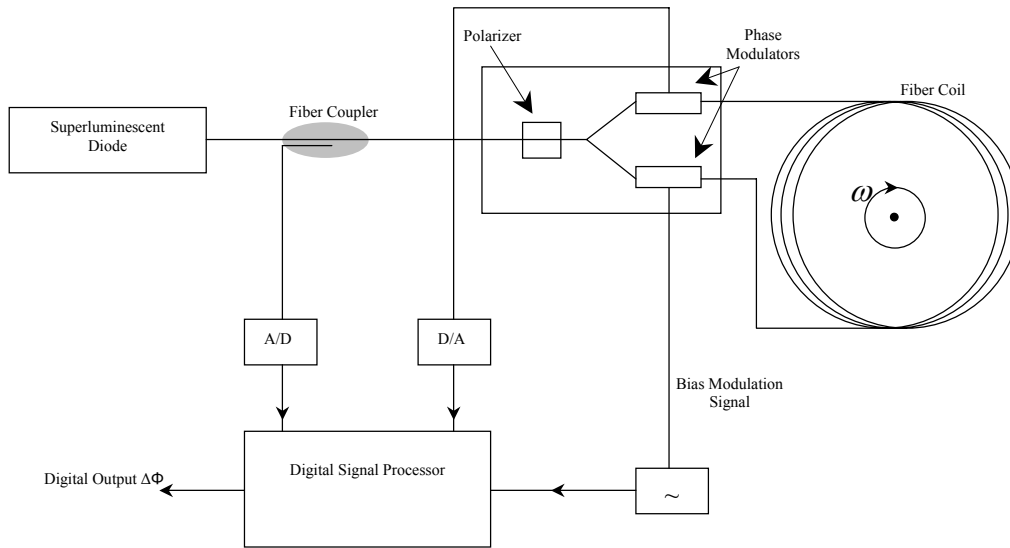


Figure 3-12: Schematic of the interferometric fiber-optic gyro. The optical beam is split into two signals that are propagating in the fiber coil in opposite sense. The recombined signal is modulated by the phase difference $\Delta\phi$ between the two signals that is proportional to the angular rate ω

3.3.5.2 LN-200 IMU Specifications

The following tables, Table 3-3, Table 3-4 and Table 3-5 give an overview of the principal characteristics of the Ln-200 IMU.

Performance-Gyro:

Type	Gyro
Bias Repeatability:	1 °/hr to 10 °/hr, 1 sigma
Scale Factor:	100 to 500 ppm, 1 sigma

Table 3-3: Gyro performances

Performance-Accelerometer:

Type	Accelerometer
Bias Repeatability:	300 microg 3 milli-g, 1 sigma
Scale Factor:	100 to 5000 ppm, 1 sigma

Table 3-4: Accelerometer performances

LM-200 Operating Range:

Type	LM-200
Angular Rate:	Up to ± 11.459 °/sec
Angular Acceleration:	± 100000 °/sec/sec
Acceleration:	± 40 g

Table 3-5: LM-200 Operating Range

The resolution of the accelerometer of the LN-200 at 400 Hz sampling rate is 2400 mGal and the resolution of the FOG for the same sampling rate is 0.002 degrees/s. It is clear that the resolution of the accelerometer is not good enough for directly compensating the measurement of the FG5-L. The scale factor of the LN-200 accelerometer was estimated for each measurement by least squares fit after an adequate synchronization has been carried out between both signals.

3.3.6 The Instrument Platform

As already mentioned at the beginning of this chapter, the function of the platform is to damp the perturbing environmental non-gravitational accelerations. A complete chapter is later dedicated to this problem (see chapter 0).

3.3.7 Conclusion

With equation (3.5) a complete physical model of the FG5-L gravimeter in airborne conditions can be described. To be able to determine g , we have to know the scaling factors, which are connecting the non-gravitational acceleration with the physical model. These factors will be estimated with the help of the data acquired by the external sensors, IMU, GPS and Episensor, during the data processing.

4 The damping platforms

4.1 Introduction

As mentioned in the previous chapters, in airborne absolute gravimetry the vibrations of different sources act as disturbing accelerations, and, therefore, modify the results of the measured g .

The sources of these accelerations are first, the vibrations induced by the engine and the movement from the aircraft, and second by the measuring system itself.

In order to be able to determine the sum of the accelerations due to the vertical movements of the aircraft and the gravity with a reasonable accuracy, it is of highest importance to remove the effects of the vibrations either by a mechanical coupling system or by appropriate mathematical algorithms during the processing of the data.

4.2 Analysis of the vibrations of the aircraft.

The aircraft used for the AAG project was a Twin-Otter DeHavilland belonging to the Swiss Federal Office of Topography (now: SWISSTOPO). The vibration's spectrum of the aircraft was measured during a dedicated flight on August 11, 2001 carried out between Zurich and Bern at the nominal altitude of 1800 m a.s.l at a speed of 80 m/s , corresponding to that planned for the experiment. The measuring system was a MR2002 from Ziegler Consultants, mounted on the top of an aluminum plate of 10 mm thickness directly fastened to the seat's rail. The data were acquired during time windows of around 20 seconds continuously repeated during the whole flight (H. Baumann, 2002). Figure 4-1 shows the mean value of the spectra measured during the test flight.

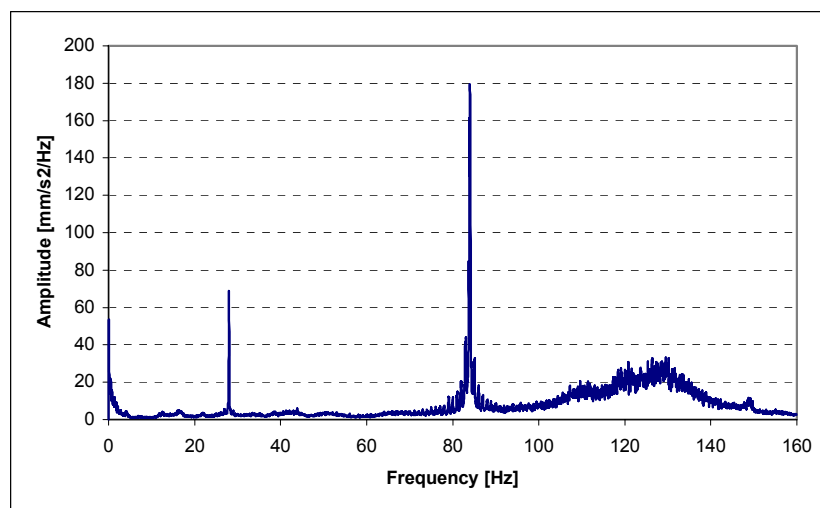


Figure 4-1: Amplitude spectrum of the vibrations measured in the Twin-Otter HD-LID

One can see in Figure 4-1 three well-defined peaks and a broader waveband at 1-3 Hz , 28 Hz , 84 Hz respectively and the last one between 100 and 140 Hz . The maximum amplitude of the vibrations is at 84 Hz with amplitude of around 18'000 $mGals$. The second peak in amplitude is of 28 Hz with 7'000 $mGals$.

A more detailed analysis is shown in Figure 4-2 and Figure 4-3.

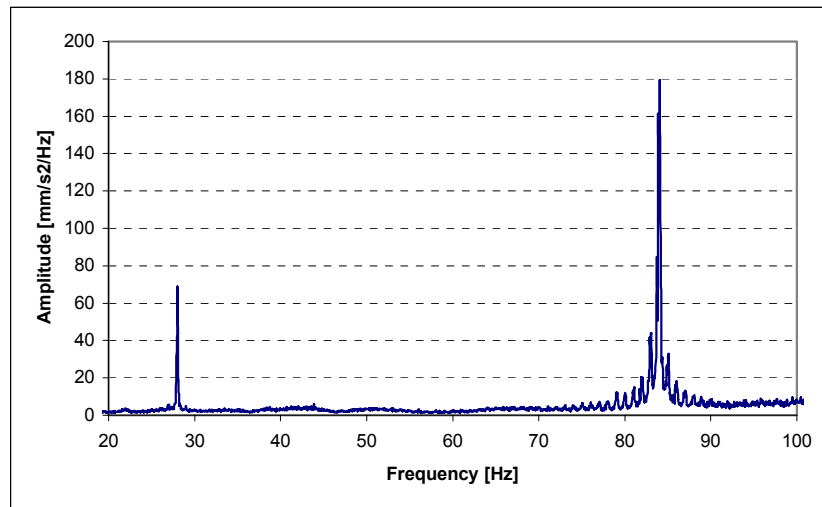


Figure 4-2: Amplitude spectrum of the vibrations measured in the Twin-Otter HD-LID, for the frequency range of 0-100 Hz.

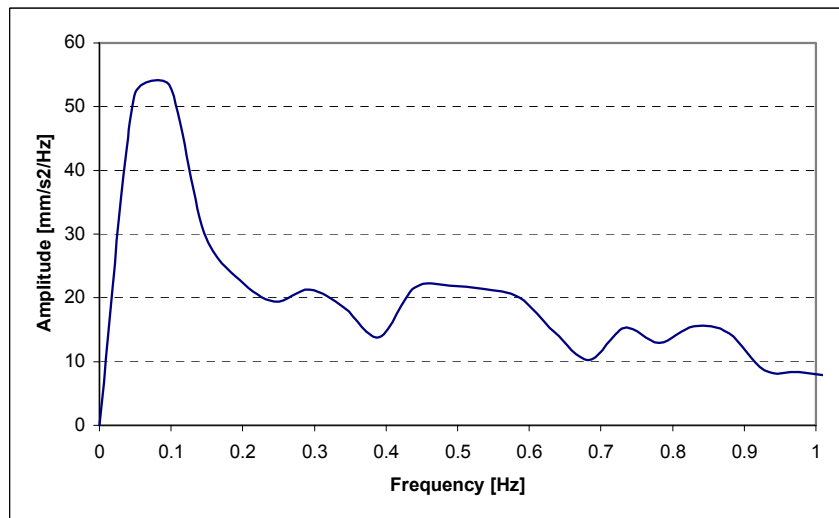


Figure 4-3: Amplitude spectrum of the vibrations measured in the Twin-Otter HD-LID, for the frequency ranges 0-1 Hz.

The first burst of vibrations at 28 Hz is due to the angular velocity of the turbines, which is of 1700 rotations/min. The three blades of the propellers passing in the front of the wing produce the second burst at 84 Hz. Each pass produces a shock wave against the wing that is transmitted to the structure of the aircraft and further to the seat's rail in the cabin.

The proper movement of the aircraft produces the vibrations of low frequencies. Because their frequencies are below 1 Hz these induced accelerations can be removed by modeling the movements of the aircraft with GPS data. The frequencies that are located between 100 Hz and 140 Hz are due to resonance frequencies of the cabin and of the metal sheets.

4.3 Mechanical systems of absorption

4.3.1 Introduction

Three different kind of systems were studied as mechanical systems of absorption.

- Active table MOD1-L
- Multi-layer table
- Hanging table

The experiments were performed following the same scheme as shown in Figure 4-4. The test system was composed mainly of three parts: The measuring part, the excitation part and finally the system to be tested.

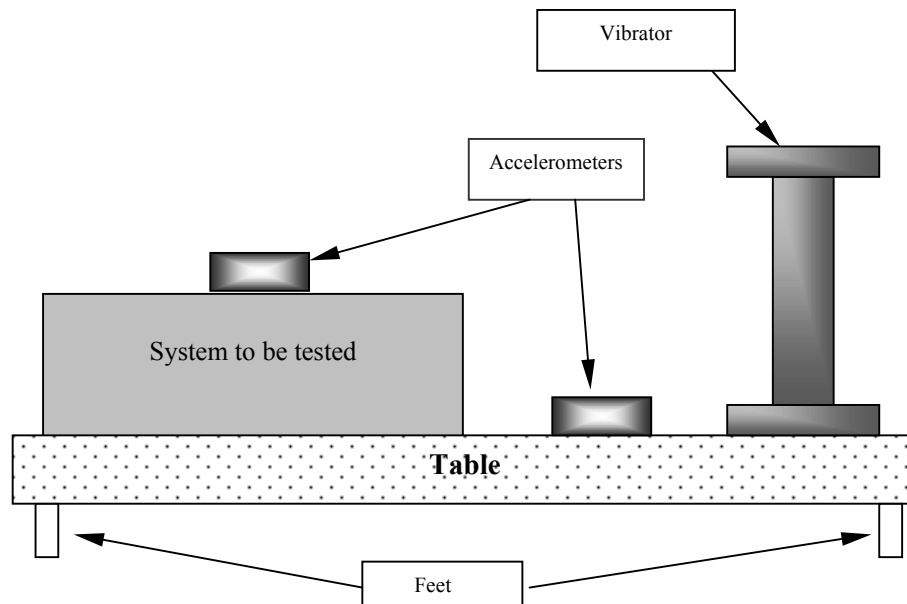


Figure 4-4: Schematic view of the whole test system. The vibrator is shaking the table in the desired frequency. One accelerometer is fixed on the table and the other on the damping system under test. The ratio between the measured amplitudes gives then the searched amplitude spectrum.

The excitation part is formed of a vibrator and a table made of honeycomb aluminium with four cylindrical feet. The vibrator consists of a mass moving vertically at programmed frequencies allowing swapping the spectrum from 0.1 Hz to 150 Hz with different amplitudes. The measuring part consists of two accelerometers MR2002 from Ziegler Consultant, one located directly on the table, the other one placed on the system to be tested. The data are collected by an analog digital system and written on the hard disk of a notebook computer. A dedicated program allows to compute the amplitude spectrum for either the entire frequency range or for only chosen frequency windows. The transfer function of the system is then to be calculated at each frequency as the ratio of the spectrum amplitude measured on the table to that measured on the tested system (*H. Baumann, 2002*).

4.3.2 The active table MOD1-L from Halcyonics

The active table is a commercial system designed to stabilize optical tables. The system is an interactive damping table, which that adjusts its filter coefficients to the environmental noise. As soon as the system detects a significant variation of the external condition it re-adapts the coefficients. Unfortunately, it was not possible to get detailed information about its working principle. Therefore it is considered as a black box filtering the vibrations coming from the ground. For the determination of its transfer function we used the system depicted by Figure 4-4. The two following figures (Figure 4-5, Figure 4-6) show the determination of the transfer function at 10 Hz.

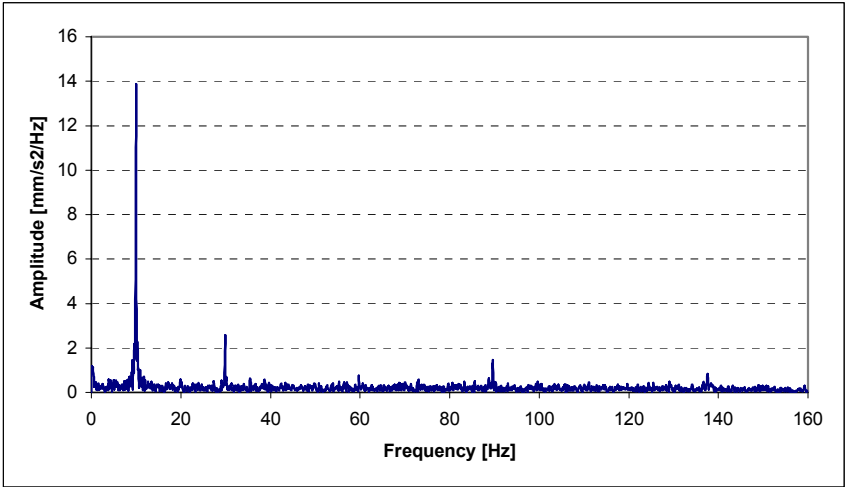


Figure 4-5: Spectrum measured on the excitation's table for a frequency of excitation of 10 Hz.

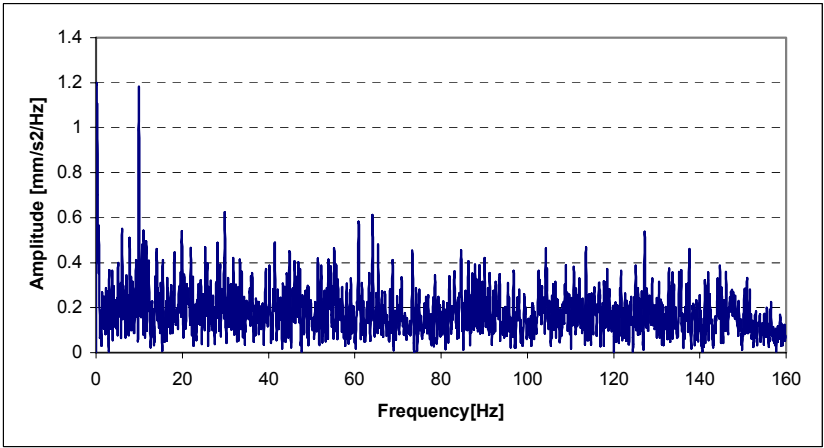


Figure 4-6: Spectrum measured on the top of the Halcyonic table during an excitation of 10 Hz.

By comparing the two amplitudes at 10 *Hz* we can determine an attenuation factor of 10. The same experiment carried out for frequencies between 1 *Hz* and 80 *Hz* allowed us to compute the entire transfer function of this table. The result is shown in Figure 4-7.

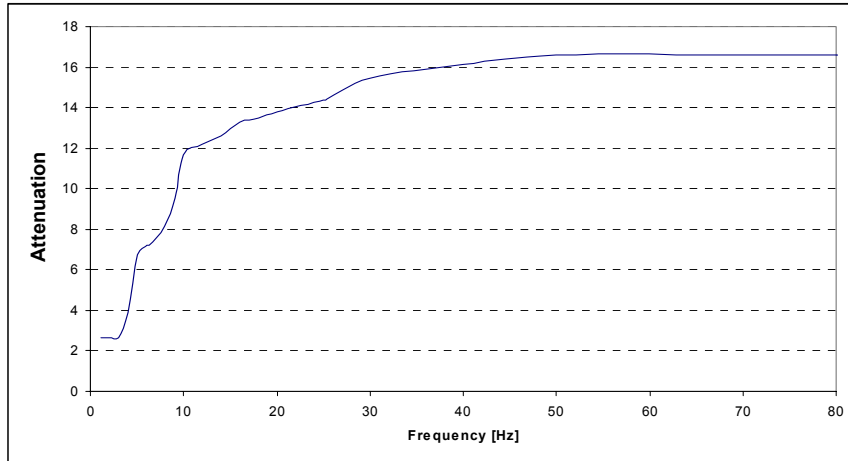


Figure 4-7: Attenuation function of the Halcyonic table for frequencies between 1 *Hz* and 80 *Hz*.

The application of the transfer function of the Halcyonic table to the spectrum of the vibrations measured in the aircraft during the test flight gives a rough estimation of the behavior of this kind of table in flight conditions. The result of this estimate is shown in Figure 4-8. The peak at 28 *Hz* is reduced to only 500 *mGal*, the peak at 84 *Hz* is reduced to 1100 *mGal*. The amplitudes in the frequencies between 100 *Hz* and 150 *Hz* are not significantly reduced and reach 190 *mGal* too. Because we are looking for an accuracy of about 2-10 *miliGal*, these amplitudes are still almost 500 times too high.

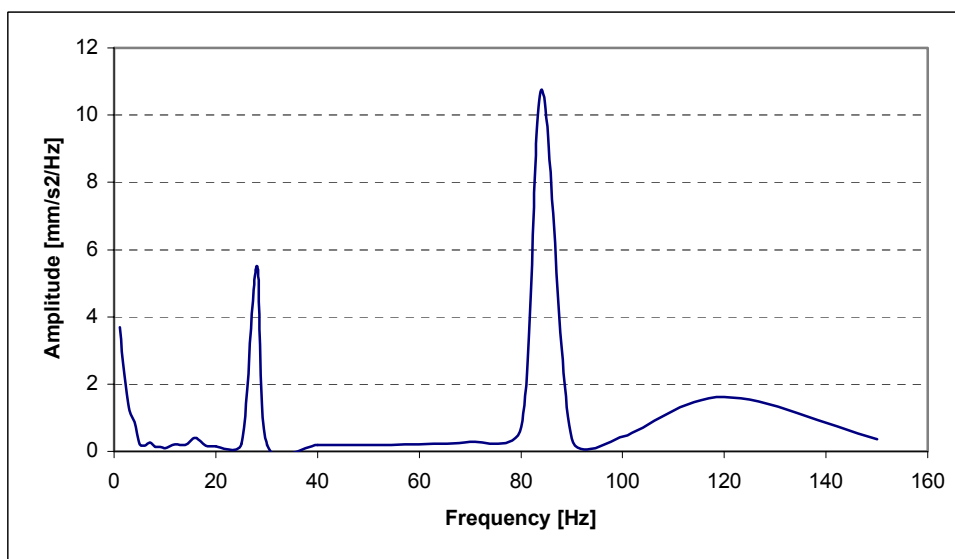


Figure 4-8: Theoretical vibration's spectrum of the aircraft after passing through the Halcyonic table.

4.4 The multi-layer table

4.4.1 Introduction

The basic idea is to construct an absorbing system by alternating layers of elastic material with layers of heavy and rigid material. Figure 4-9 shows a schematic cross section of such a table.

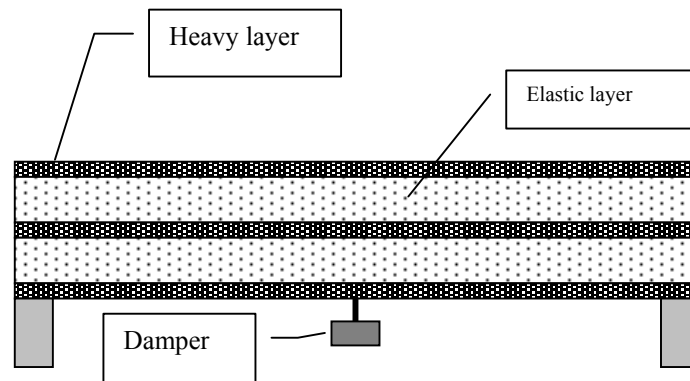


Figure 4-9: Schematic cross section of a multi-layers table

The damper placed below the table is in fact connected to the upper layer of the table and it is supposed to reduce the amplitude of the natural frequency of the table by moving in the opposite direction.

The behavior of the system can be modeled by n oscillating masses coupled in serial. The simplified transfer function H of such a system is described by the equation (4.1) whereby the attenuation factor from each oscillator is neglected.

$$|H(\omega)| = \frac{1}{1 - \left(\frac{\omega}{\Omega}\right)^2} \cdot \left[\frac{1}{2 - \left(\frac{\omega}{\Omega}\right)^2} \right]^{n-1} \quad (4.1)$$

Where: Ω = $(k/m)^{1/2}$ natural frequency
 k = Spring's constant
 M = Masse
 n = Number of layers
 ω = Applied frequency

4.4.2 The experimental mounting

The experimental table was made of a honeycomb plate supported by four cylindrical feet of aluminum with a height of 60 cm. The honeycomb plate supported twice a layer of 10 cm of synthetic foam covered by a steel plate with a weight of 40 kg. The whole system has a hole in the middle of its surface into which the dynamic damper hangs. This damper is formed of a rubber cord with a hanging mass of lead of 5 kg (Figure 4-10).



Figure 4-10: The experimental two layer absorbing table with its dynamic damper

In order to obtain the best possible behavior of the table different kind of synthetic foams were analyzed. The characteristics of these foams are summarized in Table 4-1.

Kind of foam:	Density	Compression load defelection	Elongation at break	Tensile strength	Bun height net
	[kg/m ³]	[kPa]	[%]	[kPa]	[mm]
SHT100120	80	11	130	220	630
SRT110190	100	12	130	200	440
SET80100	110	19	130	300	460

Table 4-1: Summary of the characteristic of the studied foams.

In fact the most important factor is the natural frequency of each layer which depends on the spring's constant k of the material.

This constant is given by
$$k = \frac{S \cdot E}{h}$$

With E = Young's modulus, S = Surface of the layer and h = thickness of the layer.

For a given material it is possible to change the natural frequency of a layer through a modification of the factor k . This can be obtained by modifying the ratio S/h . The working area being given and the thickness of the foam depending on the manufacturer it is necessary to take foam with a small Young's modulus and then to calculate the mass necessary to obtain the desired natural frequency. Our choice was then concentrated to the foam SHT 100120 which has a Young's modulus of 11 kPa and a thickness of 10 cm. In order to obtain a natural frequency of around 10 Hz each layer has to be loaded by a mass of 30 kg.

4.4.3 Determination of the transfer function of the multi-layer table

In order to obtain a first approximation of the behavior of this table we measured its impulse response. This allows the computation of its natural frequency and of its attenuation's factor.

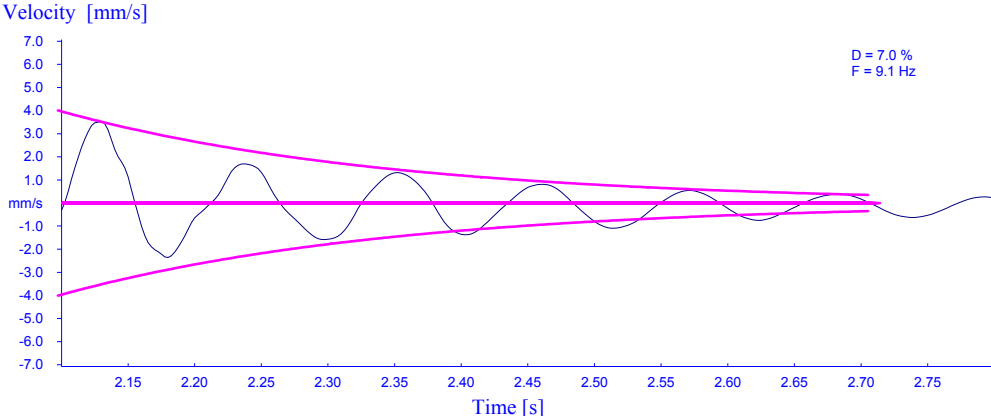


Figure 4-11: Impulse response of the experimental mounting shown in Figure 4-10

The natural frequency of this table is 9.1 Hz and its attenuation's factor is 7 %. Both values are a little smaller than expected but are in the tolerable range.

A more complete study of the table behavior has been obtained by systematically measuring the input-output ratio at frequencies between 0 Hz and 100 Hz by a step of 2 Hz using the measurement system depicted in Figure 4-9. The transfer function obtained is shown in Figure 4-12.

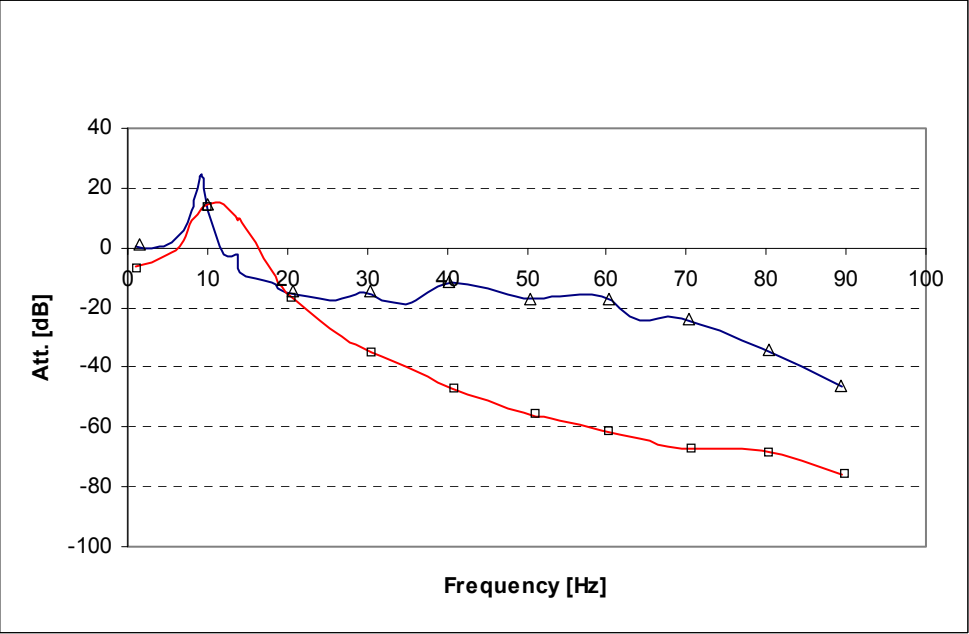


Figure 4-12: Theoretical (square) and experimental (triangles) transfer functions of the multi-layer table.

These results show a strong difference between the theoretical and the experimental transfer functions. Particularly the peak at 10 Hz is of significant importance. The relatively low absorption between 20 Hz and 100 Hz can be attributed to the attenuation factor of the foam itself, which is not taken into account in the simplified model (4.1).

4.4.4 Application to the vibrations of the aircraft

By applying the experimental transfer function obtained in 0 to the experimental spectrum of the vibrations of the aircraft it is possible to see if the multi-layer table is well-suited for the proposed measuring system. In fact the results shown in Figure 4-13 are quite disappointing because it is impossible to remove the peaks at 10 and 28 Hz even if the attenuation above 40 Hz is satisfactory.

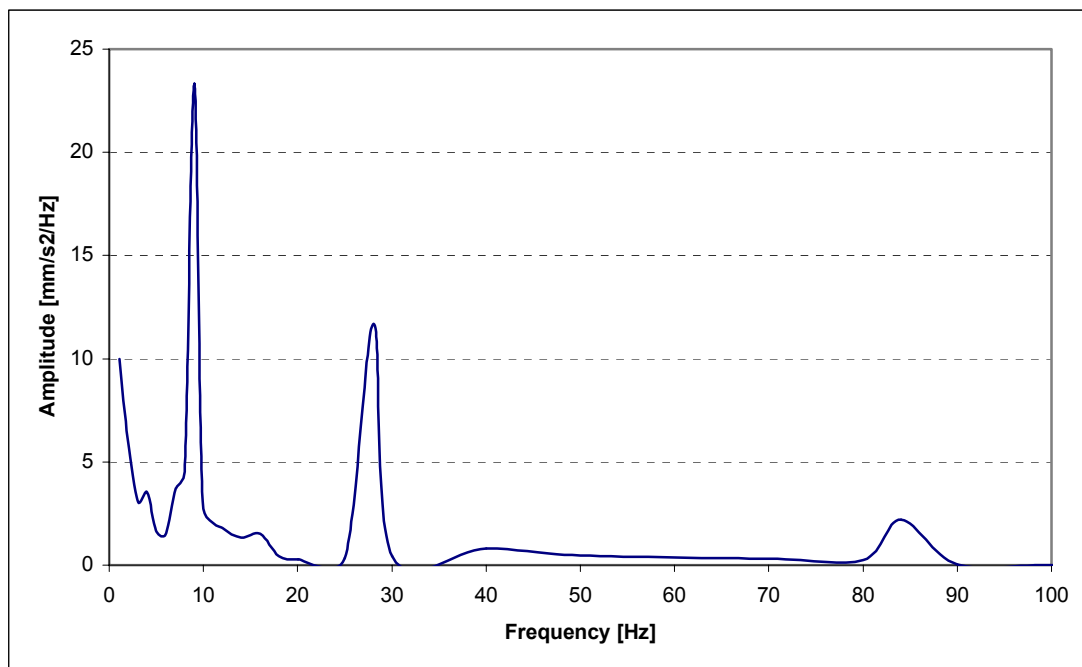


Figure 4-13: Expected transfer function of the system aircraft-multi layer table.

In conclusion a multi-layer table, as conceived, can probably be improved in the laboratory by increasing the number of layers and the weights applied to these layers. However this could introduce instabilities and great sensitivity to horizontal vibrations. Because the weight is a very important factor in airborne application we decided to not pursue any improvement of such a system.

4.5 The hanging table

4.5.1 Introduction

This system, schematically shown in Figure 4-14, is formed of a cage to which a table is suspended inside (for the measuring instruments). The suspension is made of rubber cords. Below the table a damping system is attached whose purpose is to damp excessively large oscillations of low frequencies.

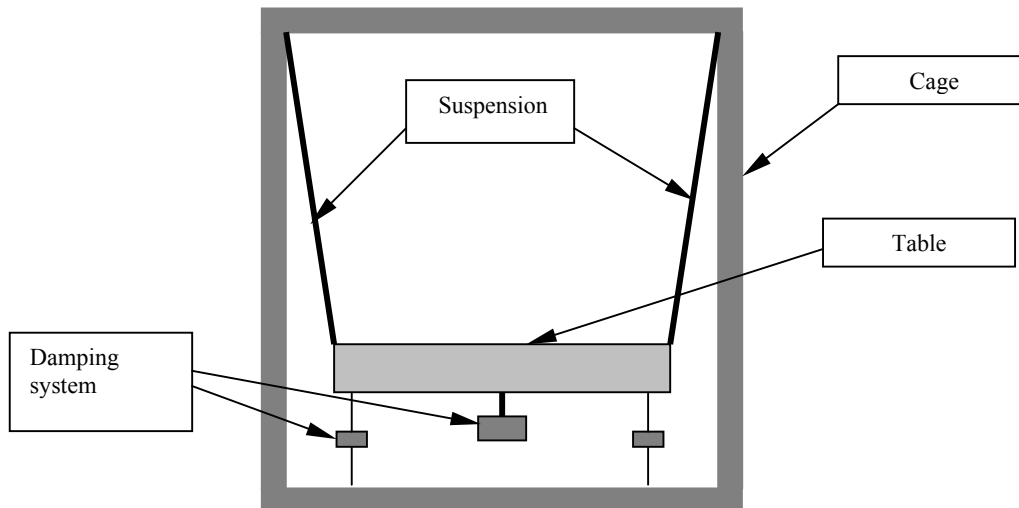


Figure 4-14: Schematic view of a hanging table

This prototype is directly inspired from a small hanging table developed by micro-g Inc which is shown in Figure 4-15. The small table is entirely made of aluminum and is formed of one principal static cage and one mobile cage. Both have a cylindrical shape. The mobile cage is suspended inside the principal cage by a system of lever and spring like a vertical seismometer. The point of attachment is located in the center of the lower plate forming the mobile cage. In order to ensure a perfect vertical movement without rotation the mobile cage is constrained by five horizontal arms. Two pair of magnets, mounted pole against pole on one pillar of the principal cage serves to damp the movement of the table when it enters into resonance.



Figure 4-15: Small damping table of micro-g solutions (Height: 50 cm)

The behavior of this table follows the transfer function:

$$|H(\omega)| = \frac{1 + \frac{\beta}{\omega_c^2}}{1 - \frac{\omega^2}{\omega_c^2} + \frac{\beta}{\omega_c^2}}$$

Where ω = pulsation of the input, ω_c = the frequency of the system and β = the damping factor

The aim of the damping factor, is to reduce the oscillation amplitude when the system enters into resonance. But by increasing the damping factor the filtering qualities of the system are also reduced.

4.5.2 The table

The table, shown in Figure 4-16, consists of four parts which are :

1. The principal cage composed of one base plate, three pillars and a top plate. The two plates of circular shape are of honeycomb material (ALUCOR), which has a very high rigidity for a low weight.
2. The hanging table made of the same material as the principal cage, has also a similar shape but with a smaller height to diameter ratio.
3. The guiding system was, in a first time composed of five rigid steal arms linking the hanging table to the principal cage. After many tests, 12 KEVLAR cords replaced them. Six of these cords are fasten to the lower plate of the hanging table and six to the upper plate.
4. The suspension, which is the most delicate part of the system, is made of a double rubber cord. The filter characteristics of the system depend strongly to the quality of the suspension. The suspension has also to be easily changed because of the wearing down of the rubber cords. Another delicate point is the fasten system of the cords. Many systems were tested like end-to-end gluing, bridle-bridle, bridle-cartridge and finally simple bridle.



Figure 4-16: The first prototype of the table of second generation (Height: 180 *cm*)

4.5.3 The determination of the transfer function

The transfer function of the hanging table was determined in the same manner as for the two other tables. The table was placed at the center of a wooden plate and the hanging table charged with a 50 *kg* load. The electro-dynamic vibrator was then placed on a side of the table. Finally the accelerometers were placed on the system: one on the wooden plate, one on the center of the base plate and one in the center of the hanging table. The experimental setup is shown in

Figure 4-17. The ratio of the measured amplitudes of the wooden plate accelerometer and the hanging table at each frequency gives then the transfer function.



Figure 4-17: View of the experimental mounting used for the determination of the transfer function

After a large number of tests and modifications done for optimizing the table behavior the determination of the transfer function of the hanging table was carried out. This function is shown in Figure 4-18.

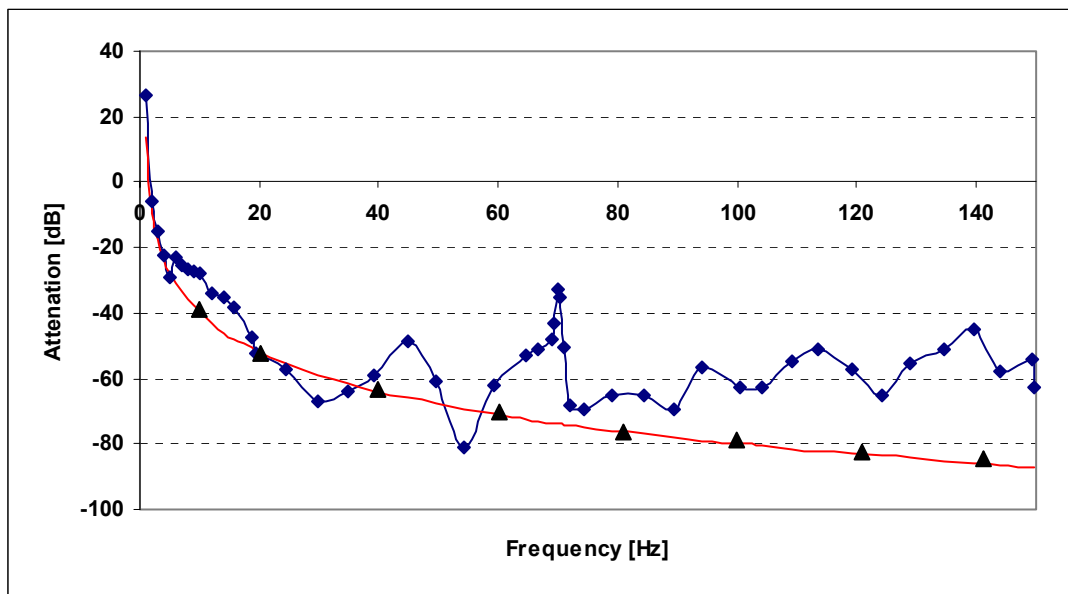


Figure 4-18: Transfer function of the hanging table. ▲: Theoretical transfer function of the hanging-table, ■: Measured transfer function of the hanging table.

The shape of the transfer function obtained by measurements is very similar to the theoretical one. A strong peak is present at 70 Hz. A more detailed study showed that this frequency corresponds to the natural frequency of the sheets of the rubbed cords. We then removed these sheets. Finally some other small modifications were done before the first dynamic test were carried out. These modifications were:

- The increase of the length of the pillars of the hanging table.
- A cut in the upper plate of the hanging table making it as a crown.
- Mounting of a magnetic damper below the hanging table

4.5.4 Application to the vibrations of the aircraft

By applying the experimental transfer function obtained in 4.5.3 to the experimental spectrum of the vibrations of the aircraft we can see if the hanging table is well suited for the proposed measuring system.

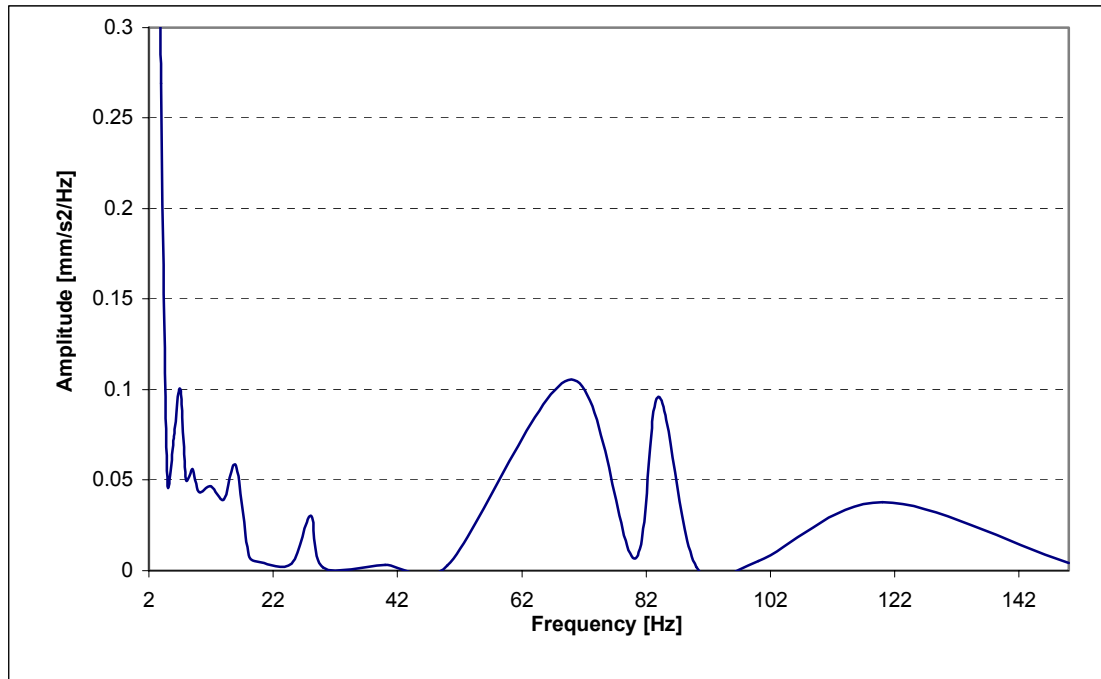


Figure 4-19: Expected transfer function of the system aircraft-hanging table.

As it can be seen, under flight conditions the expected behavior of the hanging table seems to be much better than the behavior of the multi layer or MOD-1 tables. The remaining peaks in the domain between 5 and 150 Hz are lower than 15 *mGal*, which corresponds to the order of accuracy that we are looking for.

4.5.5 The first dynamic test

For the first dynamic test we choose to perform a series of measurements in a very noisy environment: in a small bus with a running motor at different degree of power in order to produce a spectrum of vibration as large as possible. Figure 4-20 shows the mounting of the table inside the small bus as well as the last modification applied to the system.



Figure 4-20: The last modified system mounted inside a small bus for the first dynamic test.

The results of these measurements are shown in Figure 4-21. The curve marked by ▲ corresponds to the vibrations measured directly on the metallic floor of the bus and the one marked by ■ to those measured on the lower plate of the hanging table. It is clear that the modifications brought to the system improved its performances significantly.

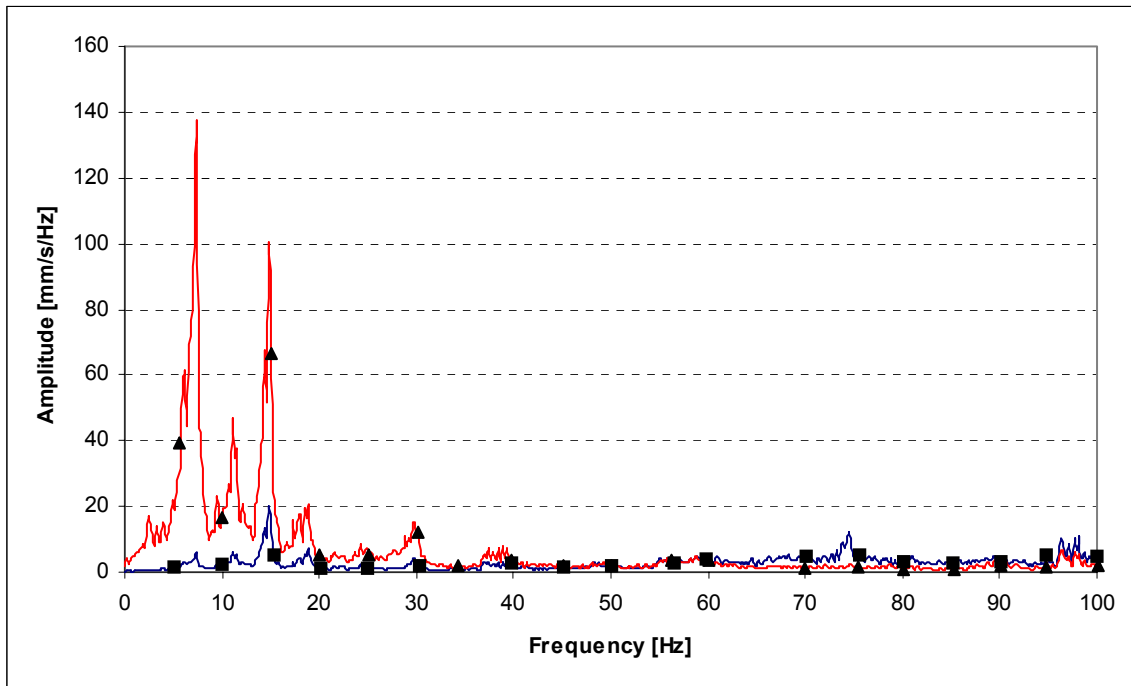


Figure 4-21: Transfer functions of the platform of the second generation determined during the first dynamic test. ▲: Measurements on the metallic floor of the bus. ■: Measurement on the lower plate of the hanging table.

4.6 Conclusion

By comparing the remaining aircraft vibrations after the application from the respective transfer function of the three attenuation systems, it is clearly seen that the best-suited mechanical filter is the hanging table. The amplitudes in the case from the hanging table are, in the domain from 5 Hz to 150 Hz lower the 15 *mGal*, which corresponds to the desired accuracy.

5 Laboratory tests

5.1 Introduction

In this chapter, we will describe the different experiences carried out in the laboratory (ETH-Hönggerberg, HPV, B113). We started by comparing the value obtained during a series of measurements and the value of the absolute station at the ETH-Hönggerberg (Fundamental station of Switzerland). In a second stage, we validated the application software we developed at the GGL (called g-GGL) by comparison with the result obtained with the application's software of the FG5-L (called g-MGS). Then, we determined the direct influence of the support to which the gravimeter will be fastened during the flight. With the validated application g-GGL, we analyzed the behavior of the components of the FG5-L gravimeter working in almost perfect measuring conditions. These components are: the laser, which allows measuring the position of the falling prism and the GT650 (Guide Technology Inc.) card, which is dedicated to the time measurements. The results will serve as reference during the dynamic measurements and will also allow an analysis of the sources of errors.

5.2 Familiarization with the FG5-L

Because a failure generated by the transport could not a priori be excluded we did some preliminary experiments in the laboratory. The FG5-L was setup, and the values obtained from a series of measurements were compared with the absolute value determined with a standard FG5. Because both measurement points were not located at the same place the reference value (g_{ref}) was obtained by a relative measurement between the laboratory and the reference station of Zurich (ETH-Hönggerberg, room A41 in building HIL).

$$g_{ref} = 980'646.73 \pm 0.04 \text{ [mGal]}$$

The FG5-L system measures the movement of the reference mirror during the drop of the falling prism by means of a seismometer Lennartz 5 s to which the signal is digitalized at 800 Hz. The recorded and integrated signal is synchronized, and then introduced as observable into the equation of movement of the falling prism (3.5). The value of g is then determined by least squares adjustment.

The value obtained during the test and at the height of the bottom of the falling chamber was:

$$g = 980'646.675 \pm 0.4 \text{ [mGal]}$$

This value corresponds to a mean obtained from 100 drops. The statistical distribution of these results is shown in Figure 5-1.

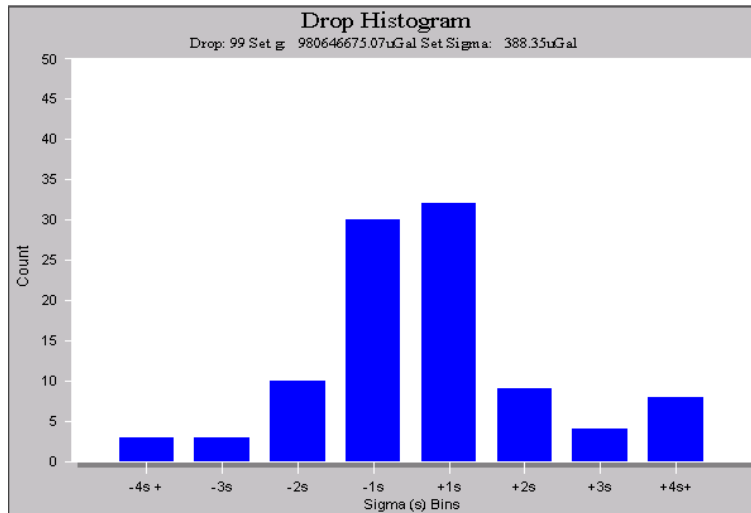


Figure 5-1: Statistical distribution of the results of the 100 drops used as test measurements

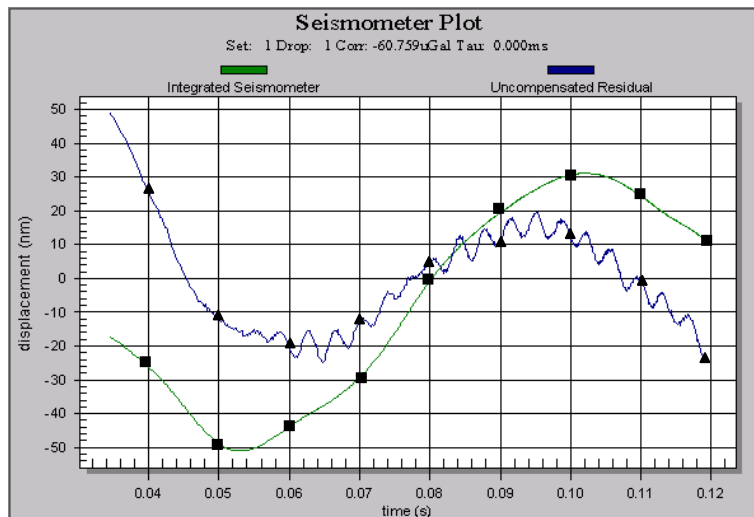


Figure 5-2: Correlation between gravity and seismometer measurements. The curve marked by ■ shows the integrated Lennartz signal, and the curve marked by ▲ one the residuals.

The strong correlation between the position of the arm of the seismometer and the relative position of the prism is clearly seen in Figure 5-2. The curve marked by ■ represents the integrated output of the seismometer. The curve marked by ▲ represents the residuals corresponding to the difference between the estimated position obtained by least squares adjustment and the real position of the falling prism.

Figure 5-3 shows the same residuals after a correction for the inaccurate relative position of the prism has been applied.

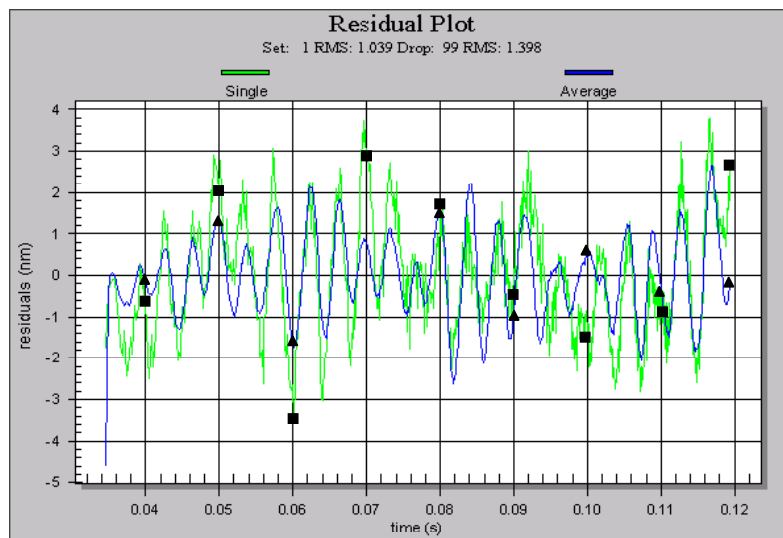


Figure 5-3: Residuals after the application of the correction. The curve marked by ■ shows the residuals obtained after compensation and the one marked by ▲ corresponds to the average over the residual function .

The comparison of the residuals before and after the compensation shows a clear and significant improvement. The improvement is of a factor of around **8**. It also shows clearly that the FG5-L gravimeter works correctly and that its accuracy is sufficient for airborne applications

5.3 FG5-L combined with an Episensor and software validation

The amplitudes of the perturbing accelerations generated by the movements of the aircraft and its engines being much larger than the capacity of measurement of the seismometer Lennartz it was necessary to find another solution for compensating these accelerations.

The solution was to replace the seismometer Lennartz by a tri-axial accelerometer Episensor made by the company Kinematics. The most important characteristics of this sensor and of its digitizing board are summarized in Table 3-2.

The FG5-L system has a graphical application's software, allowing to re-process the data acquired with different parameters like number of fringes, tolerated sigma, and so on. This software very well adapted for laboratory measurements had to be strongly modified in order to be able to process data acquired with many different dynamic configurations.

In order to validate our own application software (g-GGL), we processed the same set of data with both packages. For that we proceeded as follow: First we used the measurements obtained by means of the FG5-L and the seismometer Lennartz. In the second step, we used the measurements of the Episensor in the g-GGL software application and finally we compared the results with those obtained by means of the software g-MGS and the seismometer Lennartz.

Comparison between 'g-MGS' and 'g-GGL':

During this comparison no compensation other than the Lennartz measurements was taken into account in the 'g-MGS' application and all the values of g were used for the estimation of the mean and the standard deviation.

The results of this comparison are summarized in Table 5-1.

	g [mGal]	σ [mGal]	$\delta = g_{ref} - g $ [mGal]
g-MGS	980646.136	1.675	0.592
g-GGL	980646.533	1.325	0.195

Table 5-1: Summary of the results obtained during the comparison between the g-MGS and the g-GGL software packages. The obtained results are not showing significant differences.

Even if though the results obtained by the two software packages are not completely equal the order of magnitude is clearly reached.

The results obtained with the g-GGL software show a standard deviation and a deviation from the reference value slightly better. However, these results should be confirmed by a more detailed study of both packages and a comparison based on a larger number of measurements. In the frame of this project we assume that the g-GGL software works correctly despite the very small differences seen in the results.

Comparison Lennartz – Episensor:

As already mentioned the seismometer Lennartz is not able to measure amplitudes of movements higher than 50 *mm/s*. Its performances are not sufficient for correctly recording the velocities generated by the aircraft because these can be higher than 70 *mm/s* in the low frequencies. It is, therefore, essential to use a supplementary sensor able to measure such accelerations. To the opposite of the Lennartz seismometer the Episensor accelerometer has the characteristics required for this task (see Table 3-2). The aim of the next experiment was to compare the results obtained with the system equipped with the Lennartz seismometer working in compensation mode with the results obtained by compensation with the external accelerations acquired with the Episensor data.

The results of this comparison are summarized in Table 5-2.

	g [mGal]	σ [mGal]	$\delta = g_{ref} - g $ [mGal]
$g\text{-GGL}_{Lennartz}$	980646.533	1.325	0.195
$g\text{-GGL}_{Episensor}$	980646.481	2.310	0.247

Table 5-2: Summary of the results obtained during the comparison between Lennartz compensation and Episensor compensation. The differences in the standard deviations is due to the difference of the sampling rate of the tow sensors.

As shown in Table 5-2 the compensation made by means of the Episensor give similar results as those obtained with the seismometer Lennartz. The only significant difference appears in the standard deviations σ . This can be explained by the different sampling rates of the two sensors: The seismometer Lennartz samples at 800 *Hz* whereas the Episensor samples at 500 *Hz*. It is, however, worth nothing that the Episensor can be configured to samples at 1000 *Hz*.

Both laboratory experiments show that with the use of an accelerometer like the Episensor coupled with the *g-GGL* software it is possible to obtain the same value of *g* as obtained with the seismometer Lennartz and the software *g-MGS*. Following this conclusion we will use for the dynamics experiments the software *g-MGS* for the data acquisition whereas the data will be processed using the *g-GGL* software.

5.4 Influence of the platforms

For the AAG experiment we planned two different setup configurations. The first was the strapped-down setup in which all instruments, FG5-L, IMU and Episensor, are fastened to a platform that is fixed to the airplane rails. In the second configuration, the instruments are fastening on the platform trough a damping table. After Niebauer (*Niebauer et al.* 1995) the floor or platform recoil has a great influence on the quality of the measurements. The variation of the length of the optical path is given by the deflection of the supporting platform. For a square plate clamped at the edge, the deflection is given by:

$$\delta z = \frac{Fl^2}{4Et^3} \quad (5.1)$$

Where :

E : Elastic modulus

F : Force

l : length

t : thickness

The recoil is generated at the beginning and at the end of each drop by the accelerations and decelerations of the drag-free chamber. From equation (5.1) it is clear that a table with a large elastic modulus is needed so that deflections are kept as small as possible. Another necessary quality of the table is that it has to have a high attenuation factor so that the oscillations decrease as fast as possible.

5.4.1 Influence of the strap-down table

The characteristics needed for a strap-down system correspond to those of a good optical table. For this choice different optical tables were tested. The best results were obtained with a table “Clean Top II” from TCM (Technical Manufacturing Corporation, USA) shown in Figure 5-4.



Figure 5-4: Optical table “Clean Top II” from TMC

The optical table Clean Top II is made of an upper plate of steel, drilled and taped in a square grid of 25 mm. The body of the table has a honeycomb structure with, and below each hole a damper of Nylon is stuck to the upper plate by a layer of Epoxy glue (Figure 5-5)



Figure 5-5: Structure of the body of the “Clean Top II” table

Such a structure has an almost ideal characteristic for our application (Figure 5-6)

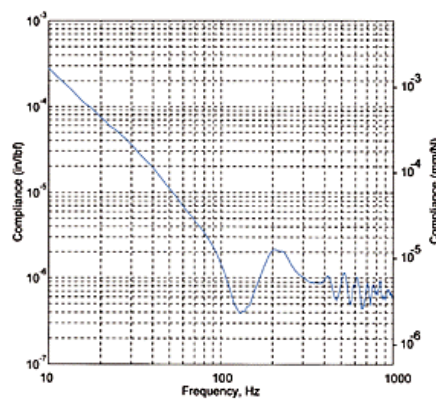


Figure 5-6: Frequency response of the table “Clean Top II”

The frequency response of the table being given in mm/N and considering that the falling prism has a mass of 0.02 kg the amplitude of the oscillations of the table will be approximately 2 nm at 200 Hz and 200 nm at 10 Hz.

The mechanical configuration used for this experiment is depicted in Figure 5-7

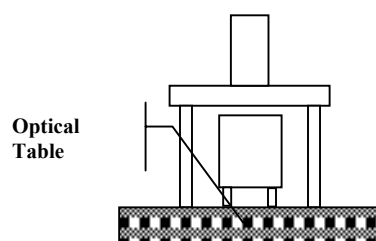


Figure 5-7: Block diagram of the experimental mounting with the optical table. The gravimeter FG5-L was mounted on the optical table “Clean Top II”.

With this configuration the g value measured at the reference point was:

$$g = 980'646.348 \pm 5 \text{ [mGal]} \quad \text{instead of} \quad g_{ref} = 980'646.728 \pm 0.04 \text{ [mGal]}$$

showing a difference of:

$$\Delta g = |g - g_{ref}| = 0.38 \text{ [mGal]}$$

The result shows a clear degradation of the measured value of g . The difference to the reference value of g is still on the same order of magnitude as when the gravimeter is working on the ground. The influence of the support clearly appears in the sigma of the estimated g , but this value is still inside the required domain of precision.

5.4.2 Influence of the platform the damping table

In chapter 0, we saw that the most appropriate damping system is the hanging-table. In this system the platform to which the instrument is fastened is made of two 25 mm thick honeycomb aluminum plates stuck together in order to decrease the deflection. On top of the aluminum plate two concentric 9 mm neoprene plates are stuck for increasing the damping factor. The interferometer is placed on the middle of the central neoprene plate whereas the tripod of the dropping chamber is on the external plates as depicted in Figure 5-8

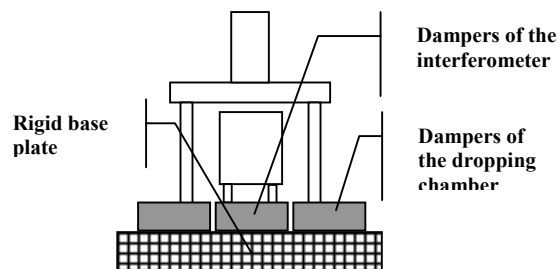


Figure 5-8: Block diagram of the system of decoupling by means of dampers

In this configuration the value of g measured at the reference point was:

$$g = 980'647.175 \pm 5.3 \text{ [mGal]} \quad \text{instead of} \quad g_{ref} = 980'646.728 \pm 0.04 \text{ [mGal]}$$

showing a difference of

$$\Delta g = |g - g_{ref}| = 0.45 \text{ [mGal]}$$

The results obtained with this configuration are not as good as those obtained with the optical table but are in the required order of magnitude.

5.5 Detailed analysis of a g measurement in laboratory

This chapter is dedicated to an analysis of the behavior of the components of the FG5-L gravimeter working in almost perfect measuring conditions. The components of the instrument are: the laser, which allows measuring the position of the falling prism and the GT650 (Guide Technology Inc.) card, which is dedicated to the time measurements. The results obtained with analysis will serve as reference during the dynamics measurements and will also allow an analysis of the sources of errors.

5.5.1 Least squares adjustment

The method of analysis used for this study is based on a least-squares adjustment of a model of the measurements. The analysis of the observations and of the adjustment parameters will give information on the quality of the model and on the accuracy of the measurements.

5.5.1.1 Theory

Generally the numerical treatment of a set of data is based on a mathematical model, which has to be solved (*H.H. Schmid, 1997*). The model has to be in the form:

$$\mathbf{F}(\mathbf{y}) = \mathbf{0} \quad (5.2)$$

The vector \mathbf{y} can be divided in two groups: the first group consisting of the measured values \mathbf{L} , and the second group consisting of the values to be determined which are the parameters \mathbf{x} . Then equation (5.2) can be written:

$$\mathbf{F}(\mathbf{L}, \mathbf{x}) = \mathbf{0} \quad (5.3)$$

The measured values being affected by a error of measurement they can be decomposed into observations, \mathbf{l} and improvements \mathbf{v}_1 .

$$\mathbf{L} = \mathbf{l} + \mathbf{v}_1 \quad (5.4)$$

The system (5.3) being not linear by definition it can be linearized by means of decomposition in a Taylor series of first order.

Setting \mathbf{x}^0 as the close value of the parameters to be estimated and Δ the vector containing the corrections to be applied on the approximate values one can write:

$$\frac{\partial \mathbf{F}}{\partial \mathbf{L}} \mathbf{v}_1 + \frac{\partial \mathbf{F}}{\partial \mathbf{x}} \Delta = -\mathbf{F}(\mathbf{l}, \mathbf{x}^0) \quad (5.5)$$

Then (5.5) represents a system of equations which can be represented in matrix form as follow:

$$\mathbf{A}_1 \mathbf{v}_1 + \mathbf{B} \Delta = \mathbf{w}_1 \quad (5.6)$$

With

$$\mathbf{A}_1 = \frac{\partial \mathbf{F}}{\partial \mathbf{L}}; \quad \mathbf{B} = \frac{\partial \mathbf{F}}{\partial \mathbf{x}}; \quad \mathbf{w}_1 = -\mathbf{F}(\mathbf{l}, \mathbf{x}^0)$$

This system can be completed by some constraints between the parameters, which have to be considered. In a general manner the system of equations related to these conditions can be written as:

$$\mathbf{G}(\mathbf{x}) = \mathbf{0} \quad (5.7)$$

In matrix form (5.7) can be written as:

$$\mathbf{C}\Delta = \mathbf{w}_c \quad (5.8)$$

with:

$$\mathbf{C} = \frac{\partial \mathbf{G}}{\partial \mathbf{x}}; \quad \mathbf{w}_c = -\mathbf{G}(\mathbf{x}^0);$$

The method of least-squares adjustment of Gauss minimizes $\mathbf{v}_1^T \mathbf{P}_1 \mathbf{v}_1$ taking into account the conditions (5.6) and (5.8) where the matrix \mathbf{P} is the weighting matrix having on its diagonal the inverse of the square of the resolution of the different observed values. In order to be able to solve such a system it is necessary to introduce some Lagrangian multipliers as help parameters. The system to be minimized can then be written:

$$\phi = \mathbf{v}_1^T \mathbf{P}_1 \mathbf{v}_1 - 2\mathbf{k}_1^T (\mathbf{A}_1 \mathbf{v}_1 + \mathbf{B}\Delta - \mathbf{w}_1) - 2\mathbf{k}_c^T (\mathbf{C}\Delta - \mathbf{w}_c) \quad (5.9)$$

where the vectors \mathbf{k}_1 and \mathbf{k}_c correspond to the Lagrangian multipliers and are called correlation's vectors

In order to minimize (5.9) it is necessary to set the partial derivatives with respect to \mathbf{v}_1 and Δ to zero. This produces the following equations:

$$-\mathbf{P}_1 \mathbf{v}_1 + \mathbf{A}_1^T \mathbf{k}_1 = \mathbf{0} \quad (5.10)$$

and

$$\mathbf{B}^T \mathbf{v}_1 + \mathbf{C}^T \mathbf{k}_c = \mathbf{0} \quad (5.11)$$

The necessary system of equations for the estimation of the improvements \mathbf{v}_1 , of the correlation vectors \mathbf{k}_1 and \mathbf{k}_c as well as the correction vector Δ by means of equations (5.6), (5.7), (5.10) and (5.11) can be written

$$\begin{array}{|c|c|c|c|} \hline -\mathbf{P}_1 & \mathbf{A}_1^T & \mathbf{0} & \mathbf{0} \\ \hline \mathbf{A}_1 & \mathbf{0} & \mathbf{B} & \mathbf{0} \\ \hline \mathbf{0} & \mathbf{B}^T & \mathbf{0} & \mathbf{C} \\ \hline \mathbf{0} & \mathbf{0} & \mathbf{C}^T & \mathbf{0} \\ \hline \end{array}
 \quad
 \begin{array}{|c|} \hline \mathbf{v}_1 \\ \hline \mathbf{k}_1 \\ \hline \Delta \\ \hline \mathbf{k}_c \\ \hline \end{array}
 =
 \begin{array}{|c|} \hline \mathbf{0} \\ \hline \mathbf{w}_1 \\ \hline \mathbf{0} \\ \hline \mathbf{w}_c \\ \hline \end{array}
 \quad (5.12)$$

Such a system can be solved in two steps. In a first step the constraints in the matrix \mathbf{C} are not taken into account. Then the corrections are determined by inversion.

$$\Delta^0 = \mathbf{N}_1^{-1} \mathbf{w}_1^* \quad (5.13)$$

with

$$\mathbf{N}_1 = \mathbf{B}^T (\mathbf{A}_1 \sigma_1 \mathbf{A}_1^T) \mathbf{B}$$

$$\mathbf{w}_1^* = \mathbf{B}^T (\mathbf{A}_1 \sigma_1 \mathbf{A}_1^T) \mathbf{w}_1$$

$$\mathbf{w}_1 = \mathbf{A}_1 \sigma_1 \mathbf{A}_1^T \mathbf{k}_1$$

$$\sigma_1 = \mathbf{P}_1^{-1}$$

then a correction's vector $\delta\Delta$ is determined :

$$\delta\Delta = \mathbf{N}_1^{-1} \mathbf{C}^T (\mathbf{C} \mathbf{N}_1^{-1} \mathbf{C}^T)^{-1} (\mathbf{w}_c - \mathbf{C} \Delta^0) \quad (5.14)$$

The final result is obtained by adding the two correction's vectors

$$\Delta = \Delta^0 + \delta\Delta \quad (5.15)$$

By using Δ it is possible to determine the correlation's vectors \mathbf{k}_1 and \mathbf{k}_c and the improvements \mathbf{v}_1 as follow:

$$\mathbf{k}_1 = (\mathbf{A}_1 \sigma_1 \mathbf{A}_1^T)^{-1} (\mathbf{w}_1 - \mathbf{B} \Delta)$$

$$\mathbf{v}_1 = \sigma_1 \mathbf{A}_1^T \mathbf{k}_1$$

With the help of the improvement's vector one can determine the mean error after the adjustment in the following manner:

$$m_o = \left(\frac{\mathbf{v}_1^T \mathbf{P}_1 \mathbf{v}_1}{r + s - u} \right)^{1/2} \quad (5.16)$$

With

r : number of state's equations

u : number of unknown to be determined

s : number of supplementary constraints

The value m_o can be considered as a normalized standard of the inaccuracy induced by the unavoidable measuring errors. Similarly it is possible to obtain the mean error of the measurements \mathbf{l} before the adjustment by:

$$\mathbf{m}_l^2 = m_o^2 \sigma_1 \quad (5.17)$$

Finally it is necessary to calculate the errors on the parameters to be estimated by determining the covariance matrix $\mathbf{C}_{\Delta\Delta}$. This one contains on its diagonal the square of the standard deviations of the estimated parameters and can be calculated by:

$$\mathbf{C}_{\Delta\Delta} = m_o \mathbf{N} \quad (5.18)$$

In order to be able to estimate the influences of the different estimated parameters to each other, it is worth computing the correlation's matrix \mathbf{K} .

$$\mathbf{K} = \begin{bmatrix} \mathbf{1} & \mathbf{k}_{ij} & & \\ & \dots & & \\ & & \dots & \\ & & & \dots & \\ & & & & \mathbf{1} \end{bmatrix}; \quad \mathbf{k}_{ij} = \frac{n_{ij}}{\sqrt{n_{ii}n_{jj}}}$$

The \mathbf{k}_{ij} give an indication on the propagation's probability of the error of the parameter \mathbf{i} on the parameter \mathbf{j} .

We now have a method allowing us to analyze the instrument as well as the quality of the mathematical model with the help of m_o and m_l .

5.5.2 Statistical analysis

After having analyzed the different parameters of the physical model we have to answer the following questions:

- 1- Does the whole system (acquisition and estimation) work satisfactorily?
- 2- What is the quality of the physical model?
- 3- What are the limits of confidence of the estimated parameters?

The answers to these questions can be found in the different methods of statistical analysis briefly described below.

Proper functioning

In order to be able to answer this question we will use a test of hypothesis. Suppose that the estimated values (g, v_o, x_o) , have all a normal distribution. In this case the distribution of their reduced values Z_g, Z_{x_o} and Z_{v_o} is a normal reduced distribution with its mean value equal to zero and of a variance equal to one.

$$Z_i = \frac{m_i - M_i}{\sigma_i} \quad (5.19)$$

With:

Z_i : Reduced variable (Z_g, Z_{v_o}, Z_{x_o})

m_i : Mean value of the sample ($\bar{g}, \bar{v}_o, \bar{x}_o$)

M_i : Mean value of the set ($\bar{g}_{theo}, \bar{v}_{o,theo}, \bar{x}_{o,theo}$)

σ_i : Variance of the sample ($\sigma_g, \sigma_{v_o}, \sigma_{x_o}$)

The number of measurements used for the determination of g during one drop being clearly larger than 30, it is justified to use a normal test.

This test is based on equation (5.19) and tells us if Z_i , for which the normal distribution is inside the critical domain defined by the limits z_c we can assert that the measurement is correct with a probability p % (see Figure 5-9).

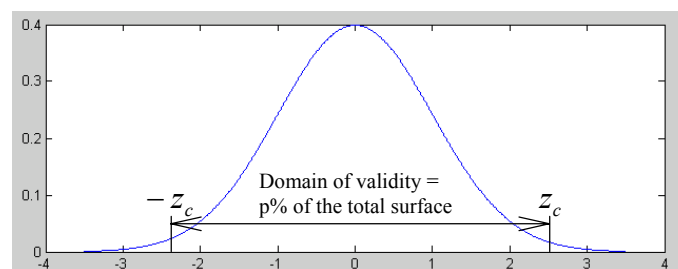


Figure 5-9: The values $\pm z_c$ are defining the domain of validity

We will then make the hypothesis H_0 that the measured value of g is equal to the reference value g_{ref} , and we will test this affirmation with a level of significance α . This has as consequence that if g_{mes} satisfies the conditions described by (5.20) the result obtained for g is more significant.

$$-z_c \leq \frac{g_{mes} - g_{ref}}{\sigma_g} \leq z_c \quad (5.20)$$

For a level of significance of $\alpha = 0.01$, $z_c = 2.58$ (Schaum *Probabilités et Statistique*).

Differently formulated it means that if g_{mes} satisfy (5.20) it is possible to assert that the system has correctly worked with 99 % probability

Quality of the physical model

For determining the quality of the physical model we will determine a correlation coefficient r for each drop.

$$r^2 = \frac{\sum (z(t_i) - \bar{z}_{meas})^2}{\sum (z_{meas} - \bar{z}_{meas})^2} \quad (5.21)$$

This factor reveals the correlation between z and t as a function of the model linking these two variables. The closer r is to 1, the closer the model represents the physical reality of the phenomenon we are trying to describe.

Limits of confidence of the estimated parameter

With the help of (5.19), it is also possible to determine the domain of validity of the estimated parameters with a level of confidence α . Like for the check of the proper working of the system we can formulate the hypothesis H_0 that the other parameters are equal to their theoretical value.

For g_{mes} one can then compute the domain of validity at the level of confidence $\alpha = 0.01$ with:

$$g_{mes} = g_{ref} \pm z_c \sigma_g \quad (5.22)$$

This allows to asserting that with in 99 % of certainty g_{mes} is located inside the window defined by (5.22).

The answers to the three questions mentioned above give us a good information about the functioning of the instrument and about the quality of the measurements.

5.5.3 Frequency analysis

A frequency analysis of the measurements should give information about the relationship between the quality of the estimation of g , and the frequency distribution of the perturbations. As already mentioned in chapter 3.3.2.1 the position of a falling body in a homogeneous gravity field is given by

$$z(t) = 0.5gt_n^2 + v_o t_n + z_o \quad (5.23)$$

The amplitude spectrum of (5.23) is given by:

$$|H(\omega)| = \sqrt{\frac{\omega^2 v_o^2 + (g + x_o \omega^2)^2}{\omega^6}}$$

setting $x_o = v_o = 0$, one obtains for the amplitude spectrum

$$|H(\omega)| = \frac{g}{\omega^3} \quad (5.24)$$

The major part of the energy of the amplitude spectrum described by (5.24) is concentrated between 0 and 10 Hz. It is then justified to suppose that the perturbations with frequencies lying in the domain 0-10 Hz have a greater influence on the quality of the estimation of g than those lying outside this domain.

5.5.4 Analysis of the measurements carried out in the laboratory

In the following there is an analysis of a set of measurements containing 200 drops measured in the laboratory B113, HPT Höggerberg. At the end of this analysis we should be able to answer the following questions:

1. Do the components of the FG5-L operate with a satisfactory resolution?
2. What is the resolution of g one can expect after a single drop?
3. What is the influence of the spectral distribution of the perturbation on the quality of g ?

5.5.4.1 Analysis of the FG5-L components

The principal components of the FG5-L gravimeter are the GT650 card for the time measurements, the laser for the measurement of positions and the EpiSensor for the measurements of the external perturbing accelerations.

The results obtained after adjustment for these components are summarized in Table 5-3.

$g_{estimated}$ [mGal]	980646.601	$\sigma = 2.284$
	Expected errors	Estimated mean error
Time FG5-L [ns]	~1	< 1
Position FG5-L [nm]	~1	< 1
Position EpiSensor [nm]	~5	< 1
Mean error [nm]	-	2.5

Table 5-3: Comparison between estimated and expected errors

Based on these results we can assume that the three principal components of the FG5-L work correctly, and their resolutions correspond to the ones expected. However it is worth noting that the errors estimated strongly depend on the physical model used for the least-squares adjustment.

5.5.4.2 Expected resolution for one single drop

The results obtained below are the mean value computed from 200 measurements. It is important to note that in airborne conditions it is not possible to carry out several measurements at the same point! However, we will try to estimate the obtainable resolution in flight condition from the 7000 values recorded during one drop. For this we will carry out a test on the equality hypothesis as described in chapter 5.5.2.

As hypothesis H_o we set that the mean value of g for a single drop g_{Drop} , has to be equal to the reference value g_{ref} , and we will test it for a confidence level of $\alpha = 0.01$

$$H_o : \bar{g}_{Drop} = g_{ref} = 980646.728[\text{mGal}]$$

The diagram in Figure 5-10 shows the results obtained for each drop.

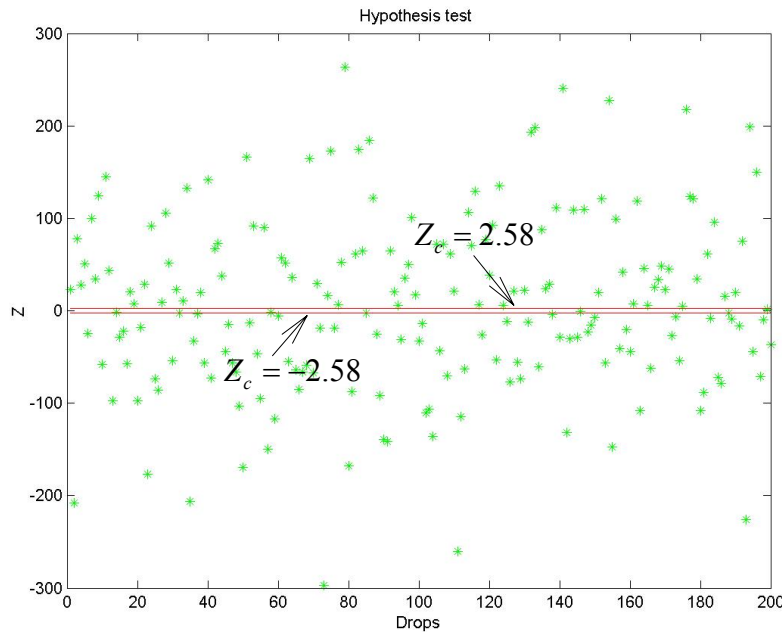


Figure 5-10: Results of the hypothesis test for each of the 200 drops. The two lines are showing the upper and lower limits of validity Z_c

Based on the results of the test of H_o , obtained for each drop it is possible to reject this hypothesis with 99 % certainty, this for 95 % of the cases. In a first view this is surprising but it simply represents the reality. Every drop gives a value of g stained with a systematic error and represents an instantaneous state of the sum of the local accelerations a_l . The least-squares adjustment allows the determination of the mean of the standard deviation for one drop $\bar{\sigma} = 0.0305[\text{mGal}]$.

It is worth noting that a_l can be determined with a good resolution but the unique method to obtain the real value of g is to determine the mean value of a large number of drop in such a manner that the systematic errors cancel.

From these results we can get very valuable information: with the results determined by means of the inequality (5.20) we are able to estimate the value of σ for which the hypothesis H_o is valid. This value of σ will, therefore, correspond to σ_{Drop} which one can expect during the estimation of g obtained with a single drop.

We then obtain:

$$\sigma_{Drop} \cong 2.5 [\text{mGal}]$$

The diagram of Figure 5-11 shows the result of the test of H_o taking into account σ_{Drop} .

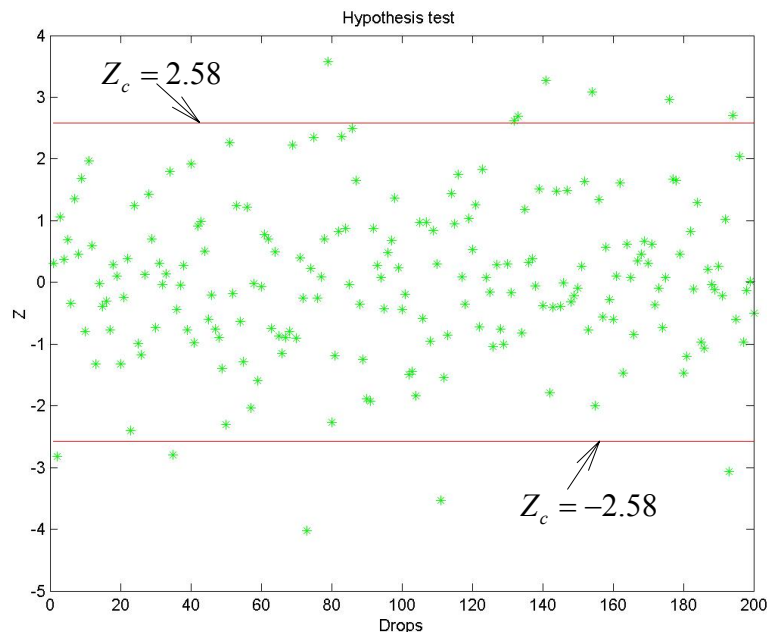


Figure 5-11: Results of the hypothesis test for each of the 200 drops taking into account σ_{Drop}

These results allow us to assert that for more than 95 % of the drops the hypothesis H_o can be accepted with a level of significance of 0.01.

We can then conclude that for a drop with 7000 points of measurements the standard deviation expected is on the order of 2.5 *mGal*. It is also worth noting that the value of σ_{Drop} is on the same order of magnitude as the standard deviation obtained by means of the adjustment (see Table 3-1).

5.5.4.3 Spectral analysis

We will now investigate the spectral distribution of the environmental accelerations and their influence on the quality of the determination of g .

The diagrams of Figure 5-12 show the function of the residuals we obtain by classical adjustment (\blacktriangle) (without taking into account the movements recorded by the external sensor represented in the lower graphic (\bullet)). As already stated in chapter 5.2, we observe a strong correlation between the residuals obtained by the classical adjustment and the movements determined by integrating twice the measures from the external sensor (EpiSensor). These two functions are represented by triangles and by circles, respectively, in Figure 2-1. The correlation between these two signals means that the measurements of the external sensor (EpiSensor) must be proportional to the movements of the reference prism during the fall.

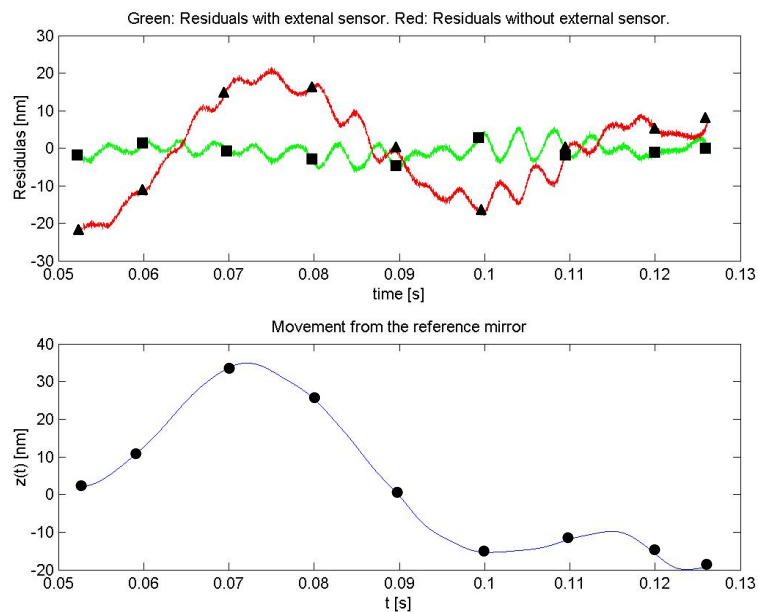


Figure 5-12: Diagrams showing the residual functions and the movement measured with the external sensor. \blacktriangle : Residual functions without taking into account the measurements of the EpiSensor. \blacksquare : Residual functions obtained by taking into account the measurements of the EpiSensor. \bullet : Movements estimated with the acquired measures from the EpiSensor.

By introducing the twice-integrated measurements of the accelerometer (EpiSensor) in the model of linear adjustment, the residuals can be reduced significantly. This can be clearly observed in the upper graphic of Figure 5-12. The function marked by \blacktriangle corresponds to the residuals obtained by classical adjustment and the one marked by \blacksquare , by taking in account the measurements of the external sensor.

The diagrams in Figure 5-14 are showing the amplitude spectrums of the three signals described above. The spectrum of the “classical” residual is represented by ▲, the spectrum of the compensated residuals ■, and the spectrum of the determined movement by ●. To be able to give an adapted interpretation of these spectra, it is necessary to have also the spectrum from the environmental accelerations. The ambient accelerations and their amplitude spectrum is represented by the graphics of Figure 5-13.

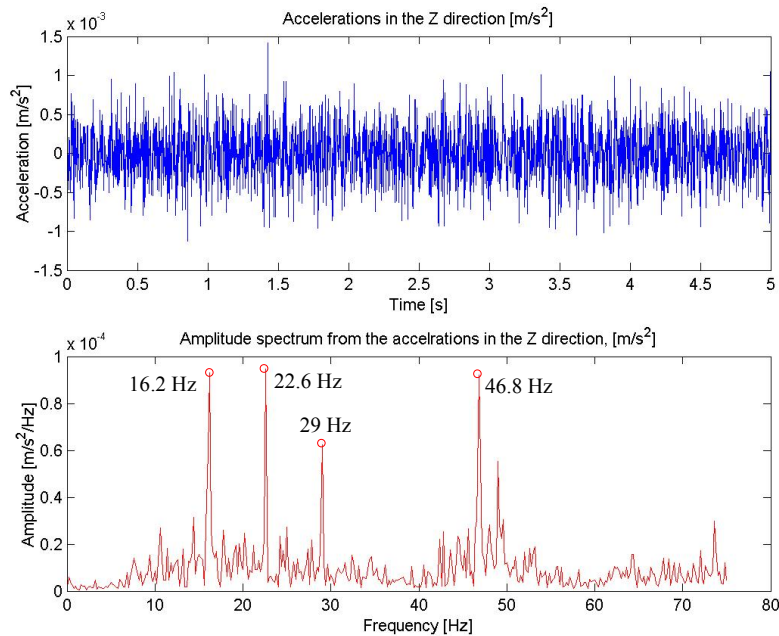


Figure 5-13: Ambient accelerations (upper diagram) and their amplitude spectrum (lower diagram). The upper diagram represents the ambient acceleration measured on the ground of the laboratory. The lower diagram represents the amplitude spectrum of these accelerations.

The amplitude spectrum from the ambient acceleration represented in Figure 5-13 shows four peaks. The ground of the laboratory room is made of a thick plate of concrete. This kind of ground has its resonance frequency at around 50 Hz. Consequently; we can say that the resonance frequency of the ground plate of the laboratory is 46.8 Hz. The other three peaks at 16.2 Hz, 22,6 Hz and 29 Hz can be attributed to other sources like machinery working around the laboratory.

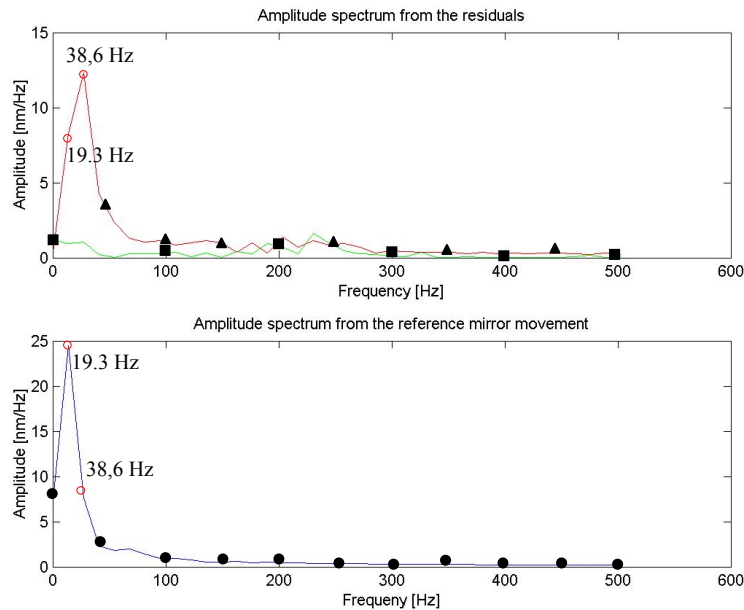


Figure 5-14: Amplitude spectrum of the residuals. The upper graph represents the amplitude spectra of the residual functions with (■ marked curve) and without (▲ marked curve) the Episensor data. Lower graph represents the amplitude spectrum of the movements recorded by the external sensor (Episensor).

The amplitude spectra from the classical residuals and from the mirror movement show the same peaks at 19.3 Hz and 38.6 Hz . These two frequencies are present in the spectrum of each drop, and because these peaks are present in the spectrum of the ambient acceleration, we can argue that these perturbations are generated by the FG5-L itself.

Based on this analysis, we can assume that the perturbations produced by the gravimeter can be partially modeled and compensated. If these perturbations can be modeled, we can also assume that environmental perturbation in the same range of frequencies can be compensated.

5.6 Conclusions

From the previous tests and analysis we conclude:

- a) The FG5-L works properly.
- b) In ideal conditions the resolution of a single drop is on the order of magnitude of 2.5 mGal .
- c) The perturbations of low-frequencies ($< 50\text{ [Hz]}$) have a great influence on the quality of the measurements. However the influence of the perturbations of environmental origin can be evaluated and introduced in the model. This results in a strong improvement of the residuals.

6 First dynamic measurement in a truck

6.1 Introduction

Before mounting the whole measurement system in an aircraft we carried out a series of tests, under different configurations in a small truck (*H. Baumann, 2002*). The questions we tried to answer with this experiment were:

- Is it possible to acquire data with the FG5-L in a very noisy environment?
- Can all the instruments be correctly synchronized?
- Which are the mechanical problems that can appear during dynamic measurements and which are the necessary modifications to be applied in order to solve these problems?
- Which are the necessary modifications to be applied to the g-GGL algorithm in order to obtain the best possible value of g ?

6.2 Location of the test line

The test area is located in the back of the building HPV of the ETHZ Höggerberg. It is a horizontal road of about 50 m length along which we first measured the g values every 2 m with a LaCoste and Romberg relative gravimeter. These measurement points were tied to the Swiss Absolute Reference station (ETH-Höggerberg, room A41 in building HIL). The maximum variation of g along this line is less than 1 $mGal$. We then considered g as constant with a mean value of $g_{the} = 980643.242 \text{ mGal}$ and a standard deviation of 0.03 $mGal$.

6.3 Experimental bus-setup

The installed system was formed with the absolute gravimeter FG5-L and only an accelerometer Episensor, the INS being not available. In order to ensure a satisfactory synchronization each sensor was connected to its own GPS receiver. Figure 6-1 gives a schematic overview of this experimental mounting.

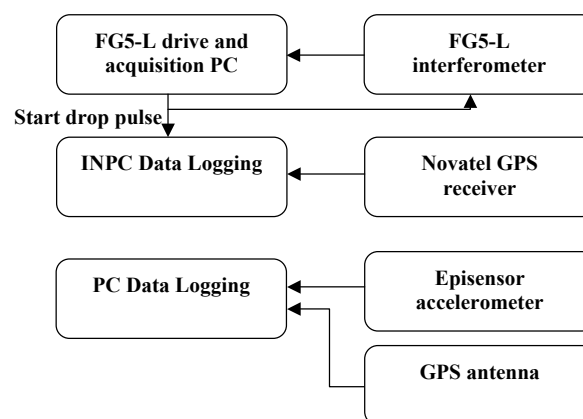


Figure 6-1: Schematic overview of the synchronization of the experimental mounting.

The triggering pulse generated by the FG5-L steering-PC is transmitted to the GPS receivers, and written into its data acquisition's file. The PC dedicated to the acquisition of the data of the accelerometer being connected to its own GPS receiver the data of the Episensor are automatically synchronized with the data of the FG5-L.

The FG5-L steering-PC triggers the fall by sending a pulse to the interferometer. This pulse is also transmitted to the PC in charge of the acquisition of the GPS data, which write the time of the arriving pulse in the data's file. With this every fall beginning is linked to the GPS time. The PC used for the acquisition of the Episensor data being synchronized to the GPS time through its own antenna all the data are referenced to the same time.

The measurement system was installed on board of a small truck in two different mechanical configurations: In a pure strapped-down and in an amortized configuration

In the pure strap-down configuration the instruments were fasten on the top of an optical table Clean Top II" from TMC (described in chapter 5.4) Figure 6-2.a while in the amortized configuration the instruments were installed on the hanging table (Figure 6-2.b).

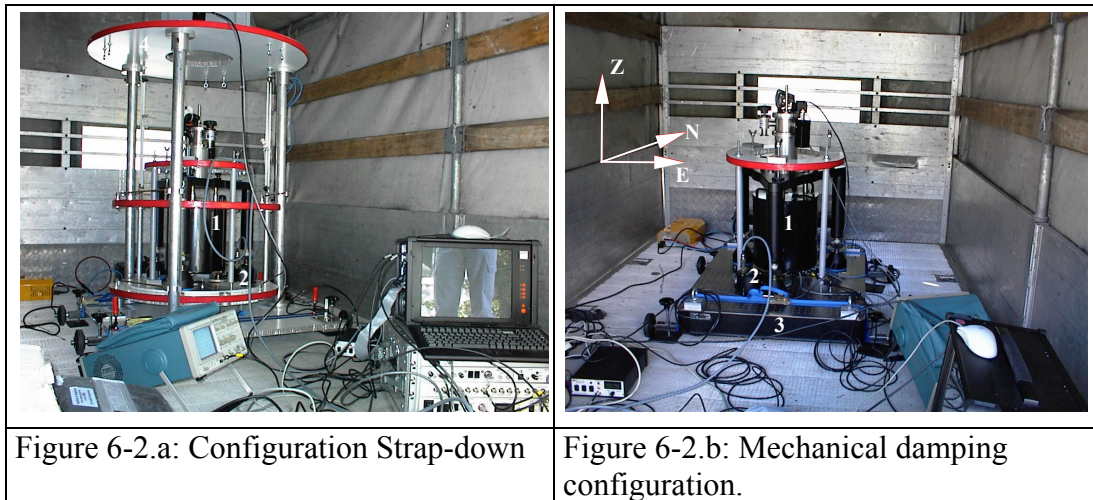


Figure 6-2: Mechanical configuration in the interior of the small truck

- a) Strapp-Down configuration
- b) Amortization's configuration

6.4 Measurements in Strap-down configuration

In this configuration three series of measurements were carried out.

During the first series the small truck was in stationary position with the engine running. During the two following series the small truck was moving with a speed of around 1 m/s along the measurement's line located in the middle of the road.

6.4.1 Static measurements

In stationary position we wanted to find the influence on g of the vibrations induced by the engine and by the resonance frequencies of the truck's suspension. In a first step we performed specific vibrations measurements in order to determine the different resonance frequencies of the truck. We then proceeded to the gravity measurements themselves consisting of 204 drops.

Frequency characteristics of the truck suspension

In order to be able to characterize the truck in its whole we performed an impulse measurement of the system. This consists in exciting the object to be studied with a shock-like jump for example. With this it is possible to determine the principal resonance frequency as well as its attenuation's factor. Figure 6-3 shows the accelerations measured in the three directions (Z = vertical, E and N = horizontal) with their corresponding amplitude spectrum.

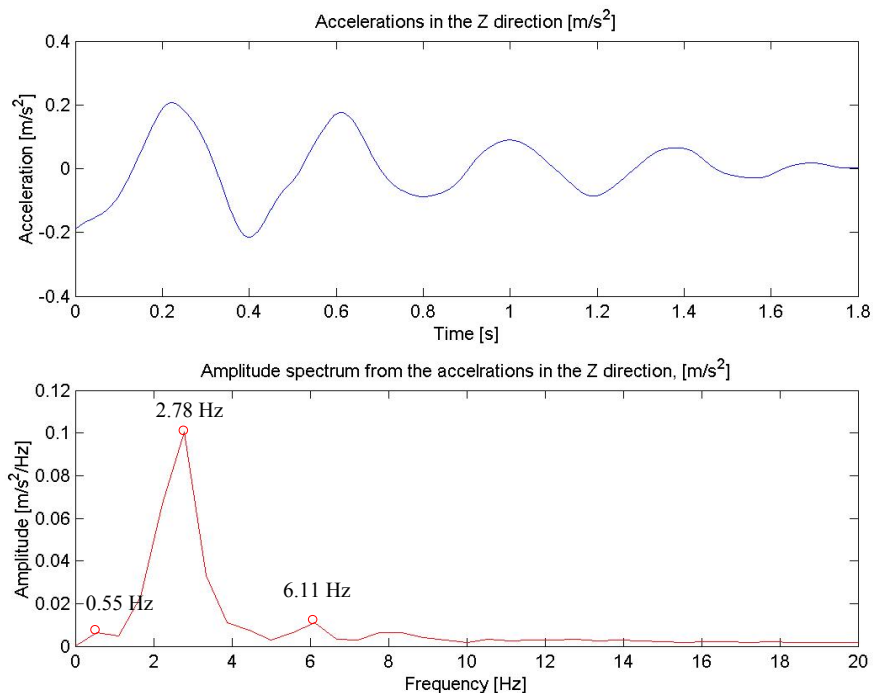


Figure 6-3: Vertical accelerations measured in the truck in static mode (upper curve) and the corresponding amplitude spectrum. The resonance frequency of the dampers is 2,78 Hz and the damping factor 4%.

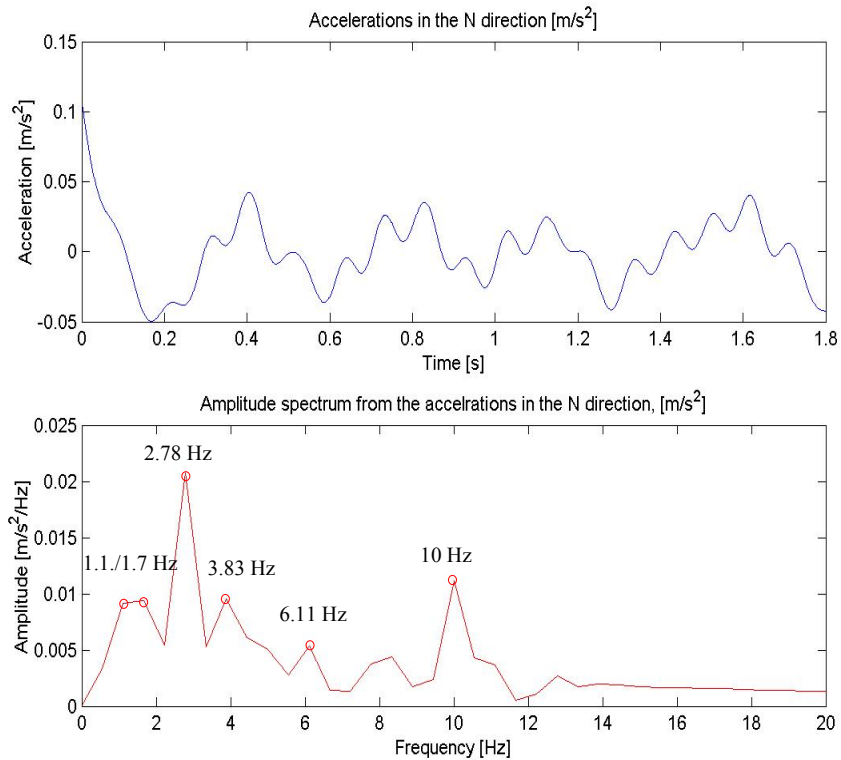


Figure 6-4: Horizontal (*N* direction) accelerations measured in the truck in static mode (upper curve) and the corresponding amplitude spectrum. The principal peak is at 2.78 Hz and the secondary peaks at 1.1/1.7 Hz, 3.83 Hz, 6.11 Hz and 10 Hz.

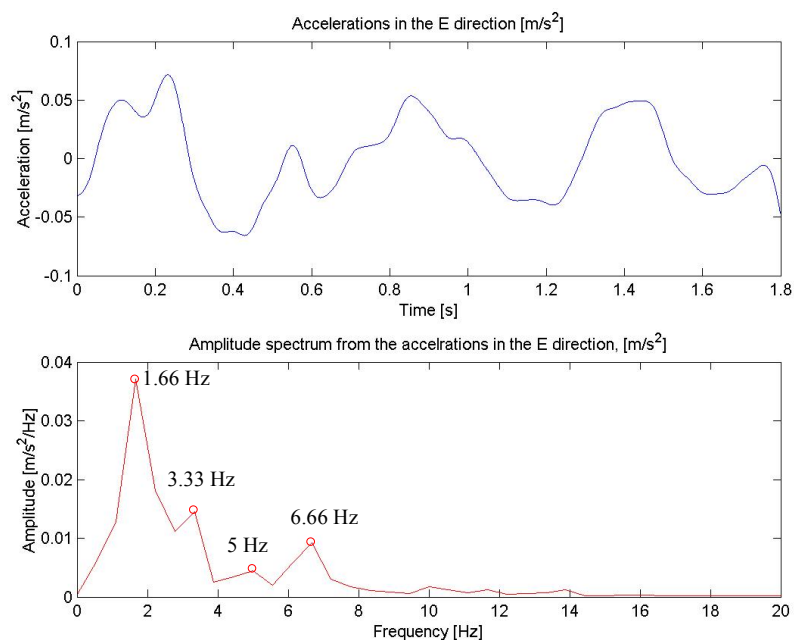


Figure 6-5: Horizontal (*E* direction) accelerations measured in the truck in static mode (upper curve) and the corresponding amplitude spectrum. The principal peak is at 1.66 Hz and three secondary peaks at 3.33 Hz, 5 Hz and 6.66 Hz.

The amplitude spectrum of the measured vertical accelerations Z (Figure 6-3) clearly shows a resonance peak at 2.78 Hz , which corresponds to the principal resonance frequency of the suspension. The damping factor of this frequency is around 4%. It is also possible to see a peak at 0.55 Hz and one at 6.11 Hz . The peaks at 2.78 Hz and 6.11 Hz are also present in the amplitude spectrum of the horizontal accelerations N (Figure 6-4). One can conclude that the sensor is not perfectly horizontal and that the horizontal accelerations are partially transmitted in the vertical component and vice versa. However, it seems that the principal resonance frequency is located around 1.7 Hz in the E direction as well as in the N one. All other observed peaks can be attributed to many origins like small differences between the resonance frequencies of the suspension's spring and/or a bad leveling of the instrument. A cross coupling between the accelerometers cannot be also excluded.

Frequencies induced by the engine of the truck

For determining the frequencies generated by the engine we carried out measurements of the accelerations during a time frame of 150 s with the engine running. Figure 6-6 to Figure 6-8 show the measured accelerations and their amplitude spectra.

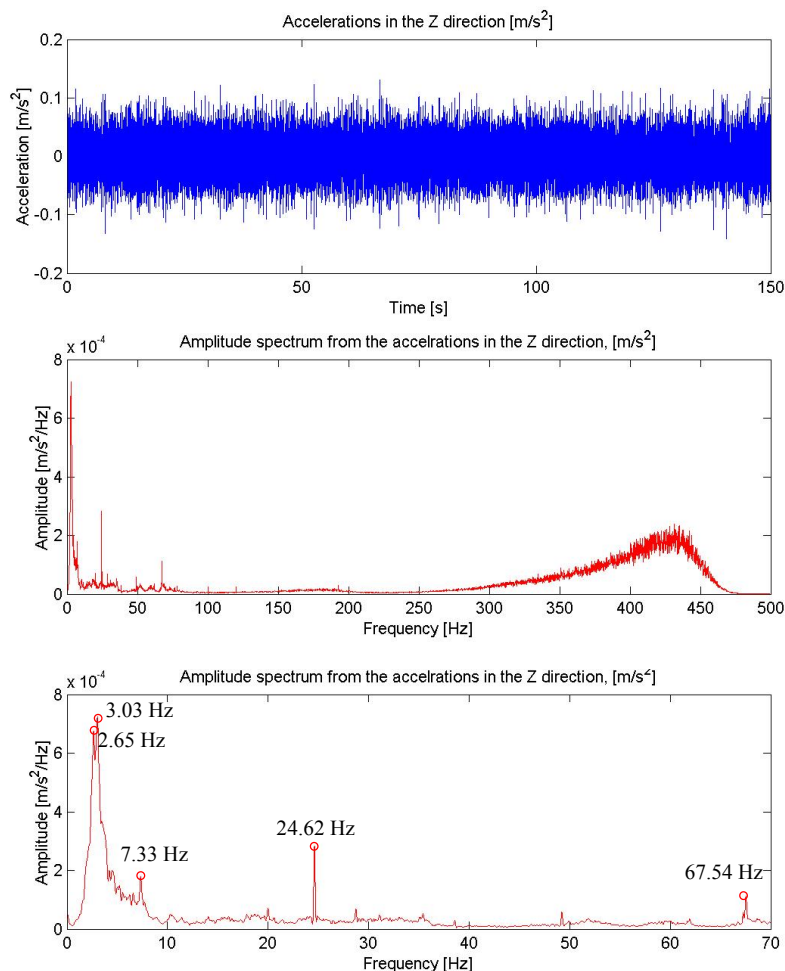


Figure 6-6: Vertical acceleration generated by the engine of the truck (upper curve) and the corresponding amplitude spectrum.

The amplitude spectrum of the vertical acceleration (Z) induced by the engine shows three peaks: at 3 Hz, 24.6 Hz and 67.5 Hz. In the high frequencies a large peak at around 420 Hz is clearly visible. These frequencies correspond to the resonance frequencies of the metal sheets of the bodywork as well as of the charge bridge. The peaks below 100 Hz are due to the resonance of the chassis and of the damping mechanism as well.

A frequency at 3 Hz is clearly visible which corresponds well with the resonance frequency already seen by the impulse excitation (Figure 6-3). The other frequencies 7.33 Hz, 24.62 Hz and at 67.54 Hz are more difficult to be interpreted but could correspond to different resonance modes of the chassis.

Figure 6-7 shows the horizontal accelerations in the N direction and their amplitude spectrum.

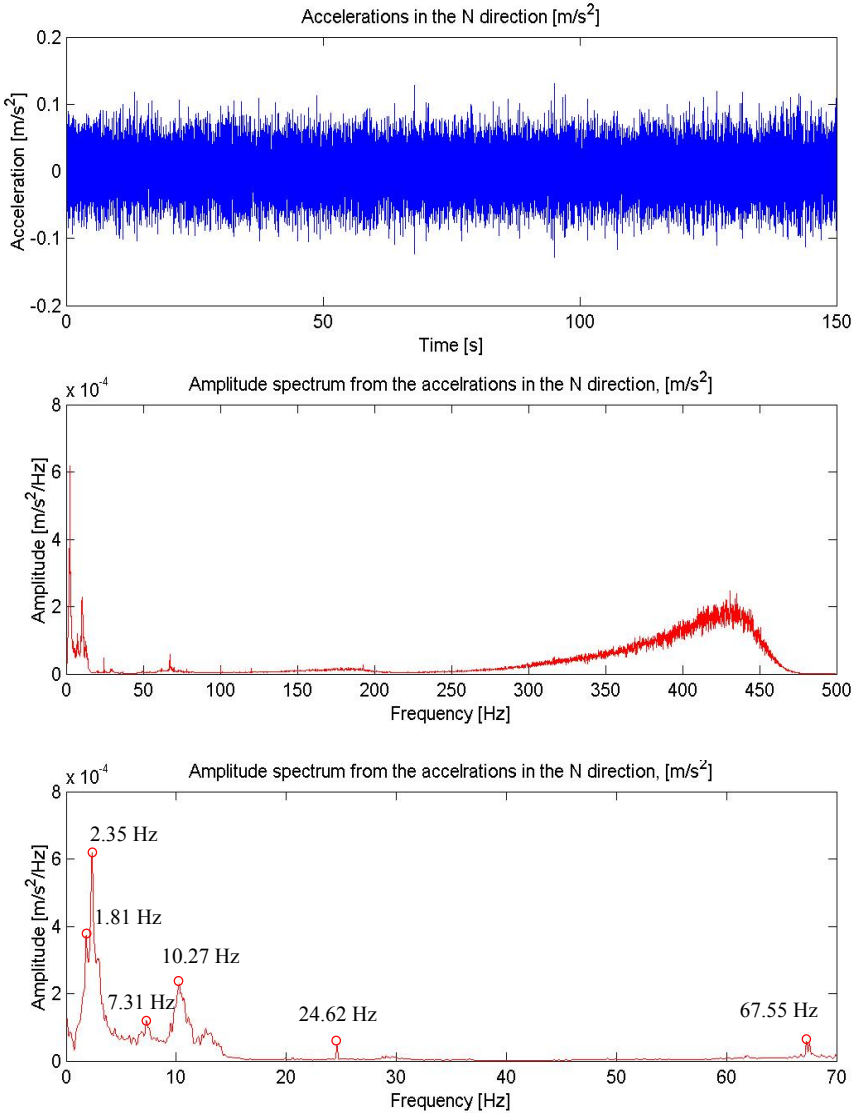


Figure 6-7: Horizontal (N direction) acceleration generated by the engine of the truck (upper curve) and the corresponding amplitude spectrum.

The amplitude spectrum of the N horizontal accelerations shows like for the vertical accelerations a large peak around 420 Hz. Below 100 Hz the three principal frequencies are also present.

Finally the E horizontal accelerations are presented, as well as their amplitude spectrum (Figure 6-8). Like for the two components Z and N described above, the 420 Hz peak is well visible as well as the three peaks at 3 Hz, 24.6 Hz and 67.5 Hz.

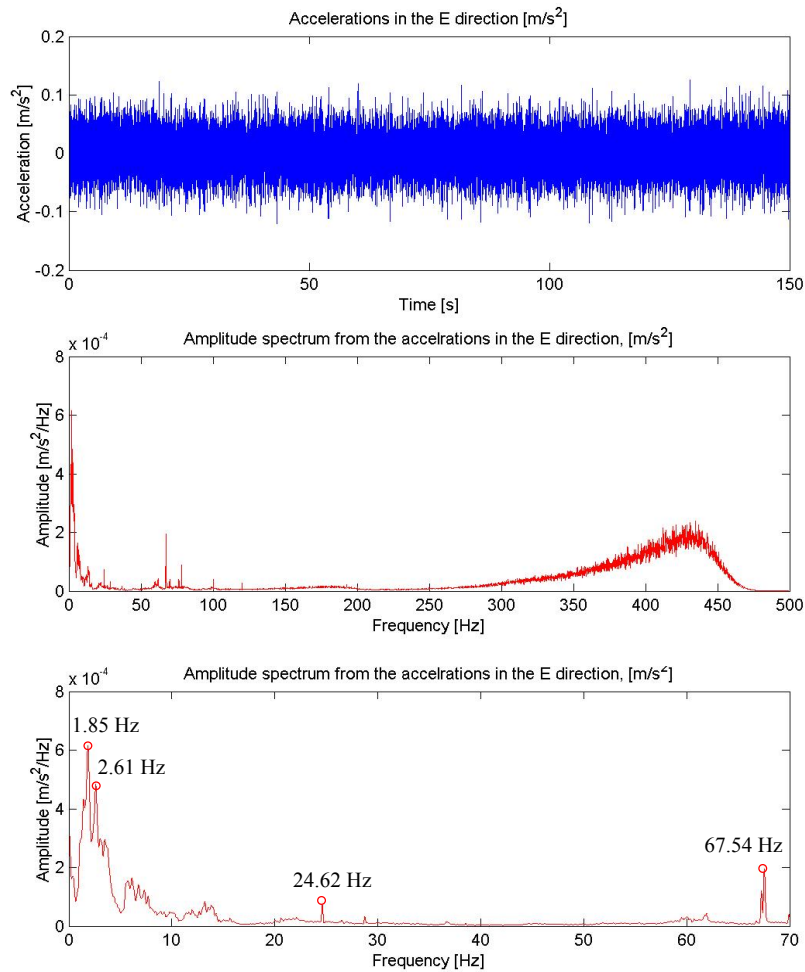


Figure 6-8: Horizontal (*E* direction) acceleration generated by the engine of the truck (upper curve) and the corresponding amplitude spectrum.

Based on the results of the vibration measurements it is possible to decompose the frequency domain in three regions. The first one extending between 100 Hz and 500 Hz contains the high frequencies, which should not have any influence on the quality of the determination of g .

Indeed we have seen in chapter 5.5.3 that the most part of the information contained in signal measured by the FG5-L is in the low frequencies. The second sector, between 10 Hz and 100 Hz contains some peaks well identified, which could be easily removed by means of the data of the external sensor (EpiSensor). The last part extending from 0 Hz to 10 Hz is the most problematic sector! First because these frequencies correspond to the domain where the information measured by the FG5-L is located. Moreover, these frequencies cannot be corrected by the method developed in laboratory (see chapter 1) because a fall during around 0.1 s, the lowest correctable frequency is 10 Hz. In order to be able to correct the lowest frequencies we then have to adopt another computing strategy, as we will see below.

The determination of g

In order to determine the g value we proceeded in two steps. In a first stage we have estimated the value of g for the 204 individual drops measured with the engine running taking into account the measurements of the Episensor. It gave us a value of g as function of time $g = g(t)$ corrupted by all the frequencies lower than 10 Hz. Figure 6-9 and Figure 6-10 show the vertical accelerations measured by the Episensor during this experience.

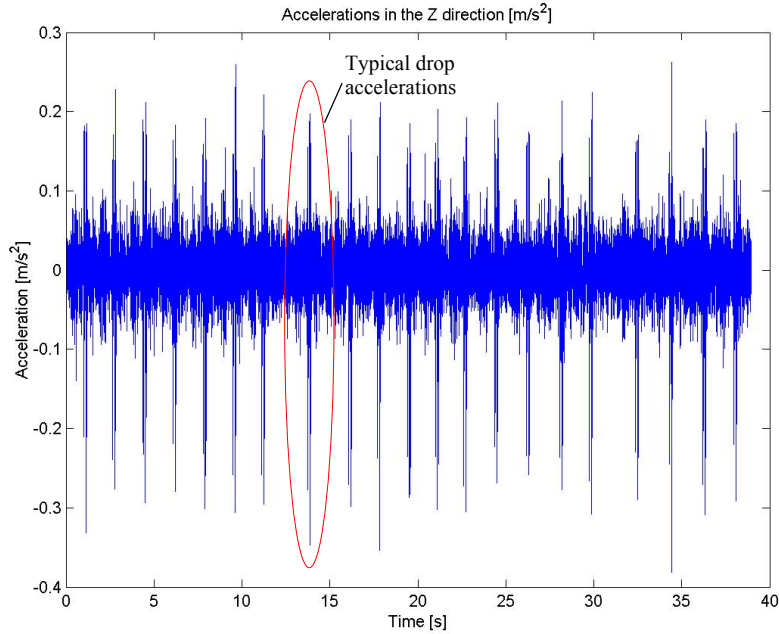


Figure 6-9: Vertical accelerations measured by the EpiSensor during the measurements of g . One can clearly see the peaks generated by the accelerations and deceleration of the drag-free chamber of the FG5-L. Both domains are more clearly visible on Figure 6-10.

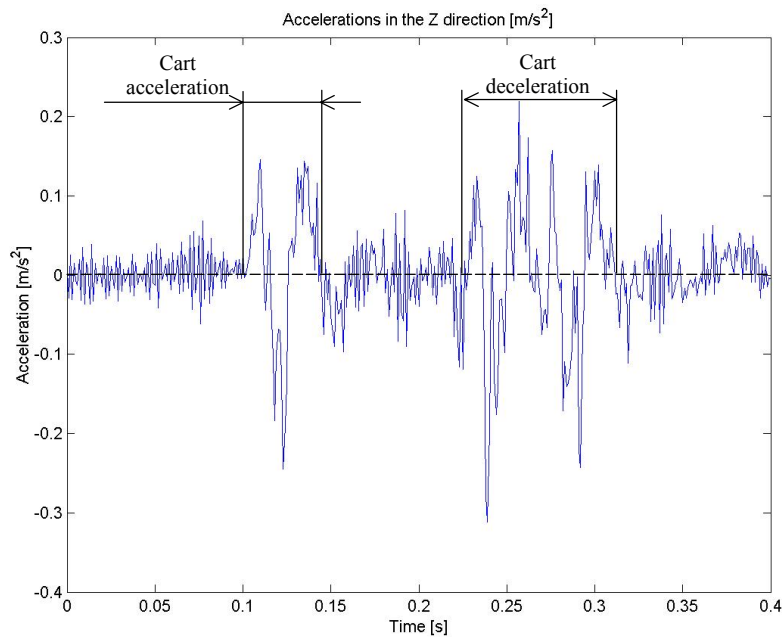


Figure 6-10: Vertical accelerations measured by the Episensor during a single fall. The two domains perturbed by the acceleration and deceleration of the drag-free chamber are easily identifiable.

First step

The physical model used in laboratory was:

$$z_i = \frac{1}{2}gt_i^2 + \dot{z}_0(t_i) + z_0 + \alpha_s F_s(t_i) \quad (6.1)$$

With:

z_i : Position of the prism at a time i

z_0 : Initial position of the prism

\dot{z}_0 : Initial velocity of the prism

g : Gravity

t_i : Time

α_s : Scaling factor

F_s : Measurements of the external sensor (Episensor)

The diagrams of Figure 6-11 show the residual obtained during the adjustment to the classical model (curve marked by \blacktriangle), it means without taking into account the Episensor measurements. The curve marked by \blacksquare , represents the residual obtained when the movements of the reference mirror (curve marked by \bullet) are taking into account.

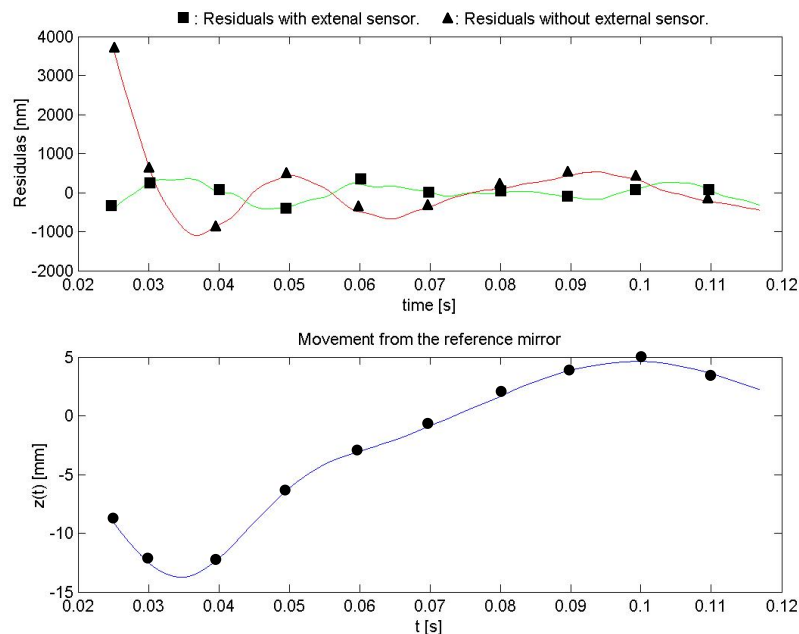


Figure 6-11: Residuals obtained by adjustment with the classical method (curve marked by \blacktriangle) and does by adjustment according to the equation (3.5) (curve marked by \blacksquare). The curve marked by \bullet represents the estimated movements of the reference's mirror.

By comparing the movements of the reference's mirror with the residuals obtained by adjustment with the classical method one can see that the correlation between the two signals is not as clear as in the laboratory (see chapter 1). Similarly the amplitudes of the residuals as well as the movements of the reference's mirror are larger than those obtained in the laboratory.

Figure 6-12 represents the amplitude spectra of the three functions depicted above. The amplitude spectrum of the residuals of the classical method shows two peaks at 10.9 Hz and a 43.6 Hz. It is worth noting that these frequencies are not part of the resonance frequencies determined during the static experiment.

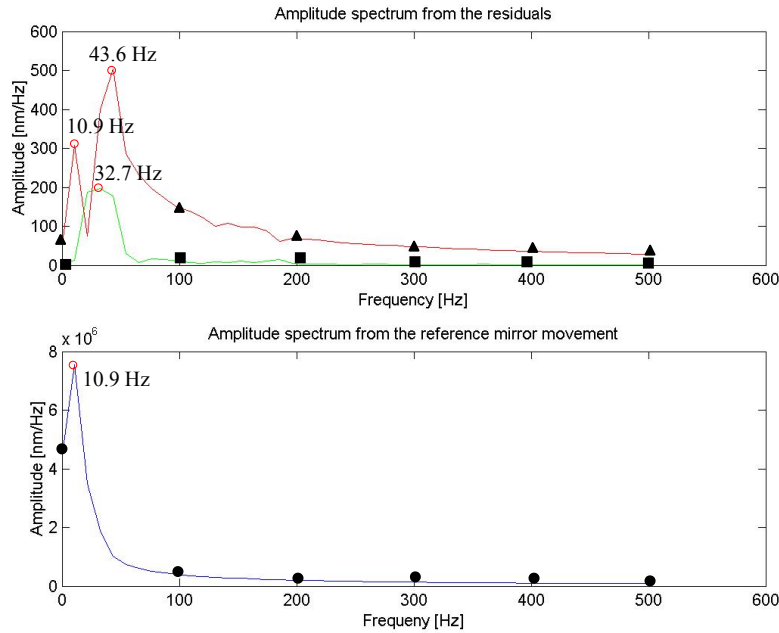


Figure 6-12: Amplitude spectrum of the function of Figure 6-11. Curve marked by ▲: Amplitude spectrum of the residuals obtained without the Episensor measurements. Curve marked by ■: Amplitude spectrum of the residuals obtained with the Episensor measurements. Curve marked by ●: Amplitude spectrum of the movements registered by the Episensor.

The analysis of the amplitude spectra of Figure 6-12 shows, however, a clear correlation between the classical residuals and the movements of the reference mirror at 10.9 Hz. One can also see that, even after corrections, the amplitude spectrum of the residuals, (green curve) still have a peak of large amplitude around 32 Hz.

A summary of the estimation obtained by using the estimation based on the physical model described by the equation (6.1) is presented in Table 6-1.

\bar{g} [mGal]	σ_g [mGal]	$\Delta g = g_{theo} - \bar{g} $	rms_{mean} [nm]	σ_{rms} [nm]
980642.48	283.94	0.79	145.9	47.3

Table 6-1: Summary of the estimation obtained by means of equation (6.1)

The difference between the values \bar{g} and g_{theo} is relatively small but σ_g is around 100 times higher than the desired resolution! It is therefore necessary to improve the method of computation as well as the physical model of adjustment.

We, therefore, developed an algorithm allowing to find the classic residuals in the movement measured by the Episensor, this in order to better synchronize the positions of the reference's mirror and of the falling prism.

Similarly we adapted the physical model by introducing 8 supplementary parameters allowing taking into account the four perturbations with maximal amplitudes.

The new model has the form:

$$z_i = \frac{1}{2}gt_i^2 + \dot{z}_0(t_i) + z_0 + \alpha_s F_s(t_i) + \sum_{j=1}^4 a_j \cos(2\pi f_j t_i) + b_j \sin(2\pi f_j t_i) \quad (6.2)$$

With:

z_i : Position of the prism at a time i

z_0 : Initial position of the prism

\dot{z}_0 : Initial velocity of the prism

g : Gravity

t_i : Time

α_s : Scaling factor

F_s : Measurements of the external sensor (Episensor)

$a_j \cos(2\pi f_j t_i) + b_j \sin(2\pi f_j t_i)$: j -th perturbation of frequency f_j

Figure 6-13 shows the classic residuals (\blacktriangle) and the residuals obtained by adjustment on the improved physical model (6.2) (\blacksquare). The lower curve (\bullet) corresponds to the part of the movement of the reference's mirror produced by the FG5-L itself.

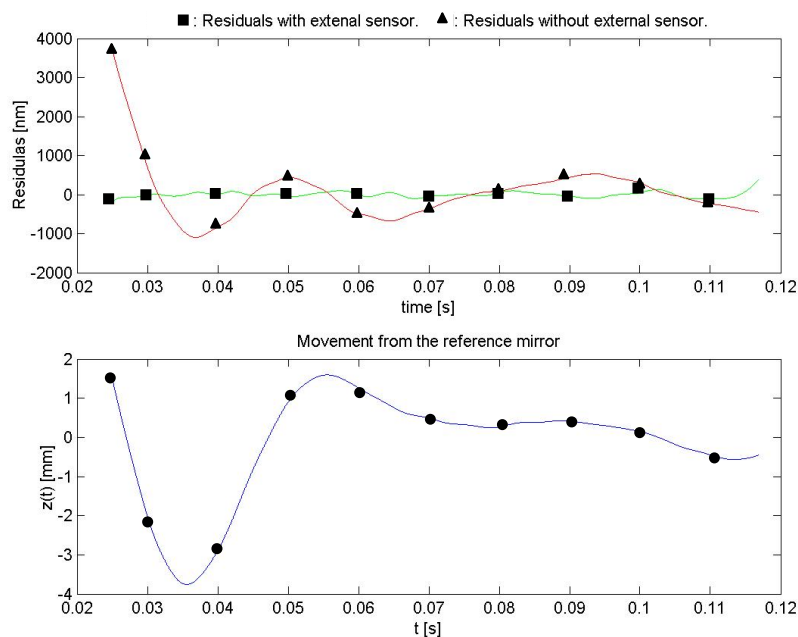


Figure 6-13: Comparison between the two methods of adjustment. The curve marked by \blacktriangle corresponds to the classic residuals and the curve marked by \blacksquare to the residuals obtained by adjustment on the improved physical model (6.2). The lower curve corresponds to the part of

the movement of the reference's mirror produced by the FG5-L itself. Looking at the curves of Figure 6-13, one can observe the strong correlation between the movement of the reference's mirror and the classical residuals. Similarly the residuals obtained after adjustment to model equation (6.2) show a clear improvement with regard to those obtained by means of equation (6.1).

Figure 6-14 shows the amplitude spectrum of the classical residuals (curve marked by ▲), the amplitude spectrum of the residuals obtained with equation (6.2) (curve marked by ■) and the amplitude spectrum of the movements of the reference's mirror (lower curve).

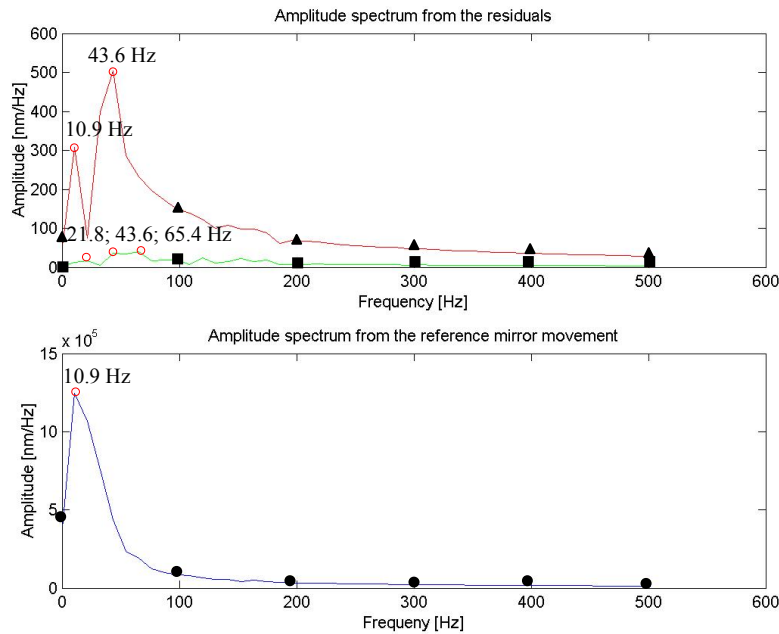


Figure 6-14: Comparison of the amplitude spectra obtained with the classical method and with equation (6.2). ▲ : Amplitude spectrum of the residuals computed without the Episensor data. ■ : Amplitude spectrum of the residuals obtained by means of the adjustment to equation (6.2). ● : Amplitude spectrum of the movement recorded by the Episensor.

The amplitude spectra of Figure 6-14 show a strong correlation between the movements of the reference's mirror and the classical residuals. It is remarkable to see that the amplitude spectrum of the residuals obtained by means of equation (6.2) is almost flat and that the peaks at 10.9 Hz and 43.6 Hz almost disappeared!

\bar{g} [mGal]	σ_g [mGal]	$\Delta g = g_{theo} - \bar{g} $	rms_{mean} [nm]	σ_{rms} [nm]
980643.99	221.98	0.75	13.51	1.92

Table 6-2: Summary of the results obtained by means of equation (6.2)

By comparing the results of Table 6-2 with those of Table 6-1 one can see that the modification of the physical model and to the synchronization' method produce a clear improvement of the rms_{mean} and of the σ_{rms} . The mean value \bar{g} is still in the same order of magnitude but the improvement of around 22% of σ_g .

Second step:

With the help of the new physical model we were able to determine $g = g(t)$, which still contains the perturbations of which the principal frequency is below 10 Hz. In this second step we will attempt to remove these perturbations by using the data acquired by the external accelerometer (EpiSensor).

Figure 6-15 shows the measurements that are inside a window of $\bar{g} \pm 2\sigma$. The threshold of $\pm n\sigma$ ($n=2$) has been adjusted in order to obtain the best correlation between $g(t)$ and $a(t)$. The mean estimated value of g , \bar{g} , is shifted of around 24 mGal from the true value $g_{theo.}$. This deviation with regard to the true value is clearly higher when all the drops are taken into account.

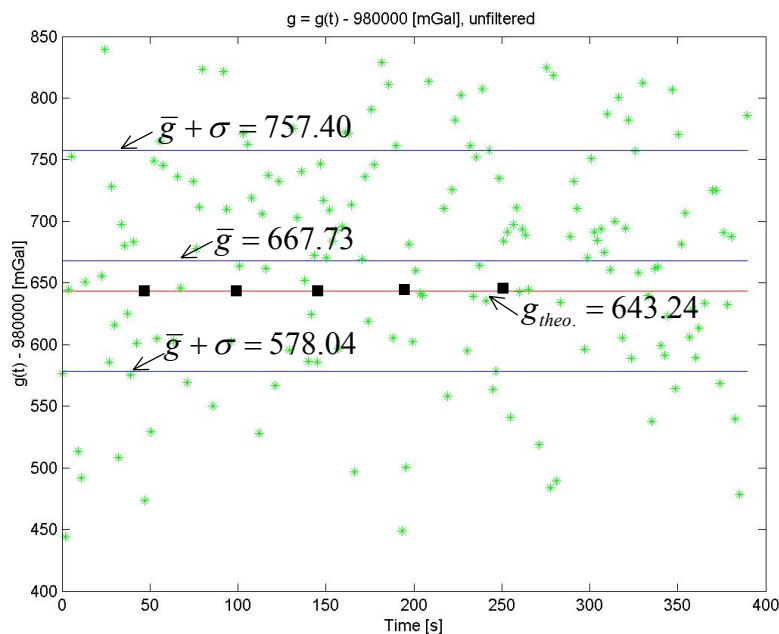


Figure 6-15: Distribution of the measurement with the threshold $\pm\sigma$. The dots are the estimated value of g for each single drop after the value without physical meaning have been removed. The central line represents the mean value, the upper and the lower lines represents $\bar{g} + \sigma$ and $\bar{g} - \sigma$ respectively with $\sigma = 89.76$ mGal. The line marked by ■, corresponds to the true value of g , $g_{theo.}$. All the values have been diminished of 980000 mGal.

The acceleration $a = a(t)$ measured by the EpiSensor, filtered with a lowpass filter with $f_c = 0.05$ Hz (lower curve) and the function $g(t)$ (upper curve) are presented together on Figure 6-16.

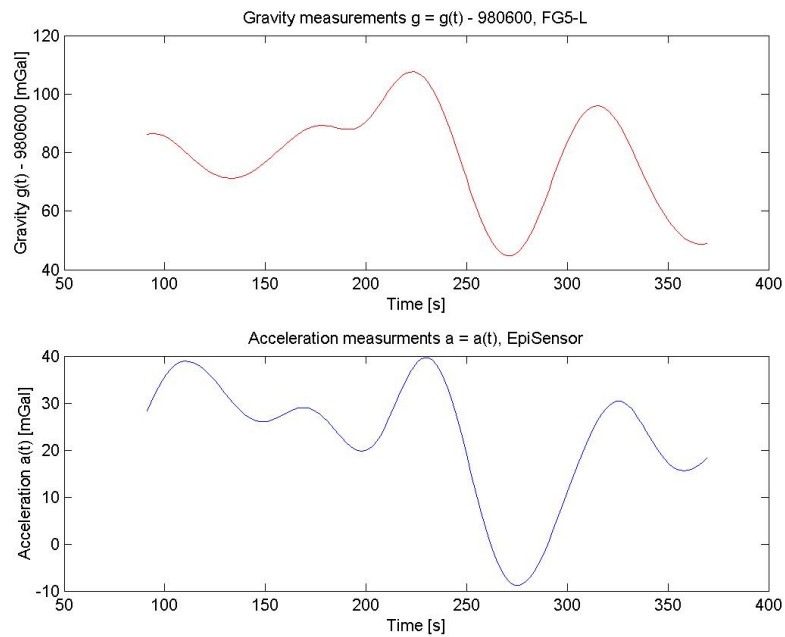


Figure 6-16: Comparison between the acceleration's function $g = g(t)$ (upper curve) and the accelerations $a = a(t)$ measured by the EpiSensor (lower curve)

The curves of Figure 6-16 show an almost perfect correlation between the measured g and the accelerations measured by the Episensor. Furthermore the function $a = a(t)$ is shifted of approximately 20 mGal with regard to the g function. This shift corresponds to that seen before (see Figure 6-15).

Finally after having optimized the synchronization of both signals, $g(t)$ is corrected by subtracting the function $\beta \cdot a(t - \tau)$, where τ and β are estimated by correlation

One then obtains:

$$\boxed{\bar{g} = 980641.063 \pm 3.47 \text{ [mGal]}}$$

$$\Delta g = 2.13 \text{ mGal}$$

Hypothesis test

With this test we will be able to define to which level of confidence the above results can be accepted.

Making the hypothesis that H_0 that the value of g is equal to $g_{theo} = 980643.242$ mGal with a level of significance, $\alpha = 0.01$.

From equation (5.19) we calculate that $Z_g = -0.63$ and from statistical tables (*Schaum Probabilités et statistique*) we obtain $Z_c = 2.58$.

In order that the hypothesis to be acceptable, Z_g has to satisfy the inequality (5.20). This the case because,

$$-2.58 < -0.63 < 2.58$$

Therefore we can accept the hypothesis and claim, with in 99% of confidence, that our measurement is correct.

Conclusions

The last experience has shown that even in a very noisy environment the experimental system is able to measure the absolute value of g with the expected resolution of 2 to 10 *mGal*. However the measured value shows a small offset, Δg , of approximately 2 *mGal*.

This difference could be introduced during the corrections of $g(t)$ by the measurement of the Episensor. In fact if the Episensor is not perfectly leveled the measured value of the vertical component contains contributions of the horizontal components, which cannot be measured with a vertical accelerometer. Using an IMU can solve this problem.

6.4.2 Measurement in dynamic mode

Until now the system was only tested in a stationary small truck. Now we will investigate the behavior of the system when the platform is in motion. For this we carried out measurements when the truck was moving along a straight line at a velocity of approximately 1 m/s . The whole experiment is formed of 251 single drops acquired at a frequency of 0.5 Hz .

In order to check the correct behavior of the system the first 100 drops were measured in stationary conditions. Figure 6-17 shows the vertical accelerations measured during the experiment.

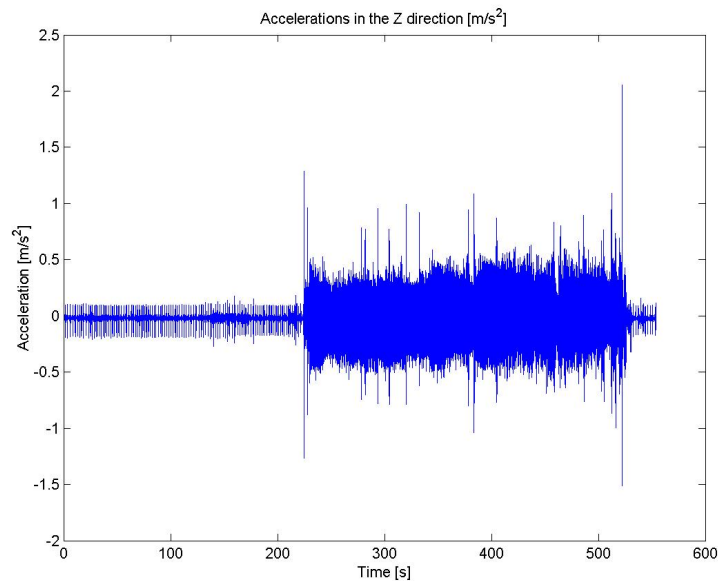


Figure 6-17: Vertical accelerations measured during the dynamic experiment. From 0 to 210 s the truck is stationary on the departure point, between 210 and 510 s the truck is moving along the measurement line and between 510 and 550 s the truck is again stationary but at the end point of the line

Figure 6-17 clearly shows the three phases of the experiment. In the first phase (0 to 210s) the accelerations produced by the drag-free chamber are clearly visible. The second phase (210 to 520 s) shows without ambiguity that the accelerations produced by the engine are much larger than those produced by the instrument. The third phase (520 to 550) is equivalent to the first one. For comparison and for putting in evidence the difficulties encountered during this experiment the accelerations measured during a single drop with and without movements are shown in Figure 6-18.

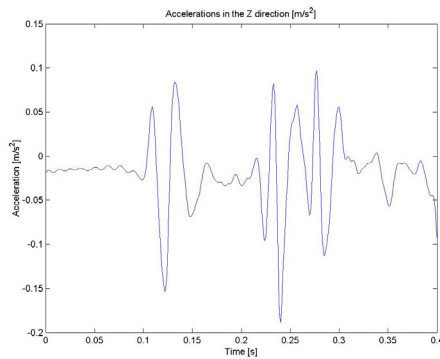


Figure 6-18.a: Drop 50

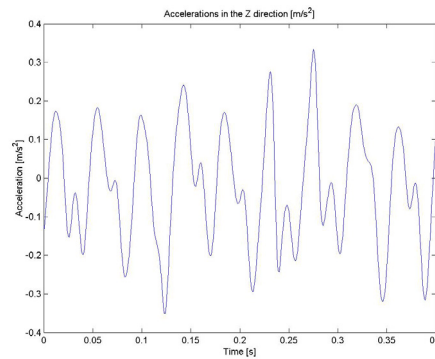


Figure 6-18.b: Drop 150

Figure 6-18: Comparison of the accelerations measured during a single drop in static (a) and in dynamic mode (b).

When the truck is located at the beginning of the line and the engine working with low rotation rate the measuring conditions are similar to those in the laboratory. On Figure 6-18.a it is possible to distinguish the three measuring zones: The acceleration of the drag-free chamber (0.1-0.15 s), the free-fall (0.15-0.23 s), and the deceleration (0.23-0.30 s). On the other hand when the truck is moving the conditions are extremely noisy and even during the period of free-fall the amplitudes of the perturbing accelerations are in the order of 0.2 m/s^2 .

The determination of g

The processing procedure for computing the g value is the same as described in chapter 6.4.1. In a first step we determine g for each single drop by adjustment on the model described by equation (6.2) then in a second step we correct the function $g = g(t)$ by correlation with the measurements of the Episensor $a = a(t)$, and by an adequate filtering.

First step:

Figure 6-19 shows, \blacktriangle , the residuals obtained without having taken into account the movement of the reference's mirror and these when movements are taken into account, \blacksquare . The lower curve shows the movements of the reference's mirror determined by the external sensor (EpiSensor).

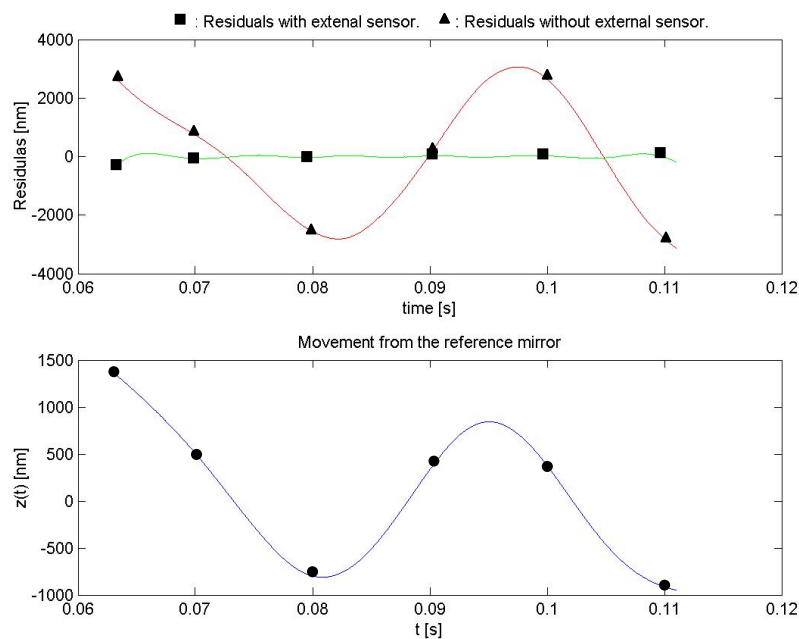


Figure 6-19: Results obtained from the first step of computation. \blacktriangle : residuals computed without the movements of the reference's mirror. \blacksquare : residuals computed with the movement of the reference's mirror. \bullet : movement of the reference's mirror determined by double integration of the signal measured by the external sensor (EpiSensor)

Like for the static measurements described in chapter 6.4.1 the movement of the reference's mirror is almost perfectly correlated with the residuals with the residuals computed without the movements of the mirror. By comparing the residuals obtained in static (Figure 6-13) with those obtained in dynamic mode (Figure 6-19), it is possible to see that both are of the same order of magnitude. Therefore the perturbing signals of frequencies higher than 10 Hz act on the reference's mirror in the same manner in dynamic mode as in static mode.

Figure 6-20 shows the amplitude spectrum of the residuals described above (Figure 6-19)

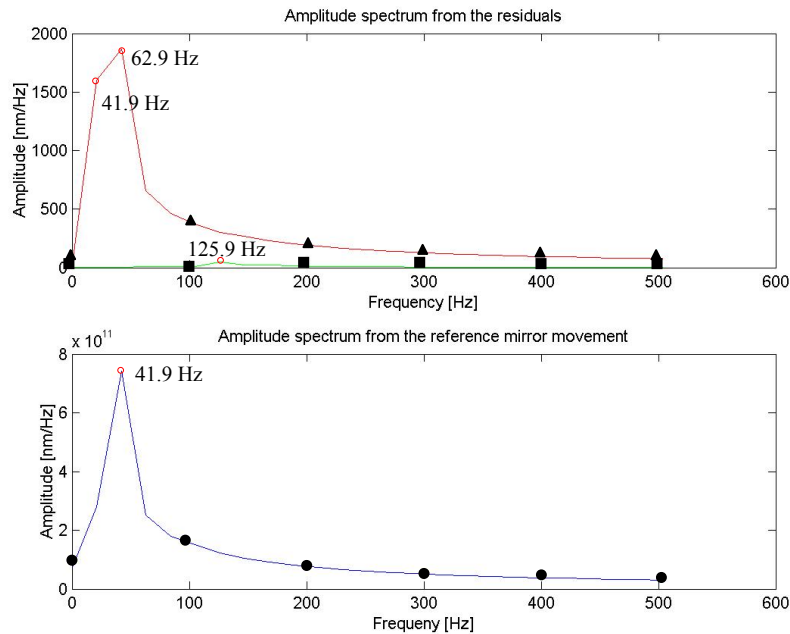


Figure 6-20: Amplitude spectrums of the residuals of Figure 1-19. ▲: Amplitude spectrum of the residuals obtained without the movement of the mirror. ■: Amplitude spectrum of the residuals obtained with the movement of the mirror. ●: Amplitude spectrum of the movement of the mirror

The peak around 40 Hz is present in both operating modes (static and dynamic). As already mentioned this perturbation is probably generated by the driving system of the drag-free chamber. On the other hand the 10 Hz peak visible in static mode is not present anymore in dynamic mode. This is due to the length of the estimation's windows, which is adjusted in such a manner that the *rms* is minimized, shorter in dynamic mode than in static mode. Consequently the lowest frequency we are able to correct in dynamic mode during the adjustment procedure is not 10 Hz but 20 Hz

The results obtained during the first stage of the estimation are summarized in Table 1-3

\bar{g} [mGal]	σ_g [mGal]	$\Delta g = g_{theo} - \bar{g} $	rms_{mean} [nm]	σ_{rms} [nm]
980371.65	445.18	271.55	35.84	26.34

Table 6-3: Summary of the results obtained during the first estimation stage.

A comparison between the data of Table 6-3 with those of Table 6-1 shows clearly that the results of the first stage of the dynamic experiment are not as good as those of the static experiment. The largest difference appears in the value of Δg . This difference let suppose that the measured g is the sum of the true g value and an almost constant acceleration. However the large value of σ_g call for a more careful analysis.

Second step:

Because we are now in a dynamic configuration similar to the one we will have in airborne mode we have to take into account the kinematic accelerations such as described in chapter 2.2. The truck running at a speed of around 1 m/s the kinematics acceleration are much lower than 1 *mGal* and therefore will have no influence on the measurements.

The correction's procedure is the same as that used before, during the static experiment.

In a first step we have estimated the validity's threshold of the computed g by optimizing the correlation between the two functions $g(\vec{x}(t))$ and $a(\vec{x}(t))$ shown in Figure 6-21.

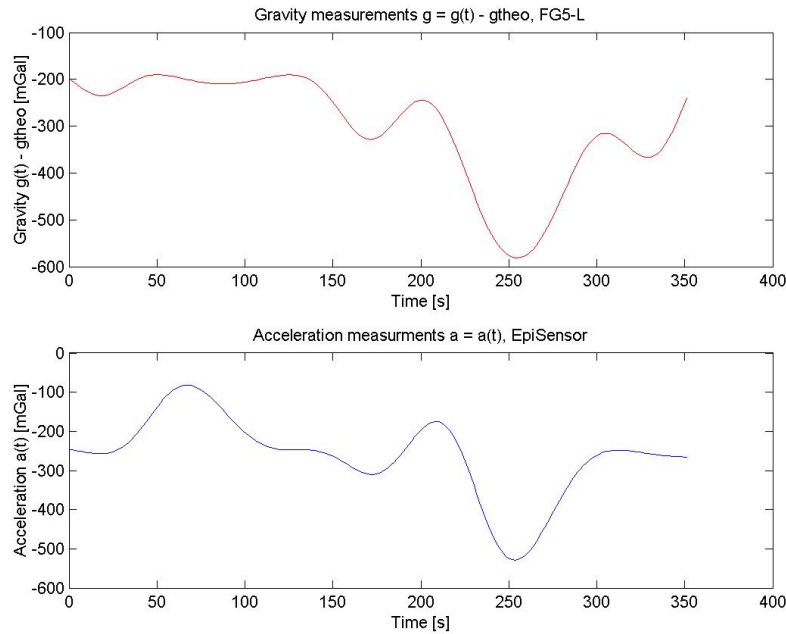


Figure 6-21: Result of the first step of the computation. Upper curve: Function $g(\vec{x}(t)) - g_{theo}$ obtained after the first step. Lower curve: Acceleration measured by the external sensor (EpiSensor)

In Figure 6-21, the upper curve represents the evolution of $g = g(\vec{x}(t))$, and the lower one the accelerations measured by the EpiSensor. Like in the static experiment it is possible to see a clear correlation between the two signals. This allows us to estimate the two adjustment factors τ and β and to correct the function $g(\vec{x}(t))$ by subtracting $\beta \cdot a(t - \tau)$. We then obtain:

$$\bar{g} = 980654.70 \pm 15.93 \text{ mGal}$$

$$\Delta g = 11.5 \text{ mGal}$$

Hypothesis test

In order to check this results we made the hypothesis H_o that the measured g is equal to $g_{theo} = 980643.242$ mGal with a level of significance of $\alpha = 0.01$.

From equation (5.19) we determine $Z_g = 0.72$ and from the statistical tables (*Schaum Probabilly and statistic*) we get $Z_c = 2.58$.

The hypothesis can be accepted Z_g satisfying the inequality (5.20).

$$-2.58 < 0.72 < 2.58$$

We concluded that our measurement is correct with in a level of confidence of 99 %.

Conclusions

The accuracy obtained during the second experiment is slightly lower than the one expected (11.5 mGal instead of 2-10 mGal). Like in the static mode the g value shows an offset Δg but much larger. This offset has probably the same origin: a bad leveling of the external accelerometer.

The leveling of the system was done before the beginning of the measurements, in a position perpendicular to the road on which the measurement line runs. Because the transversal slope of a road is around 3% the whole system was tilted by 2 degrees backward during the dynamic experiment. This had as a consequence a superposition of the N-accelerations on the vertical one. Another source of errors is the inability of the Episensor to correctly measure the low frequencies (inaccuracy in linearity, hysteresis in the control loop, etc.)

6.5 Measurements with the hanging table

In this experiment the FG5-L and the external accelerometer were both fastened on top of the basket of the hanging table (see Figure 6-2). This experience aimed of testing whether the measurements could be improved when the perturbing accelerations are filtered with a mechanical filter having a cut-off frequency of 1 Hz.

Figure 6-22 shows an example of the acceleration measured with this mounting.

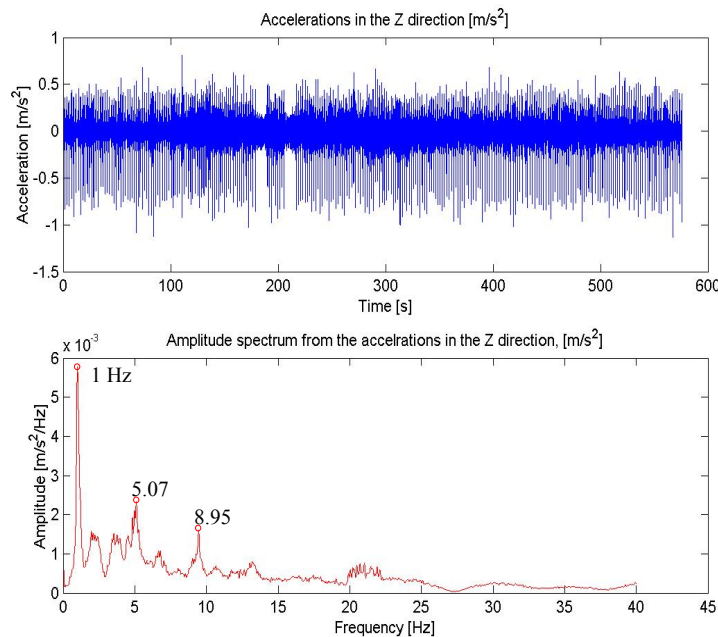


Figure 6-22: Example of accelerations measured at the top of the hanging table. Accelerations (upper curve) measured by the Episensor mounted on the hanging table and their amplitude spectrum (lower curve).

The amplitude spectrum of Figure 6-22 shows clearly a peak of resonance at 1 Hz corresponding to the cut-off frequency of the mechanical filter. The frequencies higher than 1 Hz are damped following the transfer function measured in chapter 4.5.

Figure 6-23 shows the accelerations measured during a single drop. Like in the strapped-down configuration three zones are visible: From 0.1 to 0.15 s corresponding to the acceleration of the drag-free chamber, from 0.15 to 0.22 s being the domain of a pure fall and from 0.2 to 0.28 s the decelerating phase of the drag-free chamber.

It is worth noting that during the pure fall time the mean acceleration is around 1000 *mGal* whereas in strapped configuration this acceleration is almost negligible. Important is also to remark that any constant acceleration superposed to *g* cannot be in any case estimated during the adjustment by least squares. This could have the consequence to completely shift the estimated value.

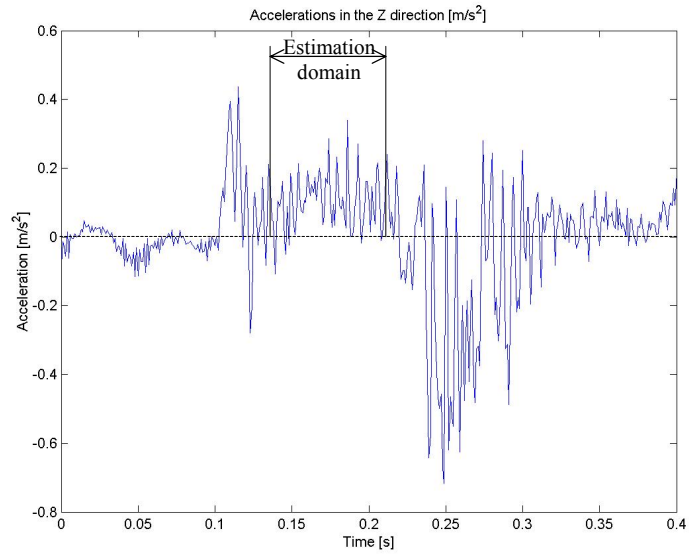


Figure 6-23: Accelerations measured by the FG5-L during a single fall.

The determination of g

Like in the strapped-down experiment we determined g in two steps. First we determined the g value for each of the 270 single drops by taking into account the estimation of the movements of the reference's mirror, then we tried to correct the obtained function $g(t)$ with the help of the accelerations measured by the external sensor.

First step:

Figure 6-24 shows the residuals obtained after the adjustment with the movements of the mirror being taken into account (\blacktriangle), the residuals obtained by adjustment on model described by equation (6.2) (\blacksquare) and the movement of the reference's mirror during the fall (\bullet).

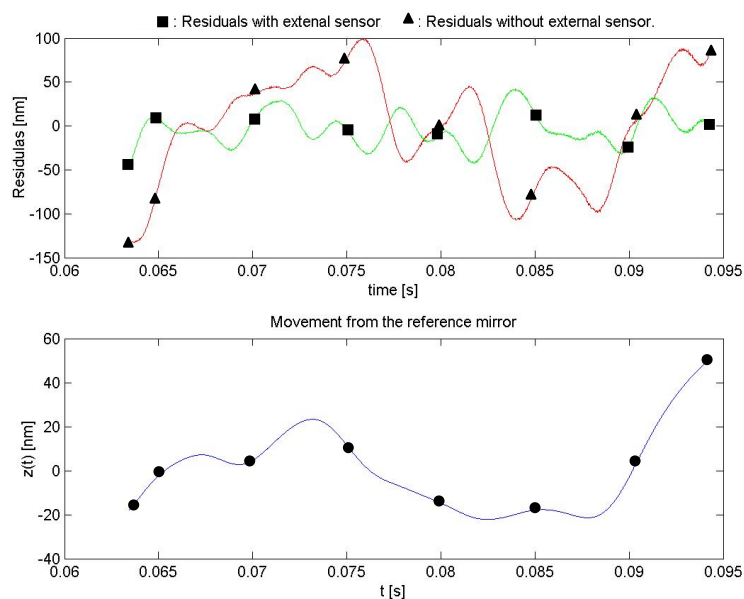


Figure 6-24: Comparison between the residuals obtained with (\blacksquare) and without (\blacktriangle) taking into account the movement of the reference mirror. \blacktriangle : Residuals obtained without taking into account the movements of the reference's mirror. \blacksquare : Residuals obtained with the movements of the reference's mirror. \bullet : movements of the mirror during the fall.

The amplitude spectra of the functions depicted in Figure 6-24 are shown in Figure 6-25.

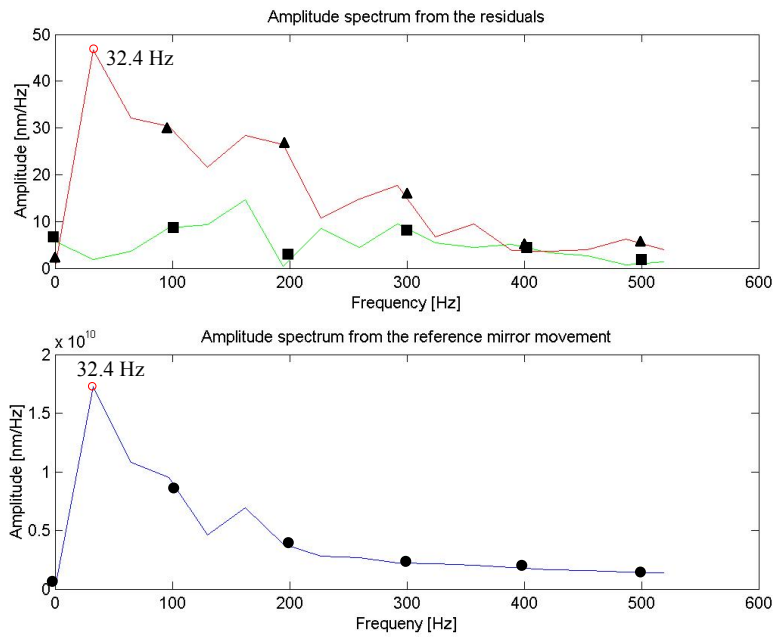


Figure 6-25: Amplitude spectrums of the functions of Figure 6-24 .The markers correspond to those defined in Figure 6-24.

The damping of the movements due to the mechanical filter is put in evidence by comparing the above residuals with those obtained in strapped-down configuration. The amplitudes of the residuals as well as those of the estimated movements of the mirror are clearly smaller than those obtained in strapped-down configuration. The results obtained after the first step of estimation are summarized in Table 6-4.

\bar{g} [mGal]	σ_g [mGal]	$\Delta g = g_{theo} - \bar{g} $	rms_{mean} [nm]	σ_{rms} [nm]
984000.30	575.28	3357.10	19.43	5.26

Table 6-4: Summary of the results obtained after the first step of estimation.

The results summarized in Table 6-4 confirm the hypothesis formulated previously that during the time of measurement the reference mirror undergoes an almost constant mean acceleration (see Figure 6-23). As already pointed out this acceleration cannot be separated from g . Consequently \bar{g} is shifted by more than 3000 $mGal$.

Second step

In this step, we tried like in the strapped-down experiment to correct the function $g(\vec{x}(t))$ with the help of the data acquired with the external sensor.

Figure 6-26 shows the functions $g(\vec{x}(t)) - g_{theo}$ in the upper graphic, and $a(\vec{x}(t))$ in the lower graphic.

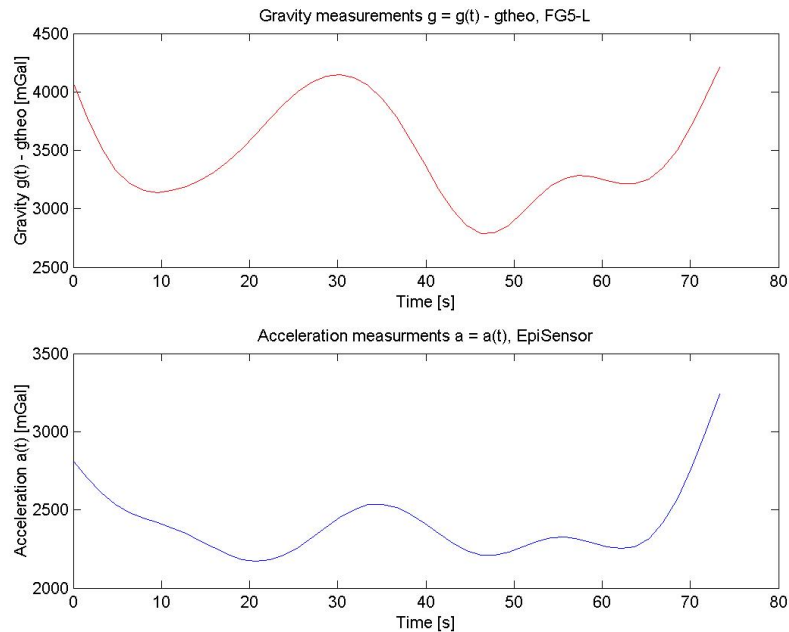


Figure 6-26: Function $g(\vec{x}(t)) - g_{theo}$ obtained after the first step (upper curve) and accelerations measured by the external accelerometer (lower curve).

The two functions $g(\vec{x}(t)) - g_{theo}$ and $a(\vec{x}(t))$ of Figure 6-26 show a quite good correlation but on the other hand even after the adjustment by correlation of $a(\vec{x}(t))$ on $g(\vec{x}(t))$ a difference of around 1000 *mGal* remains.

Finally and after complete correction we obtained:

$$\bar{g} = 981848.19 \pm 33.50 \text{ mGal}$$

$$\Delta g = 1204.99 \text{ mGal}$$

Hypothesis test

Again we tested the correctness of the obtained results. For this we made the hypothesis H_o that the measured value of g is equal to $g_{theo} = 980643.242 \text{ mGal}$ with a level of significance of $\alpha = 0.01$.

From the equation (5.19) we get $Z_g = 35.97$ and from the statistical tables $Z_c = 2.58$.

In order to get an acceptable hypothesis we have to fulfill the following inequality:

$$-2.58 < Z_g < 2.58$$

which is obviously not the case!

We then have to reject our hypothesis and can therefore claim that with a level of confidence of 99% that our measurement is not correct!

Conclusions

The hanging table allows to strongly attenuating the perturbing accelerations with frequencies higher than its cut-off frequency. However the accelerations and decelerations of the drag-free chamber of the FG5-L induce movements of the basket at its resonance frequency and consequently apply an almost constant mean acceleration on the reference mirror.

The only possibility to compensate for acceleration would be to use the data of the external sensor. However the leveling errors, the bad linearity of its transfer function and the unknown effect of the hysteresis do not allows correcting such important systematic errors like those produced by the oscillations of the hanging table

6.5.1 Discussion

Based on the results of this chapter we conclude that the experimental system behaves correctly in a noisy environment and also that the synchronization of the measurements by GPS works perfectly.

The results obtained with the hanging table are not as good as expected because we totally underestimated the effects of the accelerations and decelerations of the drag-free chamber. The mechanical filter is very efficient for damping acceleration with frequencies below the cut-off frequency from the filter. But the acceleration of the drag-free chamber are acting on the system like Dirac-pulses which are exciting the system in a broad range that includes the proper frequency of the filter. A solution would be to include in the FG5-L gravimeter a pseudo drag-free chamber moving synchronously with the real drag-free chamber but in opposite direction. Another solution would be to include a controlled damper that would block the hanging table during the acceleration and deceleration periods and would let it free during the pure free-fall.

The results obtained in strapped-down configuration are really promising. In static mode as well as in the dynamic one the accuracy of the results is close to the one expected. The small inaccuracies of the corrections seem to be produced by an insufficient leveling of the external sensor introducing a cross coupling effect which over or under-compensate $g(t)$.

7 The airborne test survey

7.1 Introduction

An airborne gravity survey consists on a double series of measurements carried out along straight parallel lines: one of the vertical accelerations and one of the trajectories of the aircraft. The planning of such a survey imposes choices like length and spacing of the lines, locations of the GPS reference stations.

In this chapter the principal characteristics of the test survey over the Rhone valley between Leuk and Martigny are described.

7.2 The aircraft

The survey was carried out with an the aircraft *De Havilland Twin Otter* (Figure 7-1, Figure 7-2) of the Swiss Federal Topographic Survey. It is equipped with a navigation system made of a receiver *GPS LORAN Trimble 200*, and of an automatic pilot *Collins*, type *AP 106*.

The principal technical data and performance of the aircraft are summarized in Table 7-1.

DeHavilland Twin Otter	
Engines	2 turbo-prop. GE/PT GA
Length	5.77 m
Wing span	19.81 m
Height	5.67 m
Empty weight	3350 kg
Max. load	2359 kg
Max. speed	335 km/h
Max. ascending speed	8 m/s
Full load max. altitude	8140 m
Take-off distance	366 m
Landing distance	320 m
Max. fuel load	1112 kg
Autonomy	5 h

Table 7-1: Technical data and performance of the *De Havilland Twin Otter*



Figure 7-1: The *DeHavilland Twin Otter* of the *Swiss Federal Topographic Survey*



Figure 7-2: The De Havilland Twin Otter at the airport of Dübendorf.

7.3 Location of the test survey

The test survey is formed of one line extending from Leuk to Martigny (Canton of Valais) flown four times twice in each direction, November 27, 2002. The length of this line is approximately 50 km, which gives a total length of the survey of 200 km. The nominal speed of the aircraft was 70 m/s and the flight altitude 2500 m a.s.l.

The location of the test line is shown in figure Figure 7-3.



Figure 7-3: Location of the test line flown, November 27, 2002

A copy of the flight log is shown in Table 7-2

Line	Date	Direction	Beginning time	End time
Line 01	27.11.02	Leuk - Martigny	14.15.00	14.22.30
Line 02	27.11.02	Martigny - Leuk	14.25.00	14.38.00
Line 03	27.11.02	Leuk - Martigny	14.42.00	14.53.00
Line 04	27.11.02	Martigny - Leuk	14.55.00	15.07.00

Table 7-2: Copy of the flight log of November 27, 2002.

7.4 The positioning of the aircraft

Principle

The exact positioning of the aircraft in a terrestrial reference frame is of at most importance in airborne gravimetry. Apart of the localization of the measurements in space, the trajectory data are used for determining the accelerations induced by the movements of the aircraft.

The GPS system allows the determination of the relative distance between two or more points in any location on the Earth surface or in the near space. This mode of positioning is called « differential positioning » it can also be applied for a moving platform, in this case it is called « *Kinematic Differential GPS mode* ». The distance between the aircraft and a ground station can be deduced from the simultaneous measurements of the pseudo-distances and the phase of the carrier waves L1 et L2 on the ground and in the aircraft.

The result of the data processing gives the coordinates of the vector joining the ground station to the antenna of the aircraft. This method of positioning reduces the errors induced by the orbit inaccuracies and the shift between the clocks of the satellites and the receivers, (*Botton et al., 1997*). Commonly used in geodesy the differential phase positioning can reach a precision of millimeters.

The ground reference station

The accuracy of the positioning depends directly on the length of the base line, the distance between the ground station and the aircraft. In order to have a base line as short as possible we used the data of the AGNES station Jungfrauoch (see Figure 7-4)



Figure 7-4: Location of the AGNES station Jungfrauoch

The reference station acquired data at the sampling rate of 2 seconds during the whole survey: From 15 :00 until 17 :00 the coordinates of this station, continuously adjusted by Federal Office of Topography are summarized in Table 7-3.

Station	Coordonnées géocentriques		
	X (m)	Y (m)	Z (m)
Jungfrauoch	4354213.261	610774.737	4609950.790

Table 7-3: Coordinates of the AGNES station Jungfrauoch

The onboard GPS receivers

In order to determine the full movement of the aircraft (pitch, roll, yaw, and position) the aircraft was equipped with five GPS antennas connected to five receivers working at high sampling rate (see Table 7-4). Two antennas were located on the wings, two on the roof of the cabin and one on the tail (Figure 7-5).



Figure 7-5: Locations of the *GPS* antennas on the aircraft. **1** : Front antenna (frnt), **2** : Wings antennas (left, rgth), **3** : Roof antenna, **4** : Tail antenna (tail)

Receivers		Collected signals	Frequency
Ground station		Codes C/A P on L1 and L2 Phase on L1 and L2	1 Hz
Aircraft antennas array	Wing	Code and phase on L1	2 Hz
	Head	Code and phase on L1 et L2	2 Hz
	Tail	Code and phase on L1	2 Hz
	Roof	Code and phase on L1 et L2	-

Table 7-4: Summary of the characteristics of the GPS receivers

The INS

In addition to the GPS receivers an INS (*INS, Inertial Navigation System*) was installed in the aircraft as a supplementary system for determining the attitude of the aircraft and also the instantaneous accelerations. The INS was chosen because it continuously gives the rotation matrix of the aircraft on which it is mounted.

7.5 Experimental mounting and measurements

To the opposite of a relative gravity system an absolute system does not need to be tied to a reference point. A measurement line can start anywhere and at any time without any constraints. Because the absolute system is not mounted on a gyro-stabilized platform a stabilization distance (normally about 20 km long) is not necessary, the data acquisition can start directly at the beginning of the measurement line. The experimental mounting as well as the synchronization system was the same as used during the truck experiment with in addition the INS. The steering and data acquisition system of the INS was connected to an independent GPS receiver allowing a perfect synchronization of its data with those of the gravimeter.



Figure 7-6: View of the interior of the aircraft during the test survey. **1** : Gravimeter FG5-L, **2** : Data acquisition system of the EpiSensor, **3** : Rack containing the GPS receivers and the PCs, **4** : Navigation system for photogrammetry, **5** : INS (Inertial Navigation System), **6** : Steering and data acquisition system of the l'INS.

During the flight the aircraft flies with a constant pitch of 3° . In order to compensate this angle as well as the variations of pitch and roll higher than 5 degrees all the sensors were mounted on a table leveled manually. This table was made of three aluminum honeycomb plates stuck together.

7.6 Data acquisition during the flight

As soon as the aircraft is on the line in a stabilized flight the measurements are started manually and continue automatically. The sampling rates of the different instruments are summarized in Table 7-5.

Instruments	Signals	Units	Sampling rate
FG5-L	Position as function of time $z = z(t)$	m, s	1 s
Episensor	Accelerations $\ddot{x}(t), \ddot{y}(t), \ddot{z}(t)$	m/s ²	0.001 s
INS	Accelerations $\ddot{x}(t), \ddot{y}(t), \ddot{z}(t)$ Angular velocity $\dot{\omega}_x(t), \dot{\omega}_y(t), \dot{\omega}_z(t)$	m/s ² rad./s	0.0025 s

Table 7-5: Signal acquired by the instruments.

At the end of the line the measurements are stopped manually. The acquisition of the GPS data is started immediately after take-off and stopped just before landing in order to ensure a complete coverage of the gravity measurements.

8 Processing of the airborne gravity data

8.1 Processing of the GPS data.

A GPS receiver acquires two types of data: The phase measurements and the pseudo-distance measurements. A phase measurement consists of determining the phase difference between the signal emitted by the satellite and its replica generated by the receiver. This phase shift is related to the distance between the satellite and the receiver through an observation's equation. A pseudo-distance consists in catching the pseudo-random codes *C/A* or *P* emitted by the satellite. The receiver generates a replica of the codes by means of the same algorithm used in the satellite and compares these two signals by correlation. This comparison allows the determination of the time difference between the satellite and the receiver and consequently the distance between them.

8.1.1 Single difference equation of observation

The equations of the observed signals, which link the phase and the pseudo-distance measurements to the physical distance between the satellite, *i* and the receiver *j* (Cocard, 1995, Klingelé et al., 1996) can be written:

For the pseudo-distance

$$\begin{aligned} \rho_j^i(t_R) &= d_j^i + c.cl_j - c.cl^i + Ion_j^i + Trp_j^i \\ &= \|\vec{R}^i(t_T) - \vec{r}_j(t_R)\| + clBias_j - clBias^i + Ion_j^i + Trp_j^i \end{aligned} \quad (8.1)$$

For the phase:

$$\begin{aligned} \phi_j^i(t_R) &= d_j^i + c.cl_j - c.cl^i + Ion_j^i + Trp_j^i \\ &= \|\vec{R}^i(t_T) - \vec{r}_j(t_R)\| + clBias_j - clBias^i - \lambda.A^i + Ion_j^i + Trp_j^i \end{aligned} \quad (8.2)$$

where :

t_R : Measurement's time at the receiver, in GPS time

t_T : Emission's time, in GPS time

c : Speed of light in vacuum (299793 km/s)

$\vec{R}^i(t_T)$: Position's vector of the satellite *i*

$\vec{r}_j(t_R)$: Position's vector of the receiver *j*

d_j^i : Unknown distance between the satellite *i* and the receiver *j*

$clBias_j = c.cl_j$: Unknown time shift of the receiver *j*, measured in en meters

$clBias^i = c.cl^i$: Unknown time shift of the satellite's clock *i*, measured in meters

A^i : Phase's ambiguity, with respect to the satellite *i*

Ion_j^i : Delay introduced by the ionosphere

Trp_j^i : Delay introduced by the troposphere

λ : Wavelength of the signal

The simple difference measurements are obtained by subtracting the simultaneous observations of two different receivers working with the same satellite.

Consider a mobile receiver located in an aircraft and a ground permanent receiver f , receiving both the signal emitted by the satellite s . The simple difference equations for the phase and the pseudo-distance measurements are given by:

$$\begin{aligned}\Delta\rho_{mf}^s &= \rho_m^s(t_{Rm}) - \rho_f^s(t_{Rf}) \\ &= \Delta d_{mf}^s + \Delta clBias_{mf} - \Delta clBias_{mf}^s + \Delta Ion_{mf}^s + \Delta Trp_{mf}^s\end{aligned}\quad (8.3)$$

$$\begin{aligned}\Delta\varphi_{mf}^s &= \varphi_m^s(t_{Rm}) - \varphi_f^s(t_{Rf}) \\ &= \Delta d_{mf}^s + \Delta clBias_{mf} - \Delta clBias_{mf}^s - \lambda\Delta A_{mf}^s + \Delta Ion_{mf}^s + \Delta Trp_{mf}^s\end{aligned}\quad (8.4)$$

with

$$\Delta d_{mf}^s = \left\| \vec{R}^s(t_{Tm}) - \vec{r}_m(t_{Rm}) \right\| - \left\| \vec{R}^s(t_{Tf}) - \vec{r}_f(t_{Rf}) \right\|$$

$$\begin{aligned}\Delta clBias_{mf} &= clBias_m(t_{Rm}) - clBias_f(t_{Rf}) \\ &= c.(cl_m(t_{Rm}) - cl_f(t_{Rf}))\end{aligned}$$

$$\begin{aligned}\Delta clBias_{mf}^s &= clBias_m^s(t_{Rm}) - clBias_f^s(t_{Rf}) \\ &= c.(cl_m^s(t_{Rm}) - cl_f^s(t_{Rf}))\end{aligned}$$

$$\Delta A_{mf}^s = A_m^s - A_f^s$$

$$\Delta Ion_{mf}^s = Ion_m^s - Ion_f^s$$

$$\Delta Trp_{mf}^s = Trp_m^s - Trp_f^s$$

This combination minimizes the differential bias $\Delta clBias_{mf}^s$, due to the time shift of the satellite's clock. The atomic clocks of the *GPS* satellite have a very high time stability of

$\frac{dcl^s}{dt} \approx 10^{-10}$. In the first order the bias $\Delta clBias_{mf}^s$ is given by:

$$\Delta clBias_{mf}^s = c \cdot \frac{dcl^s}{dt} \cdot (t_{Rm} - t_{Rf})$$

A synchronization difference of the receivers of one second then induces a bias of 3 *mm*, which can be considered as acceptable considering the length of the base line in aerogravimetry (several kilometers).

The coordinates of the vector \vec{R}^s are computed by means of accurate ephemeris of the satellite and previous computed coordinates of the ground station.

The differential delays, ΔIon_{mf}^s and ΔTrp_{mf}^s , are estimated with the help of models of the atmosphere. The only unknowns in the simple difference equations are then:

- The coordinate (x_m, y_m, z_m) of the antennas on the aircraft
- The differential bias $\Delta clBias_{mf}^s$
- The ambiguity ΔA_{mf}^s , only present in the phase measurements

In order to determine these variables it is necessary to solve a system of equations of simple difference formed by (8.3) and (8.4) written for several satellites. A such system can be written:

$$\Delta \rho_{mf}^i = C(\bar{X}^i)$$

$$\Delta \phi_{mf}^i = P(\bar{X}^i)$$

$$i = 1, 2, \dots, p$$

where $\bar{X}^i = [x_m, y_m, z_m, \Delta clBias_{mf}^s, \Delta A_{mf}^s]^T$ is the vector of the unknown variables and p is the number of observed satellites.

This non-linear system can be linearized under the form:

$$\Delta \rho_{mf}^i \approx C(\bar{X}_o^i) + \sum_j a_j^c dX_j^i$$

$$\Delta \phi_{mf}^i \approx P(\bar{X}_o^i) + \sum_j a_j^p dX_j^i$$

$$i = 1, 2, \dots, p$$

Where \bar{X}_o^i is an approximation of the unknown vector, and the set of a_j^c, a_j^p correspond to the linearization's coefficients of the pseudo-distance and phase measurements. The system is then solved by means of least squares. The linearization's coefficients are summarized in Table 8-1.

Coefficients	x_m	y_m	z_m	$\Delta clBias_{mf}^s$	ΔA_{mf}^s
a_j^c	e_x^i	e_y^i	e_z^i	1	0
a_j^p	e_x^i	e_y^i	e_z^i	1	λ

Table 8-1: Table of the linearization's coefficients. The e_x^i, e_y^i, e_z^i are the coordinates of the

unit vector $\frac{\bar{R}^i(t_{Tm}) - \bar{r}_m(t_{Rm})}{\|\bar{R}^i(t_{Tm}) - \bar{r}_m(t_{Rm})\|}$.

8.1.2 Strategy for the GPS data processing in kinematics mode

The recorded *GPS* signals are normally put together in epoch, which for static measurements group together the measurements collected during 30 s. In dynamic mode each epoch is very short, therefore, most of the variables differ from one epoch to the other.

Thus among the variables to be determined the coordinates of the rover receiver and the bias vary during the time. Only the phase ambiguities can be stay constant for several epoch. The basic idea for the processing of kinematics *GPS* data is to determine the time varying variables and the constant one separately (Cocard, 1995).

The values of the ambiguities are obtained in a first step after elimination of the time varying variables from the normal equations. Then these values, integer or real, are used for computing the time depending variables particularly the coordinates of the rover receiver. The advantage of this procedure is that it uses the entire set of the kinematics measurements, before and after the computed point, for the estimation of the ambiguities. In order to ensure a good quality of the used data a systematic detection of the cycle slip is applied prior to the computation. A *GPS* processing software using this kind of strategy has been developed at the *ETH* Zurich, and applied with success for the airborne gravity survey of Switzerland (Klingelé et al. 1997). The whole *GPS* data of the test survey were processed with this software.

The diagrams of Figure 8-1 show some results obtained by *GPS* processing. One can see that the mean flight altitude is 2523 m a.s.l. and also that the vertical acceleration computed by double derivation of the vertical positions can reach several thousands of *mGal*.

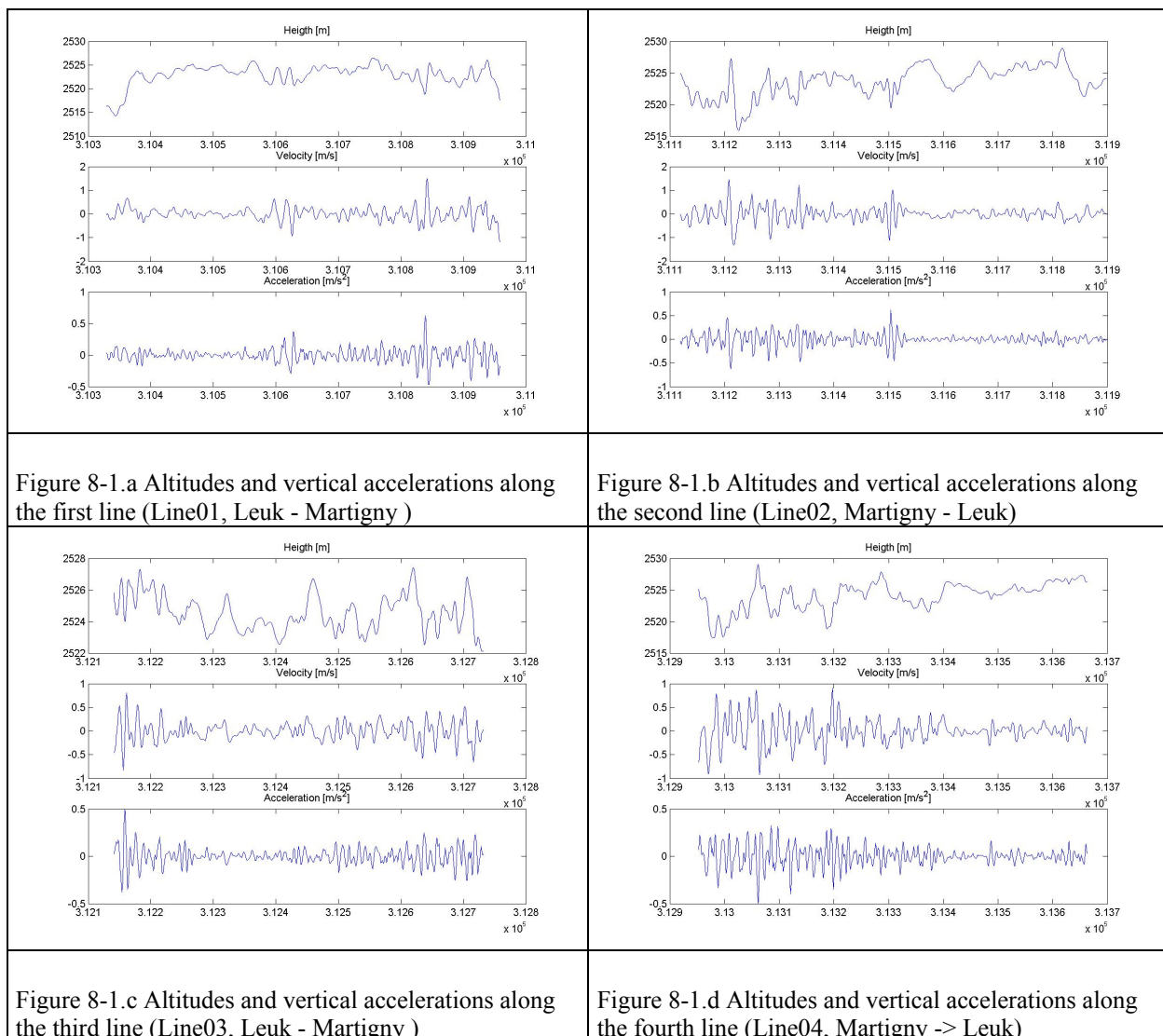


Figure 8-1.a-d: Graphical representation of some results from *GPS* data processing. By comparison on can see that the flight condition are more less the same for each flowed line.

With the *GPS* data we determined all the flight parameters, $(h, \varphi, \alpha, V_h)$, which were used, directly or indirectly, for the estimation of the kinematics accelerations useful for correcting the gravity measurements as described in chapter 2.2. In order to estimate the accuracy of the gravity measurements it is necessary to know to which accuracy the flight parameters can be estimated.

8.1.3 Accuracy of the kinematics variables computed with GPS data

As shown in chapter 2.2.5 the value of gravity is computed by means of the equation

$$g(p) = P_{\text{apparent}} + E(p) - \ddot{h} \quad (8.5)$$

where P_{apparent} corresponds to the apparent gravity measured by the gravimeter, E to the Eötvös acceleration and \ddot{h} to the vertical acceleration of the platform.

The accuracy of g then depends directly on the quality of the determination of the kinematics accelerations, which are computed from the flight parameters and their derivatives. The kinematic accelerations act directly on the reference's mirror. In order to be able to compute the precision of these accelerations it is necessary to write the equation of movement of the mirror.

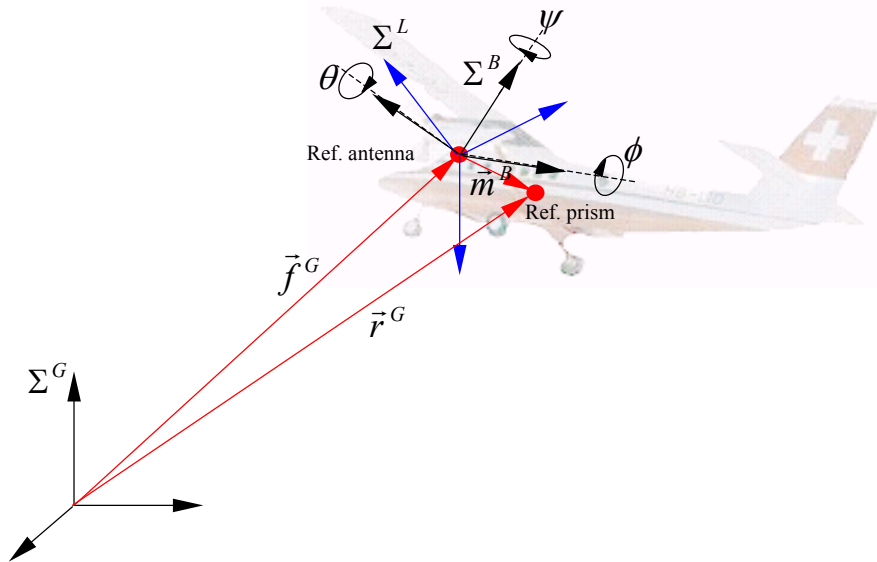


Figure 8-2: Measurement principle of the position of the FG5-L reference's mirror. Σ^G is the geocentric referential, Σ^L the local referential and Σ^B the aircraft referential. \vec{f}^G is the position's vector of the reference antenna in the geocentric referential, \vec{r}^G is the position's vector of the mirror in the geocentric referential, \vec{m}^B is the position's vector of the mirror with respect to the reference's antenna.

In the geocentric referential R_G the equation of movement of the reference's mirror can be written:

$$\vec{r}^G = \vec{f}^G + R_L^G R_B^L \vec{m}^B \quad (8.6)$$

With :

\vec{r}^G : Position's vector of the reference's mirror in the geocentric referential

\vec{f}^G : Position's vector of the reference's antenna in the geocentric referential

\vec{m}^B : Position's vector of the reference's mirror with respect to the reference's antenna in the aircraft referential

R_L^G : Rotation's matrix between the local referential Σ^L and the geocentric referential Σ^G

R_B^L : Rotation's matrix between the aircraft referential Σ^B and the local referential Σ^L

A rotation's matrix R can be decomposed into three elementary rotations around each of the three Cartesian axes

$$R = R_3(\alpha_3) R_2(\alpha_2) R_1(\alpha_1)$$

with

$$R_1 = \begin{bmatrix} 1 & 0 & 0 \\ 0 & \cos(\alpha_1) & \sin(\alpha_1) \\ 0 & -\sin(\alpha_1) & \cos(\alpha_1) \end{bmatrix}, R_2 = \begin{bmatrix} \cos(\alpha_2) & 0 & -\sin(\alpha_2) \\ 0 & 1 & 0 \\ \sin(\alpha_2) & 0 & \cos(\alpha_2) \end{bmatrix}, R_3 = \begin{bmatrix} \cos(\alpha_3) & \sin(\alpha_3) & 0 \\ -\sin(\alpha_3) & \cos(\alpha_3) & 0 \\ 0 & 0 & 1 \end{bmatrix}$$

One can set for the rotation's matrix R_L^G :

$$R_L^G = R_3(-\lambda) \cdot R_2(\varphi - \frac{\pi}{2}) \quad (8.7)$$

with λ = longitude and φ = latitude.

Similarly

$$R_B^L = R_3(-\psi) \cdot R_2(-\theta) \cdot R_1(-\phi) \quad (8.8)$$

with ϕ = roll angle, θ = pitch angle and ψ yaw angle.

Error propagation:

Transforming the equation of movement (8.6) in the local referential and then differentiating one obtains:

$$d\vec{r}^L = \frac{\partial(R_G^L \vec{f}^G)}{\partial \vec{\xi}} d\vec{\xi} + \frac{\partial(R_G^L \vec{f}^G)}{\partial \vec{f}^G} d\vec{f}^G + \frac{\partial(R_B^L \vec{m}^B)}{\partial \vec{\chi}} d\vec{\chi} + \frac{\partial(R_B^L \vec{m}^B)}{\partial \vec{m}^B} d\vec{m}^B \quad (8.9)$$

where $\partial \vec{\xi}$ is the derivative with respect to the angles $\vec{\xi}^T = (\varphi, \lambda)$ and $\partial \vec{\chi}$ the derivative with respect to the attitude angle $\vec{\chi}^T = (\phi, \theta, \psi)$.

In order to be able to calculate the partial derivative $\frac{\partial(R\vec{k})}{\partial\vec{\alpha}}$ we made the following approximation:

For small angles of rotation ($\vec{\alpha} \rightarrow d\vec{\alpha}$) the elementary rotation's matrix R_1, R_2, R_3 can be linearized and became

$$R_i \approx (I + I_i \cdot d\alpha_i)$$

$$\text{with } I_1 = \begin{bmatrix} 0 & 0 & 0 \\ 0 & 0 & 1 \\ 0 & -1 & 0 \end{bmatrix}, I_2 = \begin{bmatrix} 0 & 0 & -1 \\ 0 & 0 & 0 \\ 1 & 0 & 0 \end{bmatrix}, I_3 = \begin{bmatrix} 0 & 1 & 0 \\ -1 & 0 & 0 \\ 0 & 0 & 0 \end{bmatrix}$$

then, a rotation for a small angle is given by

$$R(d\alpha) = \prod_{i=1}^3 R_i(d\alpha_i) \approx I + \sum_{i=1}^3 I_i \cdot d\alpha_i = I + \Omega$$

where Ω is an anti-symmetrical matrix

$$\Omega = \sum_{i=1}^3 I_i \cdot d\alpha_i = \begin{bmatrix} 0 & d\alpha_3 & -d\alpha_2 \\ -d\alpha_3 & 0 & d\alpha_1 \\ d\alpha_2 & -d\alpha_1 & 0 \end{bmatrix}$$

If R_o corresponds to a estimated rotation angle $\vec{\alpha}_o$ in such a manner that a linearization of $R(\vec{\alpha}_o + d\vec{\alpha})$ by $R_o R(d\vec{\alpha})$ is possible and that \vec{k} is a vector, then it is possible to write

$$\begin{aligned} R(\vec{\alpha}_o + d\vec{\alpha})\vec{k} &\approx R_o(I + \Omega)\vec{k} = R_o\vec{k} + R_o\Omega\vec{k} \\ &= R_o + R_o K d\vec{\alpha} \end{aligned}$$

with

$$K = \begin{bmatrix} 0 & -k_3 & k_2 \\ k_3 & 0 & -k_1 \\ -k_2 & k_1 & 0 \end{bmatrix}$$

In this way the derivative with respect to the rotation's angles of a vector of type $R(\alpha_o + d\alpha)\vec{k}$ can be approximated by the derivative of its linearization.

One then obtain:

$$\left. \frac{\partial(R\vec{k})}{\partial\vec{\alpha}} \right|_{\vec{\alpha}_o} \approx R_o K \quad (8.10)$$

Applying approximation (8.10) to equation (8.9) and supposing that the errors produced by the estimation of the longitude and the latitude are negligible with respect to the other, we obtain

$$d\vec{r}^L = d\vec{f}^L + R_B^L M^B d\vec{\chi} + R_B^L d\vec{m}^L \quad (8.11)$$

where: M^B is an anti-symmetrical matrix similar to the K matrix described previously and containing the elements of the vector $d\vec{m}^L$.

In matrix notation equation (8.11) get the form:

$$d\vec{r}^L = A \cdot d\vec{x} = \begin{bmatrix} I, R_B^L M^B, R_B^L \end{bmatrix} \cdot \begin{bmatrix} d\vec{f}^L \\ d\vec{\chi} \\ d\vec{m}^L \end{bmatrix} \quad (8.12)$$

Setting all the elements $d\vec{x}$ to zero except one it is easy to compute the influence of the selected element on the position of the reference's mirror

In a first step we set $\vec{\chi}^T = (0,0,0)$, and take for the dx_i , some a-priori values for the precision. We also set $dx_i = \sigma_i$, for the most unfavorable case for each element to be studied

The accuracy in kinetic GPS ($d\vec{f}$), is known thanks to previous experiences (Cocard 1995; Favey and Schlatter, 1998). The accuracy of \vec{m} is of the order of one centimeter. Considering the roll, pitch and yaw angles equal to zero, $d\vec{f}$ and $d\vec{m}$ propagate them linearly in $d\vec{x}$. This is summarized in Table 8-2.

	dx_1 [m]	dx_2 [m]	dx_3 [m]
$df_1 = 0.05$ [m]	0.05	-	-
$df_2 = 0.05$ [m]	-	0.05	-
$df_3 = 0.12$ [m]	-	-	0.12
$dm_1 = 0.02$ [m]	0.02	-	-
$dm_2 = 0.02$ [m]	-	0.02	-
$dm_3 = 0.02$ [m]	-	-	0.02

Table 8-2: Summary of the influence of errors in the estimation of \vec{m} or \vec{f} to the determination of the position of the reference's mirror (Favey, 2001).

The accuracy of the angles ϕ , θ and ψ is also known from previous surveys (Favey, 2001) and vary between 0.05° and 0.1° . In order to estimate the propagation of the attitude errors on the position we set $d\phi = d\theta = d\psi = 0.075^\circ$. We also know that during a stabilized flight these angles are inside a window of $\pm 5^\circ$, we then set them equal to 5° . The propagation's errors obtained with these parameters are summarized in Table 8-3:

	dx_1 [m]	dx_2 [m]	dx_3 [m]
$dm_1 = dm_2 = dm_3 = 0.02$ [m]			
$d\phi = d\theta = d\psi = 0.075$ [°]	0.08	0.1	0.2
$\phi = \theta = \psi = 5$ [°]			

Table 8-3 : Summary of the influence of the estimation's errors of the attitude on the determination of the position of the reference's mirror.

Estimation of the measurement accuracy of the position of the reference's mirror

Using matrix A of equation (8.12) the accuracy of \vec{r} can be estimated by

$$C_{rr} = AC_{xx}A^T \quad (8.13)$$

C_{rr} is the covariance matrix of \vec{r} , and C_{xx} is filled by the covariance coefficients of the variables contained by \vec{x} . Making the hypothesis that all the variables are independent, the matrix C_{xx} can be written as

$$C_{xx} = \begin{bmatrix} \sigma_{f_1^L}^2 & 0 & 0 & 0 & \dots & 0 \\ 0 & \sigma_{f_2^L}^2 & 0 & 0 & \dots & 0 \\ 0 & 0 & \sigma_{f_3^L}^2 & 0 & \dots & 0 \\ 0 & 0 & 0 & \sigma_{\chi_1^L}^2 & \dots & 0 \\ \vdots & \vdots & \vdots & \vdots & \ddots & \vdots \\ 0 & 0 & 0 & 0 & 0 & \sigma_{m_3^L}^2 \end{bmatrix} \quad (8.14)$$

In order to estimate the accuracy of the position of the reference's mirror we have to introduce some known a priori values for the σ_x . Using the same values as that used for the estimation of the error's propagation we finally obtain

$$\begin{array}{l} \sigma_{r_1} = 0.24 \text{ [m]} \\ \sigma_{r_2} = 0.42 \text{ [m]} \\ \sigma_{r_3} = 0.45 \text{ [m]} \end{array} \quad (8.15)$$

Another method allowing the determination of the accuracy of the position measured by *GPS* is to use the positions obtained by one antenna for different ground reference and to compute the mean value. The differences between the mean value and the different positions give an estimation of the maximal deviation, which can be considered as a measurement of the precision. This method used in airborne gravimetry by Verdun (*Verdun*, 2000) gives an accuracy of the positions of ~ 50 cm for σ_{r_1} and σ_{r_2} , and ~ 1 m for σ_{r_3} . The estimated accuracy obtained σ_{r_3} by this method is around twice of the previous one. It is worth noting that this estimation is the most unfavorable one.

The influence of an erroneous position on the gravity measurement depends of the horizontal respectively vertical gradient of g .. The horizontal gradient in the area of our test survey (Alps) is around $2 \mu\text{Gal}/m$ and the normal vertical gradient of $300 \mu\text{Gal}/m$.. An error of half a meter in the horizontal position produces an error of $1 \mu\text{Gal}$ and an error of $1 m$ in the vertical position produces an error of $300 \mu\text{Gal}$ on the measurement of g . These two values are negligible with respect to the expected accuracy of 2 to $10 m\text{Gal}$.

However, the accuracy of the determination of g depends also on the accuracy of the determination of the vertical \ddot{h} and Eötvös $E = E(h, \varphi, \alpha, V_h)$ accelerations. The error ΔE is linearly dependant of the errors Δh , $\Delta \varphi$, $\Delta \alpha$ and ΔV_h obtained respectively the altitude, the latitude, the azimuth and the horizontal velocity as shown by the error propagation equation (8.16)

$$\Delta E = \left| \frac{\partial E}{\partial h} \right| \cdot \Delta h + \left| \frac{\partial E}{\partial \varphi} \right| \cdot \Delta \varphi + \left| \frac{\partial E}{\partial \alpha} \right| \cdot \Delta \alpha + \left| \frac{\partial E}{\partial V_h} \right| \cdot \Delta V_h \quad (8.16)$$

Coefficients				
Azimuth	$\left(\frac{\partial E}{\partial h} \right)_{\varphi, \alpha, V_h}$	$\left(\frac{\partial E}{\partial \varphi} \right)_{h, \alpha, V_h}$	$\left(\frac{\partial E}{\partial \alpha} \right)_{h, \varphi, V_h}$	$\left(\frac{\partial E}{\partial V_h} \right)_{h, \varphi, \alpha}$
0°	$1.6 \times 10^{-5} \text{ mGal}/m$	0	$14 \text{ mGal}/^\circ$	$2.5 \text{ mGal}\cdot\text{s}/m$
90°	$15 \times 10^{-5} \text{ mGal}/m$	$1.7 \times 10^{-1} \text{ mGal}/^\circ$	0	$13 \text{ mGal}\cdot\text{s}/m$

Table 8-4: Table of the coefficients deduced from the theoretical Eötvös correction. The coefficients have been computed for two azimuths corresponding to a North-South profile ($\alpha = 0^\circ$) and a East-West profile ($\alpha = 90^\circ$) The flight altitude is $2500 m$ and the ground speed of the aircraft 70 m/s .

Because no information about the accuracy of the flight parameter was available we used those obtained during the ASFAG project (*Verdun*, 2000). Because both projects were flown in similar conditions (mountainous area, stabilized flight) the use of these parameters seems to be absolutely reasonable. These data are reproduced in Table 8-5.

Parameters	Accuracy
Vertical accelerations	$\sigma_{\ddot{h}} = 50 \text{ mGal}$
Latitude	$\sigma_{\varphi} = 5e-7^\circ$
Azimuth	$\sigma_{\alpha} = 0.01^\circ$
Ground speed	$\sigma_{V_h} = 0.02 \text{ m/s}$
Eötvös	$\sigma_E = 0.15 \text{ mGal}$

Table 8-5: Summary of the accuracy of the flight parameters after *J. Verdun*, (2000)

Taking into account the values listed in Table 8-4 and Table 8-5 it is possible to estimate the influence of the Eötvös correction. One can clearly see that this correction is little sensitive to the variations of altitude: $1 m$ inaccuracy produces an error of $0.15 \mu\text{Gal}$. The inaccuracy of

the latitude induces an error of 0.00008 mGal . The azimuth and the ground speed are estimated with an accuracy of 0.01° and 0.02 m/s respectively producing errors of 0.13 mGal and 0.14 mGal . Totally the error on the Eötvös correction is around 0.3 mGal .

The most critical parameter is obviously the non-gravitational vertical accelerations of which the inaccuracy is 50 mGal . However compared with the values that these acceleration can reach, some thousands of mGal , (see Figure 8-1.a-d) this error is acceptable. Before being introduced as corrections the non-gravitational vertical accelerations have to be filtered in order to eliminate the influence of the high frequency phenomenon (e.g. turbulence).

As shown by *Klingelé et al.* (1997) and *Verdun* (2000) the accuracy of the determination of the non-gravitational vertical accelerations is frequency-dependant. This accuracy decrease to some mGal when the wavelength is around 20 km .

8.2 Processing of the gravity data

The data produced by the FG5-L gravimeter are processed in two steps. The first step is dedicated to the elimination of the erroneous or doubtful data whereas the second step deals with the determination of g by adjustment on a physical model for each fall. However, before explaining the processing of the gravity measurement it is worth analyzing the accelerations measured by the INS along the lines of measurements.

Once the gravity data have been processed we estimated their quality by comparing their values with those obtained by upward continuation of ground data.

8.2.1 Upward continuation of the ground data

The estimation of the validity of the airborne measurements can only be done by comparison with data obtained from another method of measurement, ground data, for example.

It is clear that gravity data measured at 2500 m altitude cannot be directly compared with data measured between 500 m and 2000 m . Before performing this comparison either the ground data have to be upward continued at the flight altitude or the airborne data have to be downward continued to the altitude of the ground measurements. Because the prolongation operator works like an amplifier for the short wavelengths of the anomaly we adopted the first approach consisting of upward continuing the ground data.

Instead of computing a Bouguer anomaly for each airborne measurement we computed the theoretical value of g from the upward continued ground anomaly following the definition of the anomaly.

$$g_{\text{Bouguer}} = g_{\text{measure}} - g_{\text{norm}} + g_{\text{Top}} - g_{\text{BPl}} + g_{\text{free-air}} \quad (8.17)$$

g_{Bouguer} : Full Bouguer anomaly

g_{measure} : Measured g

g_{norm} : Normal gravity

g_{Top} : Topographic corrections

g_{BPl} : Bouguer layer effect

$g_{\text{free-air}}$: Free-air effect

Re-ordering the relationship one obtains:

$$g_{measure} = g_{Bouguer} + g_{norm} - g_{Top} + g_{BPI} - g_{free-air}$$

It is, therefore, quite simple to obtain the theoretical measured g at any point on the plane of airborne measurements.

From the data bank of the EGT (European GeoTraverse), a grid with a mesh size of 1 km covering the whole Switzerland and a part of Italy, Germany and France was produced by interpolation (E. Klingelé et al. 1997). In order to get a support surface having no parts higher than the flight altitude the stations located higher than 2000 m were removed from the data bank before interpolation. Then using the well-known FFT technique the anomaly, supposed at an altitude of 500 m , was upward continued to 2500 m according to equation (8.18).

$$g(x, y, z_o + h) = F^{-1} \{ e^{-fh} F \{ g(x, y, z_o) \} \} \quad (8.18)$$

It is clear that the hypothesis of a horizontal support surface of the Bouguer anomaly at 500 m altitude is not completely true and could introduce distortions on the upward continued anomaly. In principle the continuation should be done from the irregular support surface to the horizontal plane at 2500 m by for example an equivalent source technique. However, because most of the ground measurement points are between 400 m and 1000 m altitude and spread on a very large surface (>50000 km^2) the distortion effect is very small as the following evaluation has shown.

The upward continued anomaly was compared to measurement points lying between 2400 and 2600 m , where the Bouguer anomaly is known to better 0.5 $mGal$. This comparison shows that the difference is at most around +/- 3.5 $mGal$. It is worth noting that the nodes of the grid do not correspond exactly to the location of the measurement points in the horizontal coordinates and altitude and therefore a linear three-dimensional interpolation was necessary for the comparison.

The value of g obtained at the mean flight altitude is shown in Figure 8-3. As pointed out by Klingelé (E. Klingelé, 1996) independently to the method used for the upward continuation the longest wavelength still present in the continued anomaly depends on the size of the area used for this prolongation. Because in the Alps the larger amplitudes are in the long wavelengths that the values of the upward continued anomaly can be underestimated and consequently the theoretical value of g overestimated.

From our own analysis, this overestimation could range from 40 to 80 $mGal$ depending on the location of the point in consideration.

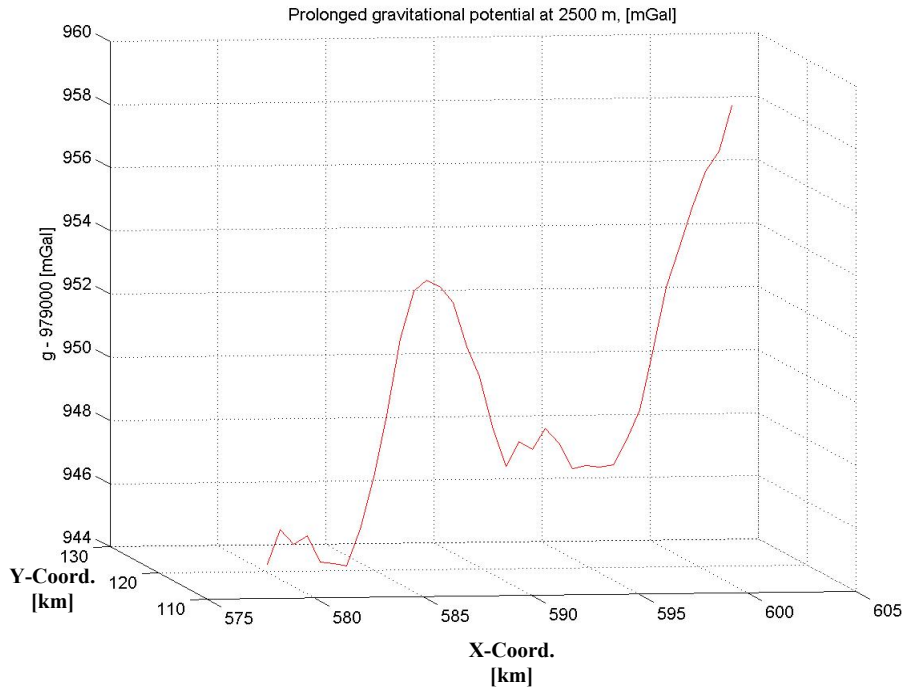


Figure 8-3: Value of g at a mean altitude of 2500 m computed through the ground upward continued Bouguer anomaly. Note that the variation of g from the beginning to the end of the line varies of only 20 $mGal$.

8.2.2 Analysis of the perturbing accelerations produced by the aircraft

In chapter 4.2 we did a first analysis of the accelerations produced by the engines of the aircraft and by the movement of it. In order to get more precise information of these accelerations acting on the reference's mirror we analyzed the measurements of the *INS*.

These data were processed in such a manner to obtain the whole kinematics accelerations produced by the aircraft. The accelerometers of the *INS* measure the sum of the kinematics accelerations and the local gravity.

In the local reference frame it can be formulated as (Fadi, 2001):

$$a^l = f^l - (2\Omega_E^l + \Omega_L^l)v^l + g^l \quad (8.19)$$

Where:

a^l : Kinematics acceleration in the local reference frame

f^l : Forces measured by the accelerometers

Ω_E^l : Anti-symmetric matrix associated to the rotation's vector $\vec{\omega}_E$ representing the rotation of the Earth with respect to the geocentric reference frame

Ω_L^l : Anti-symmetric matrix associated to the rotation's vector $\vec{\omega}_E$ representing the rotation of the local reference frame with respect to the geocentric reference frame

v^l : Ground speed

g^l : Local gravity

Ω_l^l is determined by means of the combination of the *INS* and *GPS* measurements. The ground speed v^l is determined by the *GPS* data only. Then by introducing a model of the local gravity g^l , it is possible to determine the kinematics accelerations acting on the reference's mirror. The whole *INS* data were processed with software developed by par J. Skaloud (J. Skaloud, 1995)

Figure 1-2 shows the vertical kinematics accelerations estimated in the local reference frame and their amplitude spectrums whereas the horizontal kinematics accelerations and their spectrum are shown in Figure 8-4.

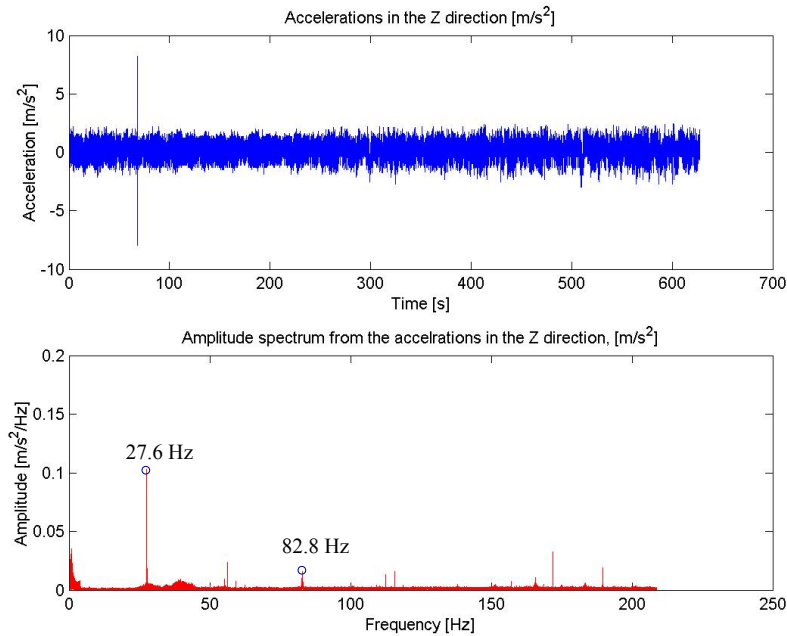


Figure 8-4: Measured vertical accelerations and their amplitude spectrum. The upper graph shows the measured accelerations measured by the *INS* during the first flight Leuk-Martigny. The lower graph shows the amplitude spectrum of these accelerations.

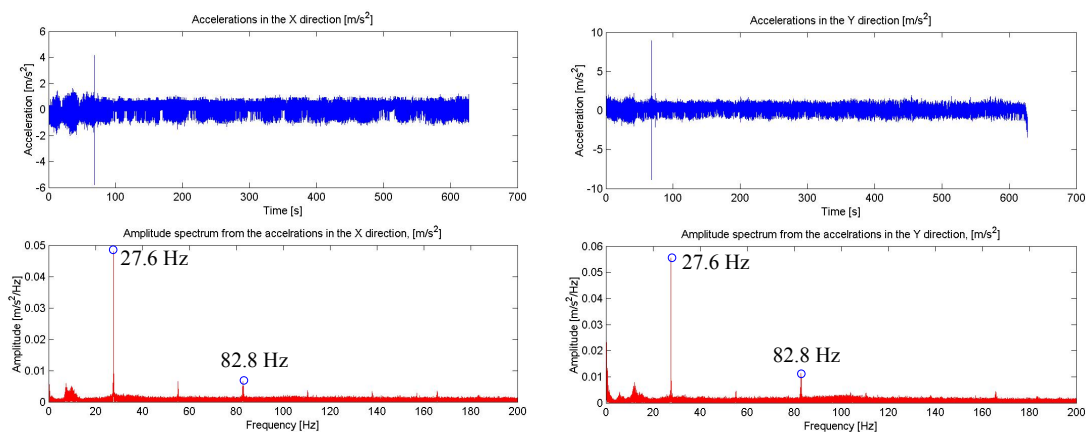


Figure 8-5: Measured horizontal accelerations and their amplitude spectrum. The upper graph shows the measured accelerations measured by the *INS* during the first flight Leuk-Martigny. The lower graph shows the amplitude spectrum of these accelerations.

By comparing the amplitude spectra of the measured accelerations during the test flight and during the measurement flight one can clearly see that these are absolutely not equal. The peaks at 28 Hz and around 83 Hz are present on both spectra but a series of resonance peaks appear during the measurement flight. The sources of these perturbations is, however, difficult to determine. Nevertheless these perturbations have to be introduced in the physical model in order to fit the reality as good as possible. In order to get an idea about the influence of the driving system of the FG5-L we did two supplementary spectral analysis (Figure 8-6 and Figure 8-7) corresponding to accelerations measured during the falls and between the falls respectively.

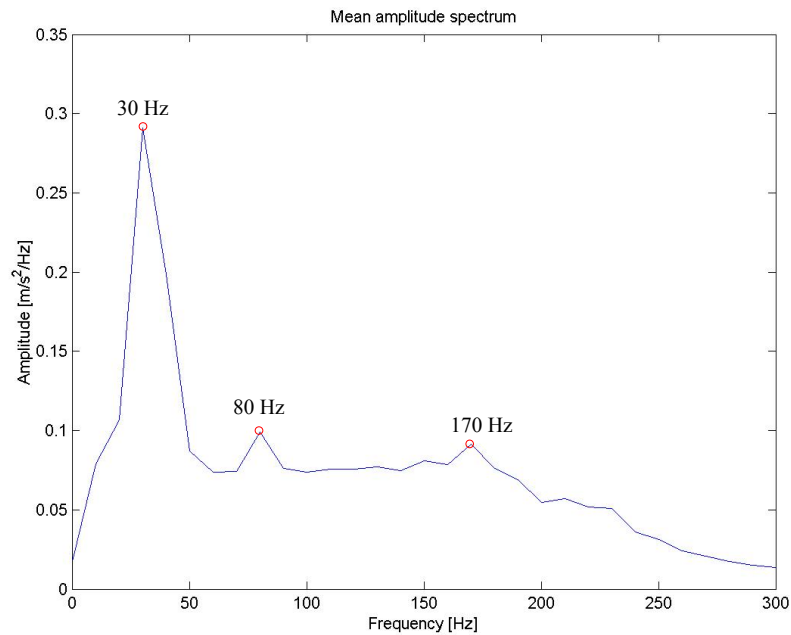


Figure 8-6: Mean amplitude spectrum of the accelerations measured during the falls.

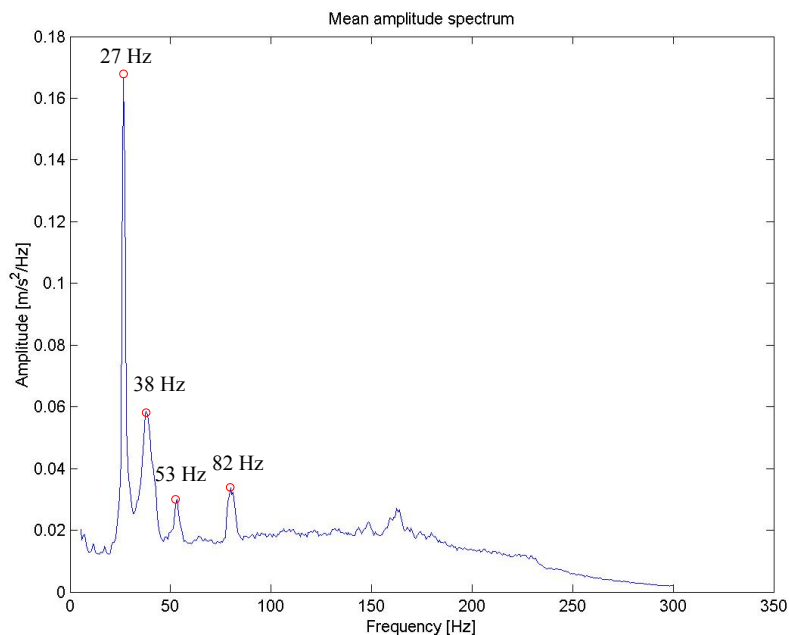


Figure 8-7: Mean amplitude spectrum of the accelerations measured between the falls. These accelerations correspond to the perturbations produced by the aircraft.

These two graphs clearly show that the excitation frequencies are the same in both cases. The only small difference is that the peak of the accelerations measured during the fall is larger than that of the measurements between the falls. This is due to the fact that the duration of measurements used for the computation of the spectrum is shorter in the first case than in the second case (0.1 s for 1 s)

This short analysis allows us to summarize the principal perturbing sources, which we will introduce as variables in the model.

Amplitude [m/s ² /Hz]	Fréquence [Hz]
0.173	27
0.059	38
0.035	82
0.029	53

Table 8-6: The principal perturbing frequencies and their amplitudes

8.2.3 Estimation of the apparent acceleration A_{app} for a single fall.

First step, elimination of the erroneous measurements.

The major problem encountered during the airborne measurements was that of the horizontal position of the support table and consequently the verticality of the gravimeter. In principle a small deviation around the vertical does not affect the measurement. In reality because the space between the falling prism and the drag-free chamber is only of some millimeters, an inclination of more than 1° leads to a collision between the prism and the wall of the chamber. The aircraft flying with a more or less constant pitch of around 3° it was necessary to equip the support table with a 3 point leveling system in order to maintain the position horizontal with an accuracy of $\pm 0.5^\circ$. Despite this system the collision prism-drag-free chamber could not be completely avoided.

A collision between the prism and the wall of the drag-free chamber has for consequence to produce a discontinuity in the function of the residues obtained during the estimation of A_{app} .

In Figure 8-8 such a discontinuity produced by a collision can be clearly seen.

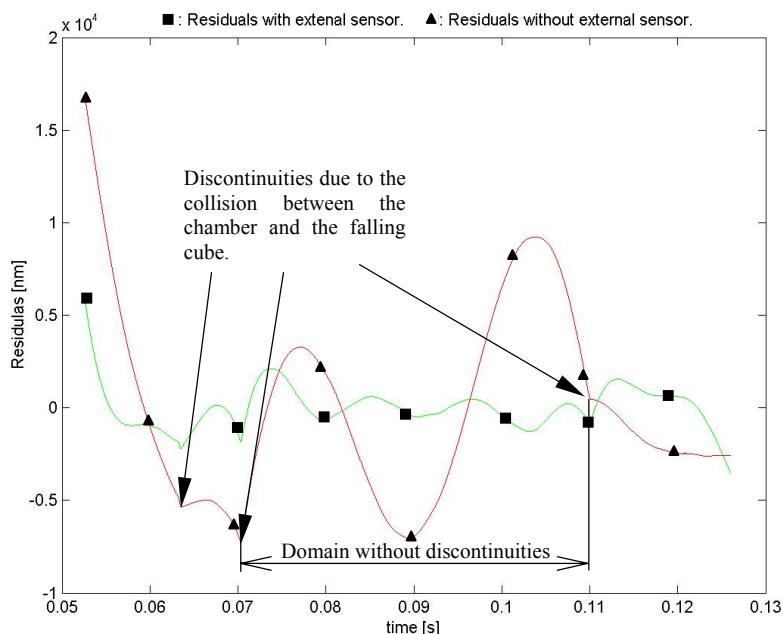


Figure 8-8: Example of a function of residuals. The curves shows clearly the discontinuities produced by the collision between the falling cube and the wall of the drag-free chamber. The time interval between 0.07 s and 0.11 s corresponds to a pure free fall.

In order to test the validity of each drop several methods were tested. During the adjustment by least-squares the time interval used for the adjustment can be optimized by removing the first and the last measurement's points, that is to set a upper and a lower limits. This optimization can be based either on the *RMS* or on the theoretical value of g . Such methods are not flexible enough and constrain too much the estimated A_{app} toward the theoretical g . More, the functions of residues obtained after the optimization procedure still show many discontinuities.

A second method consists of setting the bounds used for the adjustment in such a manner that the time interval without discontinuities is the largest possible. The disadvantage of this method is that it leads to take too short windows. Shorter is the window more low frequencies are lost in the physical model (see equation (6.2)). Knowing that the information lies mostly

in the low frequency domain and that the perturbations induced by the engine are around 28 Hz one can conclude that this method is not appropriate.

The third method, which was used in this project, is to set the bounds in such a manner that the largest measurement window is around 0.1 s and then to eliminate all the drops having a discontinuity inside this time interval.

Second step, estimation of A_{app} for every single fall

After having eliminated all the erroneous falls the value of A_{app} is determined by adjustment to the physical model described by equation (6.2), by introducing as variable the frequencies of the principal perturbators as described in Table 8-6. The method is the same as the one developed during the test with the truck (see chapter 6) with the difference that the determination of the movements of the reference's mirror is based on the *INS* data.

The graphs of Figure 8-9 represent the residuals obtained by adjustment on the classical model to say without taking into account neither the movements of the reference's mirror nor the frequencies of the principal perturbators. The graphs of Figure 8-11 represent the amplitude spectrums of these signals.

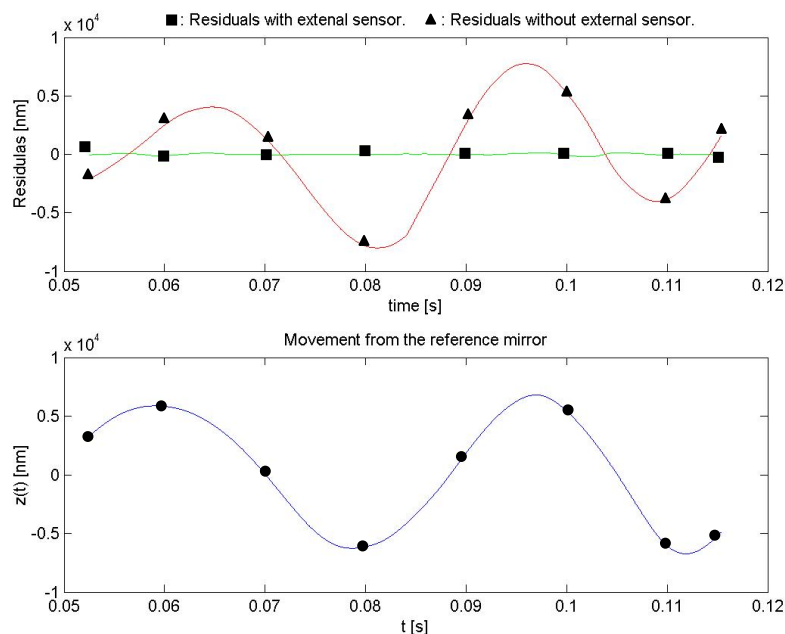


Figure 8-9: Functions of residuals and movements of the reference's mirror. The curve marked by ■, represents the residues obtained when the movements of the mirror (lower graph) is not taken into account. The curve marked by ▲, represents the residues obtained when the movements of the reference's mirror and the frequencies of the four principal perturbators are taken into account.

The graphs of Figure 8-9 clearly show the strong correlation between the classical function of residues and the movements of the reference's mirror determined by the *IMU*. It is also worth noting the spectacular improvement of the adjustment: around a factor of **30** between the amplitudes of the residues. A more detailed view of the residues obtained after adjustment is presented in Figure 8-10.

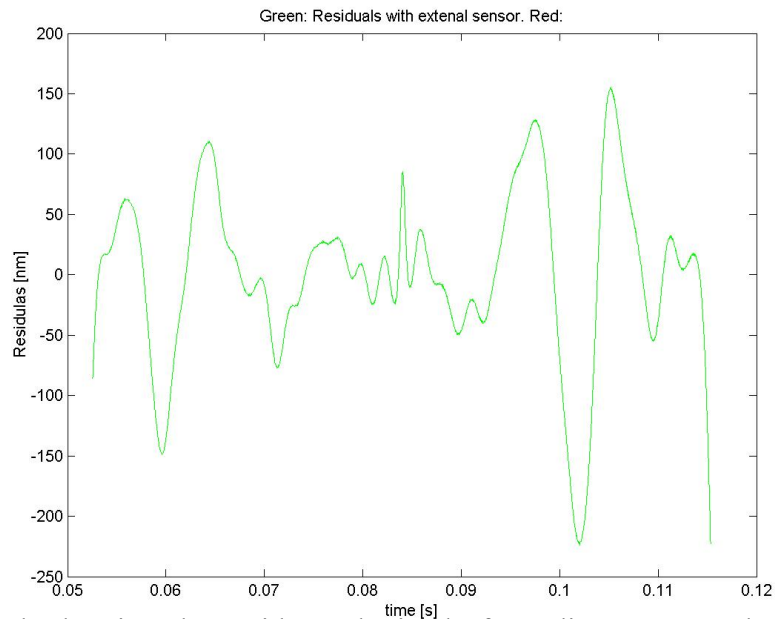


Figure 8-10: Graph showing the residues obtained after adjustment on the physical model described by equation (6.2).

The amplitude of the corrected residuals presented in Figure 8-10 are of the same order of magnitude as those obtained in the laboratory without external corrections. So the resolution one can expect for the apparent acceleration should be one the same order of magnitude: several *mGal*.

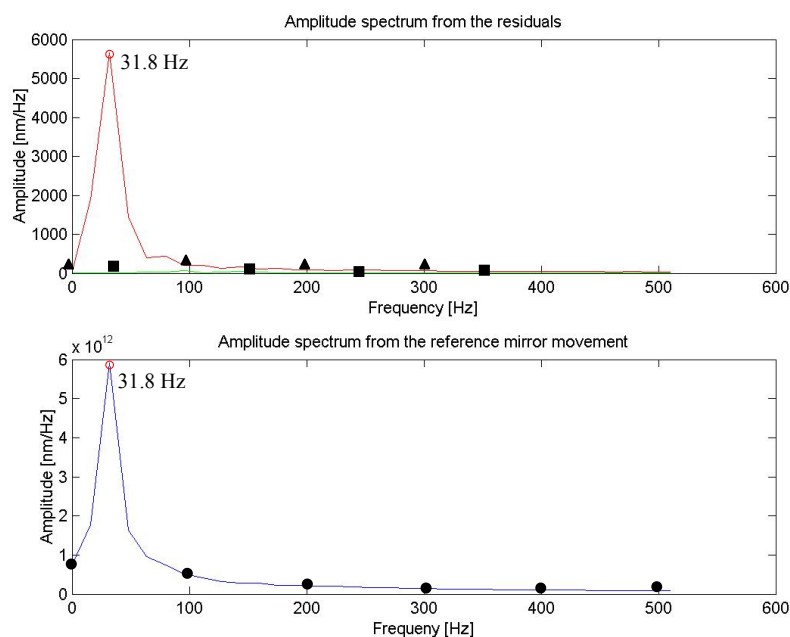


Figure 8-11: Amplitude spectra of the residuals and of the movement of the reference mirror.
 ▲: Amplitude spectrum of the classical function of residuals. ■: Amplitude spectrum of the function of residuals corrected by means of the movements of the reference's mirror.
 ●: Amplitude spectrum of the movements of the reference mirror.

Like for the analysis of the residuals of Figure 8-9, the amplitude spectra represented in Figure 8-11, show an almost perfect correlation between the residuals and the movements of the reference's mirror. However, it is interesting to point out that the principal correlated frequency is around 32 Hz, which corresponds to the one measured in the laboratory.

We formulated the hypothesis that this resonance is generated by the driving system of the drag-free chamber but if it would be the case the residuals should be 25 times less than they are.

It seems that there is a resonance of the FG5-L amplified by the quasi white noise of the vibrations of the aircraft. It is also important to see that the corrected amplitude spectrum is almost flat compared to the uncorrected one. A more detailed analysis of the corrected residues is presented in Figure 8-12.

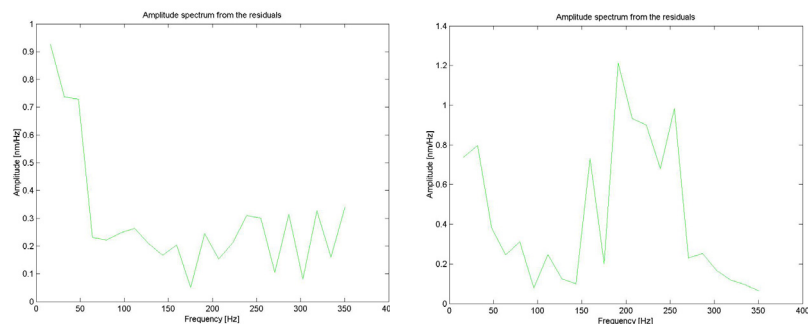


Figure 8-12: Amplitude spectrum of the data of an airborne fall (left diagram) and of a laboratory drop (right diagram). Both were obtained by adjustment on the corrected physical model (6.2) at the difference, which for the laboratory solution the principal frequencies were not taken in account.

The amplitude of the spectra of Figure 8-12 (spectrum of the data of airborne drop adjusted on the model (6.2) and of the laboratory drop adjusted on the model (6.1) are of the same order of magnitude. This allows us to conclude that the airborne measurements of the apparent accelerations are comparable to those of laboratory measurements, to about 2-5 *mGal* (see chapter 5.5). It is also worth noting that the introduction of the frequencies of the 20 principal perturbators almost removes the peak between 150 Hz and 300 Hz. The results of the estimation of the apparent accelerations A_{app} , along each flight line are presented graphically in Figure 8-13.

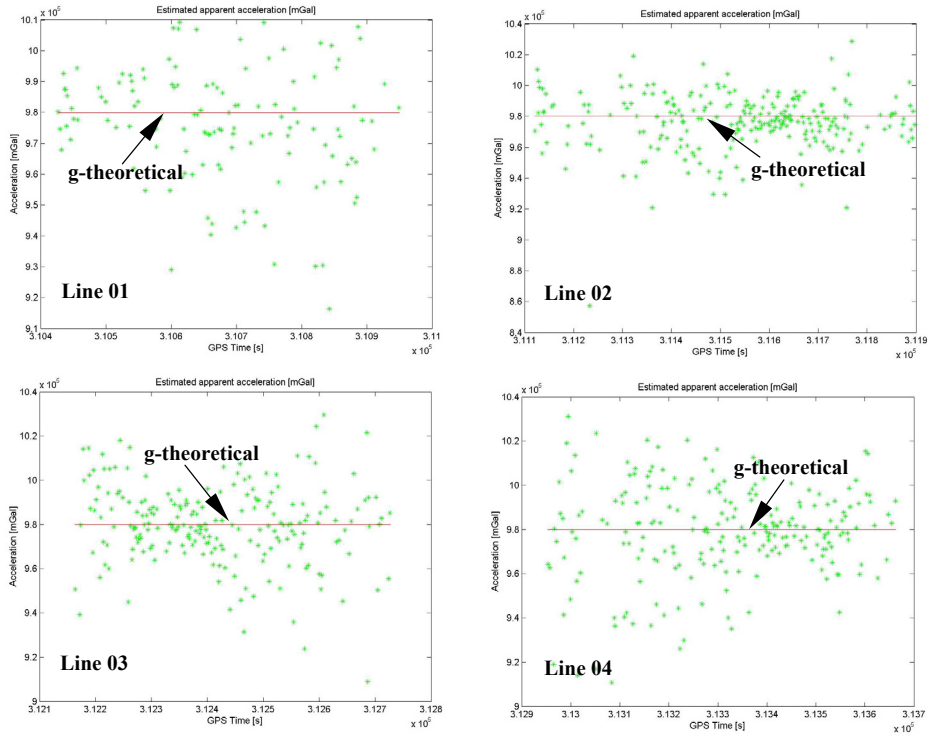


Figure 8-13: Estimated apparent accelerations A_{app} along the flight lines.(Line 01, 03 : Leuk-Martigny et Line 02,04 : Martigny-Leuk)

Table 8-7 gives an overview of the principal values obtained during the estimation of the apparent accelerations along each flight line.

	Line 01	Line 02	Line 03	Line 04
$\overline{A}_{apparent}$ [mGal]	974570.52 $\sigma = 20614.76$	976481.16 $\sigma = 18012.84$	979915.48 $\sigma = 17717.14$	979144.96 $\sigma = 20909.46$
$\Delta = \overline{A}_{apparent} - g_{theo} $ [mGal]	5329	3585	29	752
$Mean_{Drop_rms}$ [nm]	8.62 $\sigma = 14.21$	12.86 $\sigma = 17.23$	8.06 $\sigma = 11.53$	7.56 $\sigma = 8.94$
$\overline{\sigma}_{A_{apparent}}$ [mGal]	4.96 $\sigma = 10.86$	14.96 $\sigma = 19.86$	4.98 $\sigma = 9.96$	5.39 $\sigma = 22.95$

Table 8-7: Summary of the values obtained during estimation of the apparent accelerations along the flight lines. $\overline{A}_{apparent}$: Mean value of the whole apparent accelerations.

$\Delta = |\overline{A}_{apparent} - g_{theo}|$: Difference between the mean value of the whole apparent accelerations estimated along a flight line and the mean value of g , estimated by upward continuation of ground data. $Mean_{Drop_rms}$: Mean value of the whole rms obtained during the adjustment.

$\overline{\sigma}_{A_{apparent}}$: Mean value of the standard deviations obtained during the estimation of the apparent accelerations.

The results presented in Figure 8-13 and summarized in Table 8-7 show mean values of the apparent accelerations $\bar{A}_{apparent}$, which are relatively close to the theoretical value of g , estimated by upward continuation of ground data. The deviations with respect to the theoretical values are for one part due to the kinematic accelerations and for another part to the completely erroneous estimated values.

Of special importance is the obtained $Mean_{Drop_rms}$, values which correspond to the mean value of the whole rms obtained during the estimation of the apparent accelerations and also the $\bar{\sigma}_{A_{apparent}}$, corresponding to the mean standard deviation of the apparent acceleration along a line. Both values confirm that the estimated apparent accelerations are on the order of magnitude of the expected resolution: several $mGal$.

During the estimation of the apparent accelerations for each drop the perturbations acting on the reference mirror were taken into account. Through this the perturbations of which the principal frequencies are between $10\ Hz$ à $400\ Hz$ are strongly attenuated.

However the functions $A_{apparent}(x(t), y(t), z(t))$ have still to be corrected for the kinematic acceleration of low frequencies ($< 10\ Hz$) in order to get the real value of g .

8.2.4 Correction of the functions $A_{apparent}(x(t), y(t), z(t))$

The kinematic accelerations (upper curves) first low-pass filtered at 10 Hz and their amplitude spectrum (lower curves) are presented in Figure 8-14 for each line.

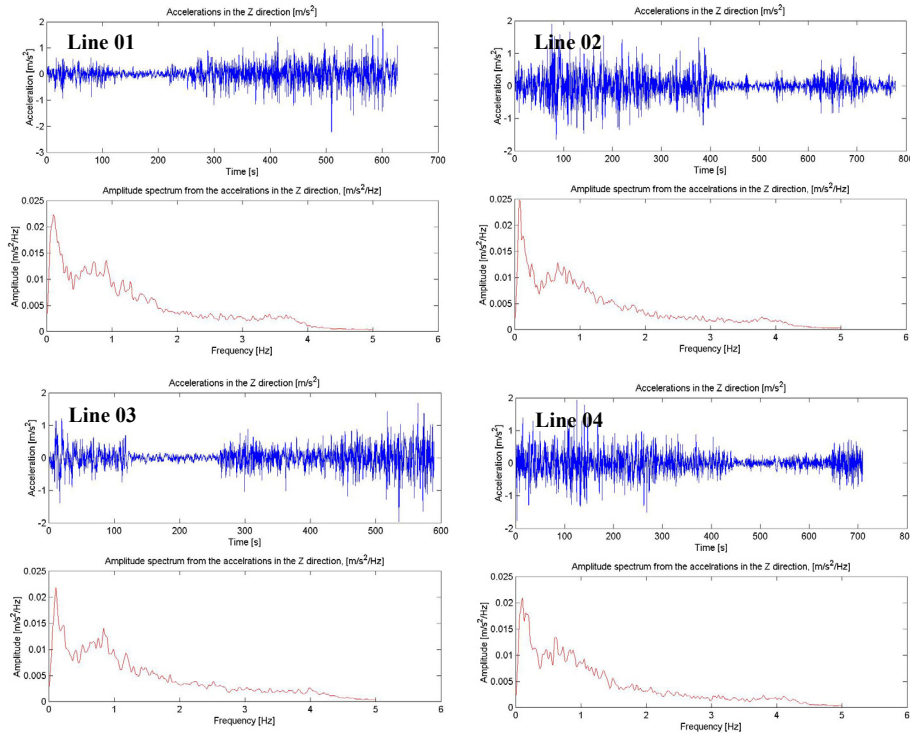


Figure 8-14: Filtered kinematics accelerations and their amplitude spectrums.

Looking at Figure 8-14, it is easy to see that the amplitudes of the kinematics accelerations can reach more than 0.2 g! These amplitudes are almost 10 times stronger than those measured during the relative airborne survey of the French Alps, flown at 5000 m (*E. Klingelé et al. 1997, J. Verdun 2000*). This partly explains the results obtained during the estimation of the mean apparent accelerations (See Table 8-7).

It is also interesting to note the presence of a period of around 150 s on each line during which the flight conditions are more quiet. This is probably due to the configuration of the valley changing the wind conditions, which in turn reduce the turbulence.

The amplitude spectra reproduced in Figure 8-14 show that the maximum of information of the filtered kinematics accelerations is below 4 Hz and that the maximum amplitude is around 0.1 Hz. Before subtracting the kinematic accelerations from the apparent accelerations both were filtered with a low-pass filter of which the cut-off frequency corresponds to the maximum time between two accepted measurements, 20 s. ($F_c = 0.05$ Hz). The combination of the mean ground (around 70 m/s) and this filter leads to a spatial resolution of 1.4 km.

The raw and filtered signals are presented for each line in Figure 8-15 to Figure 8-18.

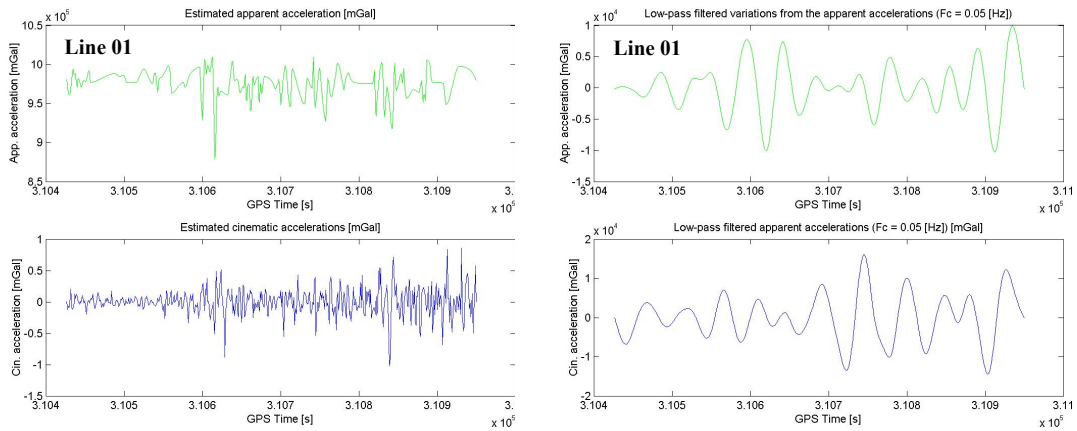


Figure 8-15: Apparent and kinematic accelerations along line 01, Leuk-Martigny. The left graphs represent the unfiltered apparent (upper left) and kinematics accelerations (lower left). The right graphs represent the apparent (upper right) and kinematics (lower right) accelerations filtered with a low pass filter with $F_c = 0.05 \text{ Hz}$.

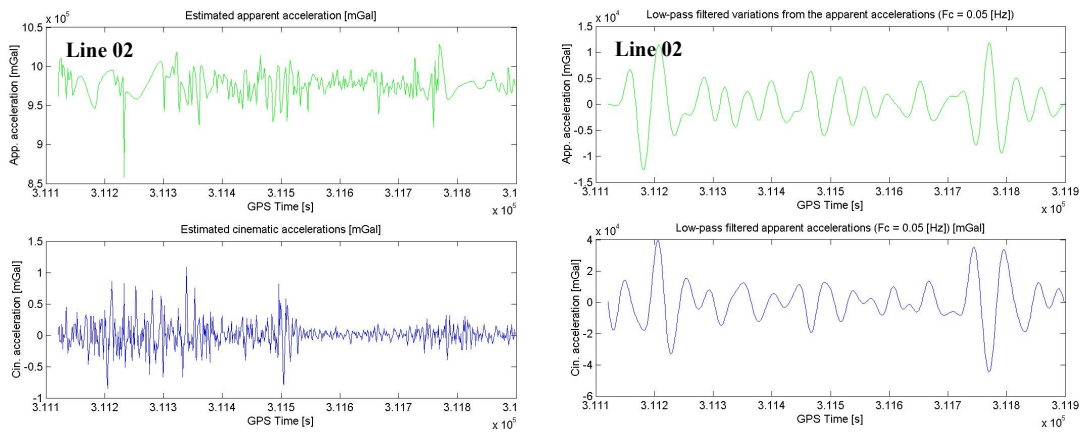


Figure 8-16: Apparent and kinematic accelerations along line 02, Martigny-Leuk. The left graphs represent the unfiltered apparent (upper left) and kinematics accelerations (lower left). The right graphs represent the apparent (upper right) and kinematics (lower right) accelerations filtered with a low pass filter with $F_c = 0.05 \text{ Hz}$.

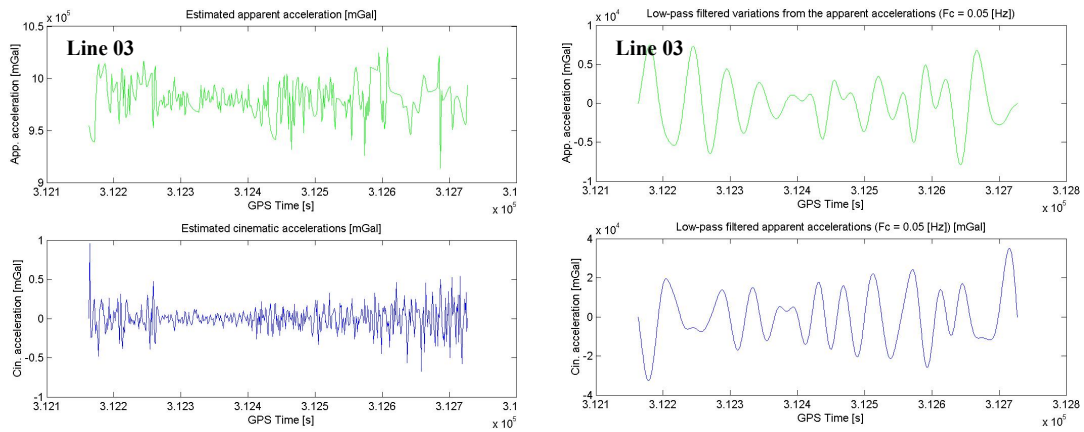


Figure 8-17: Apparent and kinematic accelerations along line 03, Leuk-Martigny. The left graphs represent the unfiltered apparent (upper left) and kinematics accelerations (lower left). The right graphs represent the apparent (upper right) and kinematics (lower right) accelerations filtered with a low pass filter with $F_c = 0.05 \text{ Hz}$.

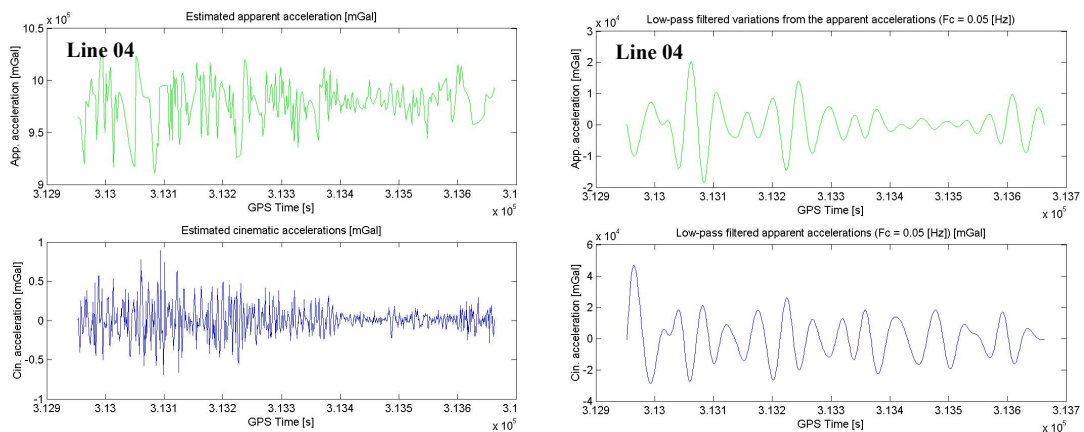


Figure 8-18: Apparent and kinematic accelerations along line 04, Martigny-Leuk. The left graphs represent the unfiltered apparent (upper left) and kinematics accelerations (lower left). The right graphs represent the apparent (upper right) and kinematics (lower right) accelerations filtered with a low pass filter with $F_c = 0.05 \text{ Hz}$.

The accelerations of Figure 8-15 to Figure 8-18 show a good correlation between the lines. It is also seen that the quiet flight period appears in the apparent accelerations and in the kinematic one as well. When filtered the correlation between the two signals is not as marked as previously.

However, this correlation still exists as demonstrated by the two correlation's functions estimated for line number 2 (see Figure 8-19).

Even if the amplitudes of the kinematic accelerations are on the same order of magnitude as the variations of the apparent accelerations around the mean value, the difference is too high to be subtracted without adjustment of the amplitudes. This difference is due to the fact that the kinematic accelerations correspond to the mean value of the values measured during each drop.

The adjustment procedure of the amplitudes is the same as the one we applied to the measurement carried out in the small truck: by signal correlation (See chapter 6.4).

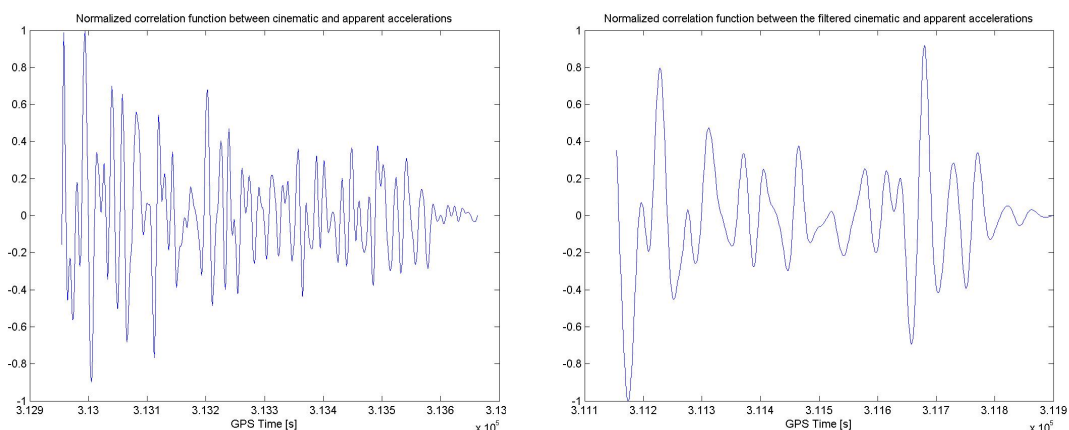


Figure 8-19: Estimated correlation's functions for line number 02. The left graph shows the correlation of the raw accelerations and the right graph shows the correlation between the filtered accelerations (Low-pass filter 20 s).

After have been re-adjusted the kinematics acceleration are subtracted from the apparent accelerations. Then the data are corrected for the Eötvös accelerations and finally filtered for removing the high frequencies produced essentially by the erroneous measurements

The data of each line were processed in the same manner. They were first de-spiked by removing the data of which the amplitude was higher than the mean estimated value $\bar{A}_{apparent} \pm 10'000 \text{ mGal}$. Finally the data were filtered with a low-pass filter having a cut-off frequency of $F_c = 0.0064 \text{ Hz}$. The wavelength corresponding to this frequency is around 11 km for a ground speed of 70 m/s.

The results of this processing are presented graphically in Figure 8-20, and the corresponding statistical data are compiled in Table 8-8.

	Distance [km]	Δg [mGal]	σ_{error} [mGal]
Line 01	28	-41.8	4.1
Line 02	50	-63.1	16.8
Line 03	27	-162.1	9.2
Line 04	40	-54.5	8.9
		$\Delta \bar{g} = 80.3$	$\bar{\sigma}_{error} = 9.7$

Table 8-8: Summary of the statistical data about the estimated value of g along the four flight lines. Distance: length of the line, Δg : mean value of the difference between the estimated value and the value obtained by upward continuation, σ_{error} : standard deviation of the difference between the estimated g and the upward continued value.

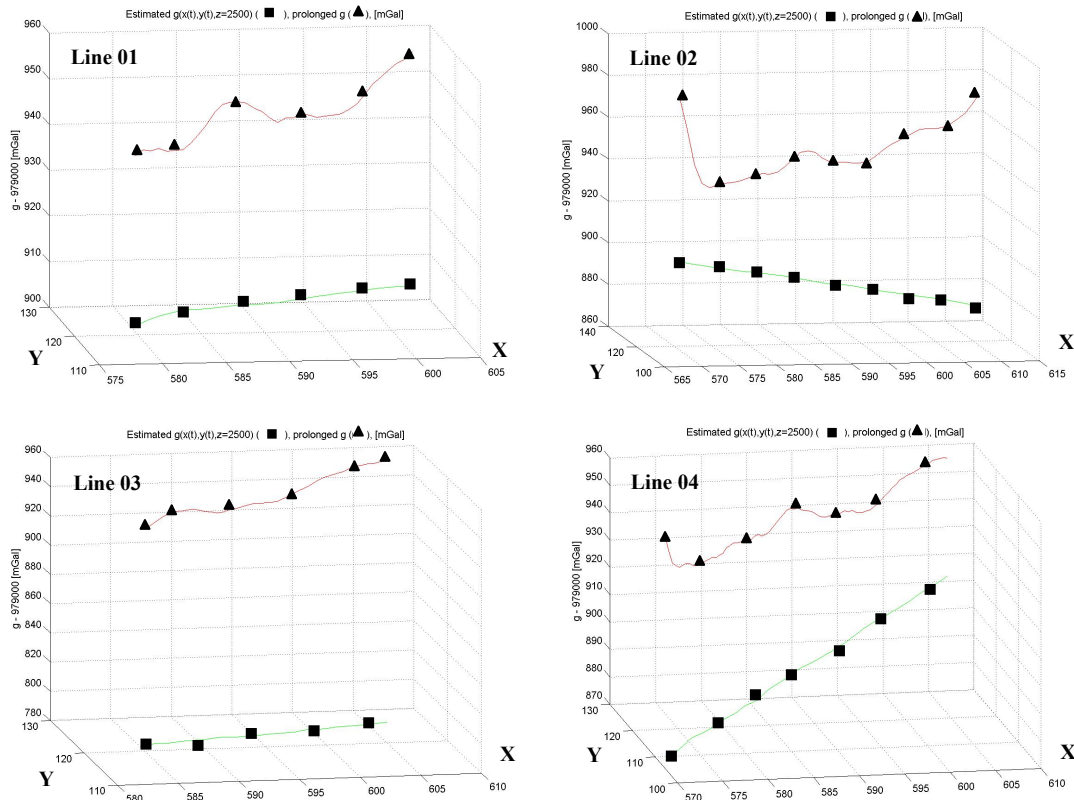


Figure 8-20: Estimated value of g for each flight line (■) $g(x(t), y(t), z=2500)$, and the g value deduced from the upward continued ground Bouguer anomaly (▲).

The diagrams of Figure 8-20 show that only along line 2 the estimated g does not follow the same trend as the gravity obtained by upward continuation of the ground data. For the other three lines both curves are more or less parallel and shifted by a mean value of $\Delta \bar{g} = 80$ mGal. This value is on the same order of magnitude as the one obtained during the relative airborne surveys of Switzerland (*E. Klingelé*, 1996) and of the French Alps (*J. Verdun*, 2000). This is attributed to the upward continuation of the ground data. However, because of the anti-correlation in line 2 this hypothesis cannot be confirmed neither rejected. We saw in chapter 3.3.5 that the resolution of the LN-200 IMU accelerometers was 2400 mGal. During the processing we tried to adjust the measured IMU accelerations with the FG5-L acceleration by correlation. It is possible that, through this kind of processing we introduced a shift due to the low accuracy of the measured accelerations.

Moreover, because lines 1 and 3 were flown from Leuk to Martigny and lines 2 and 4 from Martigny to Leuk it can be surmised that the flight conditions strongly influenced the quality of the data (back or front wind). It is also clear that the shorter lines show the largest difference with the supposed true value. On the other hand the standard deviations do not show any particular correlation either with the flight directions or with the lengths of the lines. Their mean value, $\bar{\sigma}_{error}$, is on the order of magnitude as the expected resolution $\bar{\sigma}_{error} = 9.7$ mGal.

9 Conclusions and recommendations

In the last ten years, global change has become of major concern for mankind. In this context a precise knowledge of the Earth gravity field is of utmost importance in various applications: In geodesy for determining the geoid which serves as the absolute height reference needed for monitoring sea level variations and in geophysics for determining mass anomalies in the Earth interior.

Because satellite gravimetry only covers wavelengths larger than 100 km and the ground and offshore data cover wavelengths extending from meters to some kilometers, there is a large uncovered wavelength domain, which can only be filled by airborne techniques.

Until now, all the airborne gravity surveys were carried out with relative gravimeters. The principal disadvantages of this kind of gravimeters are the correlation between measurements of a same data set, the instrumental drift, the frequency response of the spring and possible variations of the calibration factor. In comparison, absolute gravimetry does not suffer from any of these problems. To our knowledge nobody has attempted to perform measurements with an absolute gravimeter in kinematic mode onboard an aircraft.

As shown in chapters 2 and 3 the most difficult problem in absolute airborne gravimetry is the compensation of the perturbing vertical accelerations. To solve this problem it is absolutely necessary to have a system able to measure both the accelerations induced by the movements of the aircraft and by those generated by the engines and the propellers.

In order to compensate these accelerations two different methods were studied. The first one consists of decoupling the gravimeter from its support by means of a mechanical filter while the second one uses a mathematical model for subtracting numerically the perturbing accelerations.

Three mechanical filters were studied: A commercial optical table from Alcyonics, a multi-layers table and a hanging table.

The application of the transfer functions of these filters to the amplitude spectrum of the vibrations of the aircraft has shown that the hanging table presented the best characteristics in flight conditions. Unfortunately this system like any other mechanical filter has the disadvantage of having a resonance frequency close to the frequency of some typical movements of an aircraft consequently inducing broad oscillations of the table. The only possibility for controlling these oscillations would be to introduce a magnetic damper but that would also decrease the quality of the transfer function. Consequently this solution was not retained.

The numerical compensation and the general behavior of the FG5-L were studied in detail. From this study we could clearly see that the principal components of the FG5-L (laser, GT 650 board) allow measuring g with a resolution of 2.5 mGal for each single fall. It was also possible to confirm that with the numerical compensation of the movements of the reference mirror the residuals are reduced by a factor of 8. In order to test the two methods of compensation a dynamic experiment was carried out in a small truck. From this experiment it was possible to show that the whole system and especially the FG5-L work correctly in an extremely noisy environment.

A first test in strapped-down configuration (without mechanical filter) has shown that the numerical compensation is a fully satisfactory method. The strategy developed consists of decomposing the perturbing accelerations in two distinct groups. In the first group are the perturbation produced by the engines of the aircraft and lying in the frequency band between 10 Hz and 200 Hz. The lower limit of this group corresponds to the falling time of the prism, and the higher limit is given by the sampling rate of the external sensors (Episensor and INS). The second group contains the low frequency accelerations due to the movements of the platform.

The compensation is done in two stages. In the first stage the accelerations of the first group are integrated twice in order to determine the movement of the reference's mirror during the fall. This movement is then introduced as variable in the system of equations allowing the determination of the apparent acceleration. After this procedure has been applied to each fall one obtains a function $a(t)$ from which it is necessary to remove the accelerations of the second group in order to obtain $g(t)$. This method applied to the truck experiment has shown its efficiency and allowed the determination of g with a resolution of **16 mGal**.

Even if this resolution was higher than the expected resolution we found it sufficiently promising for applying it to a real airborne experiment.

A second dynamic test carried out with the hanging table in the small truck was really disappointing. In fact during the development of this table we totally underestimated the influence of the accelerations produced by the movements of the drag-free chamber at the beginning and at the end of each fall. Such accelerations can be assimilated to Dirac impulses, which excite the system in a broad band of frequencies including the resonance frequency of the filter. The measurement frequency of the FG5-L being 0.5 Hz and the resonance frequency of the table 1 Hz, the accelerations of the drag-free chamber produce systematic errors, which cannot be corrected, and the estimated value of g is shifted.

We were also able to demonstrate that the positioning by GPS allows a reasonable determination of the kinematic accelerations and consequently to correct the raw values of g to obtain the true gravity.

A combination of GPS and INS measurements produce complete information of the position of the aircraft in space with a high sampling rate. Using the experience gained during the small-truck experiment it was possible to develop a method of compensation for the airborne measurements taking into account the attitude of the platform during the flight.

Finally the analysis of our results allows us to answer the fundamental questions formulated at the beginning of the project, which were:

- 1. Is absolute airborne gravimetry feasible at all?**
- 2. Which accuracy can we expect from these measurements?**
- 3. What are the advantages and disadvantages of this technique with respect to the classical ones?**
- 4. Which are the necessary improvements to be done to the system in order to make it useful for routine measurements.**

As regards question 1 we can definitively and clearly answer: **YES**

Based on the results summarized in Table 8-7 and Table 8-8 we can claim that the gravimeter FG5-L behaves correctly even in extreme conditions as those encountered during an airborne survey. Therefore the measurements are reliable and can be used for the determination of g .

As regards the question 2, a clear answer is more difficult to formulate.

For a wavelength of **11 km** the mean resolution is **9.7 mGal**. (See Figure 9-1) which approximately corresponds to the one obtained in relative airborne surveys (*Klingelé et al.*, 1996, *Verdun et al.* 2000).

We have seen in chapter 8.2 that the resolution strongly depends on the flight conditions. In our experiments we did not have the choice of the flight area or of the flight altitude. These were imposed to us by the air traffic control and by the meteorological conditions. A flight in a region with a very rugged topography like in the Alps a flight altitude of 2500 *m* is far to be ideal. It would have been better to fly higher than the highest mountain in order to reduce the influence of the turbulences. If a further experiment will append in the future such remarks should be taken into account.

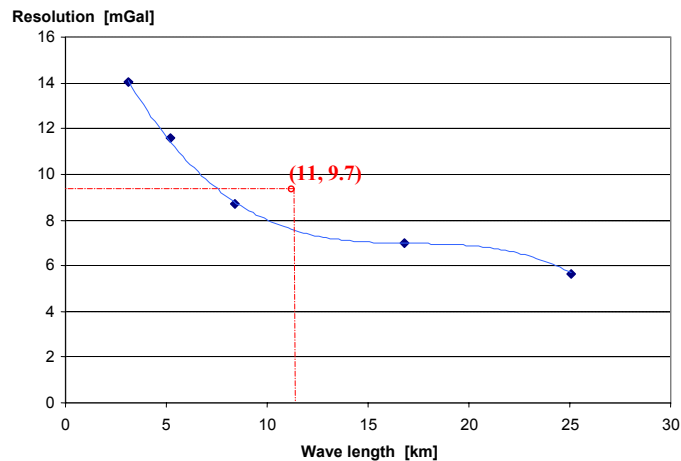


Figure 9-1: Comparison between the resolutions obtained by relative and absolute airborne surveys. The curve (■) represents the experimental resolution obtained during the airborne relative surveys of Switzerland (*Klingelé et al.* 1996) and of the French Alps (*Verdun et al.* 2000). The dot corresponds to the resolution obtained during the present project.

3. What are the advantages and disadvantages of the absolute measurements with regard to the relative one?

The most severe disadvantage is that the sampling rate is too low. While in the relative airborne gravimetry the signal is sampled at 200 *Hz* to 1000 *Hz* in the absolute technique the sampling rate is around a second with a measurement window of 0.1 *s*. This can lead to serious problems at the time of synchronizing the apparent with the kinematic accelerations. Indeed the value of *g* estimated during a single fall corresponds to a mean value of the accelerations working on the falling prism and on the reference mirror. In order to be able to correct the value obtained in this way it is necessary to attribute a time to the estimated value, which can vary between the beginning and the end of the fall. As we have seen in chapter 6 (see Figure 6-23) the kinematic accelerations can vary strongly during a drop. These have a direct influence on the correlation between the estimated apparent gravity and the kinematic accelerations and, therefore, on the quality of the correction.

The best advantage of the method is, without doubt, the possibility of getting directly the value of *g* avoiding a reference station at the airport, avoiding the problems of drifts and tares.

Moreover, the measurements being uncorrelated at all an erroneous value has no influence on the others measurements.

Even if the system needs a leveling table allowing to keep the instrument in a more or less vertical position, the complexity of this table is not comparable at all with the one of a gyro-stabilized platform necessary for relative airborne or ship-borne gravimetry.

The experiments carried out during this project have shown that the gravimeter FG5-L works perfectly in a strapped down configuration which makes the dynamic measurement very advantageous.

While relative airborne measurements needs a time of stabilization at the beginning of each line Klingelé et al. (1996) and Verdun et al. (2000) have shown that the length of the flight line used for the stabilization of the gyro-stabilized platform is on the order of 20 to 30 km) absolute measurements can begin immediately after the aircraft has been positioned on the line. This greatly increases the useful length of the line and consequently reduces the cost of the survey significantly.

4. What are the necessary improvements to be done to the system in order to make it routinely usable?

As we have seen one very important problem is the collision of the falling prism with the drag-free chamber. In order to solve this problem and consequently to avoid this collision it would be necessary to increase the distance between the two objects by increasing the diameter of the chamber.

On the other hand, it is questionable if such a drag-free chamber is absolutely necessary for an expected accuracy of some *mGal* instead of *microGal*. Also the necessity of a constant pumping by an ionic pump can be seriously asked. In our opinion a good vacuum made at the beginning of each day, for example, would be sufficient for our purpose.

In order to improve the accuracy of the correction of the apparent acceleration it would be necessary to have lower frequency of the modeled perturbator. For that the actual length of the dropping chamber of the FG5-L is too short. It should be considered to increase it by a factor of two for getting a longer free-fall.

A very important component to be introduced to the actual system would be a servo-controlled leveling table allowing to keeping the instrument in a vertical position with accuracy better than 0.5 *degree*. This accuracy, of course, depends on the length of the drop and on the distance between the falling prism and the drag-free chamber (if maintained in a fully airborne version of the instrument). A supplementary feature could be to condition the start of a drop to a sufficient accurate vertical position of the gravimeter.

Before beginning with the suggested modifications and improvements it would be reasonable to determine the resonance frequencies of the instrument itself. As we have seen during the analysis of the airborne data it seems that some mechanical components of the instrument enter in resonance with the vibrations of the aircraft, which at the end produce an increase of the residuals (See chapter 8.2).

The different tests we performed during the development of a passive damping system (see chapter 0) have revealed that the addition of a pseudo drag-free chamber moving synchronously with the real drag-free chamber but in opposite direction, can strongly reduce the problem from the floor or platform recoil and this, independently from the type of experiment.

Finally in spite of very unfavorable conditions of measurements, and in spite of a relatively small budget the results obtained can be qualified as good and promising for further experiments and developments.

References

- Baumann, H., Klingelé, E., Geiger, A., Kahle, H.-G. (2002). Problematik der Vibrationen bei der fluggestützten Absolutgravimetrie. 5. MR2002 Symposium EMPA-Dübendorf.
- Baumann, H., E. Klingelé (2002). Flugestutze Absolutgravimetrie. InterGeo 2002, Frankfurt am Main.
- Botton, S., F. Duquenne, Egels, Y., Even, M., et Willis, P. (1997). GPS Localisation et navigation: Hermès éditeur, Paris, 247 p.
- Brown, J.M., Niebauer, T.M. and E.E. Klingelé: (2001) Towards a Dynamic Absolute Gravity System. In Gravity, Geoid and Geodynamics 2000. Proceeding of the GGG2000 IAG International Symposium Banff, Canada. 223-228
- Canuteson, E., Zumberge, M.: (1996) Fiber-opticextrinsic Fabry-Perot vibration-isolated interferometer for use in absolute gravity meters, Appl. Optics, **35**, 3500-3505, 1996
- Canuteson, E., Zumberge, M., Hanson, J.: (1997) An absolute method of seismometer calibration by reference to a falling mass, Bull. Seismo. Soc. Am., **87**, 484-493, 1997
- Cocard, M. (1995). High Precision GPS Processing in Kinematics Mode: Ph.D. Thesis ETH Zürich.
- Dampney, C. (1969). The Equivalent Source Technique: Geophysics, **34**, 39-53
- Emilia, D. (1973). Equivalent Sources Used as an Analytic Base for Processing Total Magnetic Profiles: Geophysics **38**, 339-348
- Fadi A. B. (2001). Some Investigation on Local Geoid Determination from Airborne Gravity Data, UCGE Reports Number 20154
- Favey, E. (2001). Investigation and Improvement of Airborne Laser Scanning Technique for Monitoring Surface Elevation Changes of Glaciers, Ph.D. Thesis, ETH Zürich.
- Favey, E. and Schlatter, A. (1998). Geoidbestimmung am Lac Léman. Technical report, Institut für Geodäsie und Photogrammetrie, ETH Zürich, Bericht Nr. 282.
- Graber-Brunner, V., Klingelé, E., Marson, I. (1991). An Improved Solution for the Problem of Upward Continuation of Gravity Field Data in Rugged Topography. Boll. Geof. Theor. ed Appl., **32**, 130-131.
- Kahle, H.G. (2003): Einführung in die Höhere Geodäsie, ETH Zürich.
- Klingelé, E. (1996). Contribution to the Geology of Switzerland, Swiss Geophys. Comm., Series. Geophys., **30**, 103 p, 22 fig.
- Klingelé, E., Cocard, M., et Kahle, H.-G. (1997) Kinematic GPS As a Source For Airborne Gravity Reduction In The Airborne Gravity Survey Of Switzerland: J. Geophys. Res, B4, **102**, 7705-7715.

-
- Meyer, U., Boedeker, G., Pflug, H. (2003). Airborne Navigation and Gravimetry Ensemble & Laboratory (ANGEL). Scientific Technical Report STR03/06.
- Nelson, P.G., An Active Vibration Isolation System For Inertial And Precision Measurement, *Rev. Sci. Instrum.*, 1991, **62**, 2069-2075.
- Neumeyer, L., Hehl, K. (1995). State-of-the Art and Future Sensor Technology for Airborne Gravimetry: Report of the GeoForschungsZentrum Postdam. Dep: Recent Kinematics and Dynamics of the Earth.
- Niebauer, T.M. (1995). A new generation of absolute gravimeters: *Metrologi*, **32**, 159-180.
- Niebauer, T.M. (1989). The Effective Measurement Height of Free-fall Absolute Gravimeters. *Metrologia*, 1989, **26**, 115-118.
- Rinker, R.L. (1983). Supper Spring. A new Type of Low-Frequency Vibration Isolator, Ph.D. Thesis University of Colorado.
- Schmid H.H., (1977). Ein allgemeiner Ausgleichungs-Algorithmus für die numerische Auswertung in der Photogrammetrie, Institut für Geodäsie und Photogrammetrie an der ETH Zürich, Mitteilung Nr. 22
- Selvakumar, A. (1996). A high sensitivity z-axis torsional silicon accelerometer. International Electron Devices Meeting (IEDM '96).
- Skaloud, J. (1995). Strapdown INS Orientation Accuracy with GPS Aiding, UCGE Reports Number 20079.
- Torge, W., (1989). Gravimetry: Walter de Gruyter. Berlin, New York
- Torge, W., (1991). Geodesy: Walter de Gruyter. Berlin, New York, 2nd edition.
- Verdun, J. (2000). La gravimétrie aéroportée en région montagneuse, Ph.D.Thesis Université Montpellier II.
- Zumberge, M.A., Rinker R., Faller J. E. (1982), A Portable Apparatus for Absolute Measurements of the Earth's Gravity, *Metrologia*, 1982, **18**, 145-152 (1982)

“Geodätisch-geophysikalische Arbeiten in der Schweiz”

**(Fortsetzung der Publikationsreihe ”Astronomisch-geodätische Arbeiten in der Schweiz”
der Schweizerischen Geodätischen Kommission (ab Bd. 48):**

- 48** 1994 Ionosphere and Geodetic Satellite Systems: Permanent GPS Tracking Data for Modelling and Monitoring: Urs Wild, 155 Seiten.
- 49** 1994 Optical Astrometry of Fast Moving Objects using CCD Detectors: Thomas Schildknecht, 200 Seiten.
- 50** 1995 Geodätische Alpen traverse Gotthard: A. Elmiger, R. Köchle, A. Ryf und F. Chaperon. 214 Seiten.
- 51** 1995 Dreidimensionales Testnetz Turtmann 1985-1993, Teil II (GPS-Netz). F. Jeanrichard (Hrsg.) Autoren: G. Beutler, A. Geiger, M. Rothacher, Stefan Schaer, D. Schneider, A. Wiget, 173 Seiten.
- 52** 1995 High Precision GPS Processing in Kinematic Mode: M. Cocard. 139 Seiten.
- 53** 1995 Ambiguity Resolution Techniques in Geodetic and Geodynamic Applications of the Global Positioning System. L. Mervart. 155 Seiten.
- 54** 1997 SG 95: Das neue Schweregrundnetz der Schweiz: F. Arnet und E. Klingelé. 37 Seiten.
- 55** 1997 Combination of Solutions for Geodetic and Geodynamic Applications of the Global Positioning System (GPS). Elmar Brockmann, 211 Seiten.
- 56** 1997 Geoid der Schweiz 1997. Urs Marti, 140 Seiten.
- 57** 1998 Astrometry and Satellite Orbits: Theoretical Considerations and Typical Applications. Urs Hugentobler, 209 Seiten.
- 58** 1998 Systematic Investigations of Error- and System-Modelling of Satellite Based Flight Approaches and Landings in Switzerland. Maurizio Scaramuzza, 165 Seiten.
- 59** 1999 Mapping and Predicting the Earth’s Ionosphere Using the Global Positioning System. Stefan Schaer, 205 Seiten.
- 60** 2000 Modeling and Validating Orbits and Clocks Using the Global Positioning System. Timon Anton Springer, 154 Seiten.
- 61** 2001 Spatial and Temporal Distribution of Atmospheric Water Vapor using Space Geodetic Techniques. Lars Peter Kruse, 128 Seiten.
- 62** 2001 Solar Spectrometry for Determination of Tropospheric Water Vapor. Bernd Sierk, 212 Seiten.
- 63** 2001 Analysis of refraction influences in geodesy using image processing and turbulence models. Philipp Flach, 175 Seiten.
- 64** 2003 INS/GPS Integration for Pedestrian Navigation. V. Gabaglio, 161 Seiten.
- 65** 2003 Efficient Methods for Determining Precise Orbits of Low Earth Orbiters Using the Global Positioning System. Heike Bock, 214 Seiten.
- 66** 2003 Capteurs et Algorithmes pour la Localisation Autonome en Mode Pédestre. Quentin Ladetto, 121 Seiten.
- 67** 2004 GPS based Determination of the Integrated and Spatially Distributed Water Vapor in the Troposphere. Marc Troller, 172 Seiten.
- 68** 2005 Geodetic Mobile Solar Spectrometer. Alexander Somieski, 205 Seiten.
- 69** 2005 Absolute Airborne Gravimetry. Henri Baumann, 142 Seiten.